Copyright
by
Antonio Forenza
2006

The Dissertation Committee for Antonio Forenza
certifies that this is the approved version of the following dissertation:

Antenna and Algorithm Design in MIMO Communication Systems Exploiting the Spatial Selectivity of Wireless Channels

Committee:

Robert W. Heath, Jr., Supervisor

Jeffrey G. Andrews

E. Glenn Lightsey

Edward J. Powers

Sriram Vishwanath

Antenna and Algorithm Design in MIMO Communication Systems Exploiting the Spatial Selectivity of Wireless Channels

by

Antonio Forenza, B.S., M.S.

DISSERTATION

Presented to the Faculty of the Graduate School of

The University of Texas at Austin

in Partial Fulfillment

of the Requirements

for the Degree of

DOCTOR OF PHILOSOPHY

THE UNIVERSITY OF TEXAS AT AUSTIN

May 2006

Dedicated to Gino and Rita.

Acknowledgments

I would like to express my sincere thanks to my supervisor and friend, Prof. Robert W. Heath, Jr., for his invaluable guidance. His knowledge, creativity, never-ending energy and encouragement have been fundamental to my technical growth during my research at UT. I also thank Prof. Jeffrey G. Andrews, Prof. E. Glenn Lightsey, Prof. Edward J. Powers, Prof. Theodore S. Rappaport, and Prof. Sriram Vishwanath for their invaluable feedback on my research and for taking their time revising my dissertation. I want to thank Matthew R. McKay and Iain B. Collings for their collaborative work on the analysis and design of adaptive MIMO systems. Regardless the physical distance USA-Australia, working with Matt has been an amazing experience.

I am very grateful to my former/current colleagues and my friends from the Wireless Networking and Communications Group (WNCG) at UT: Manish Airy, Sandeep Bhadra, Bishwarup Mondal, Taiwen Tang, Chan-Byoung Chae, Seijoon Shim, Roopsha Samanta, David Love, Runhua Chen, Wan Choi, Aamir Hasan, Kyungtae Han, Jeremy Chen, Taeyoon Kim, Zukang Shen, Jihoon Choi, Robert Daniels, Caleb Lo, Ramya Bhagavatula, Frank Sun, Kaibin Huang, Robert Grant, Kitaek Bae, Farooq Sabir, Ian Wong, Sumohana Channappayya, and everybody else. With them I had constructive technical discussions throughout my Ph.D. and very enjoyable time at JP's Java.

I also thank Cristine Ayala, Janet Preuss and Lori Lacy for their invaluable help with the logistics of my Ph.D. and for their positive attitude that made my work at WNCG even more enjoyable. Thanks also to all the faculties and staff from WNCG for enabling cooperative and constructive interactions between students. I also want to thank Melanie Gulick and Michelle Belisle for their help with the paperwork for my Ph.D. and all the funny stories shared with them during these years.

Special thanks go to Hojin Kim, Marios Kountouris, Ashish Pandharipande and Kyungtae Han, who I really enjoyed working with during my summer 2004 internship at Samsung Advanced Institute of Technology (SAIT), Korea. I thank them for being such a great team players at work, fun friends in the nore-bangs and excellent teachers of Korean for me. I also want to thank Russell Priebe and Jayesh Kotecha from Freescale Semiconductor, for supporting my research and the collaborative work during my internship at Freescale over the summer 2005.

I want to thank my dear friends Reza Koohrang, Daniella Hiche, Alex Arcone, Mira Svatovič, Khursheed Hassan, Guglielmo Scovazzi, Amber Heard, Giovanni Migliaccio, Tatiana Ruiz, Lisa Kaselak, and Jonathan Hansen, for their constant encouragement throughout the years of my Ph.D. and for being such a solid pillars for me! I thank all my friends from Austin, California and overseas for all the unforgettable experiences I shared with them over the past few years. I also thank my coach Sean Murray and the UT waterpolo team for the fun time at practice and during the state and national tournaments.

Last but definitely not the least, I want to thank my brother, sisters and in law, Mario, Sonja, Maya, and Peter Tompkins, and my parents, Gino and Rita for their everlasting love, support and encouragement. My brothers and sisters have been wise teachers of life for me, giving me good guidance in several important steps of my life. My parents have always supported me and my professional and academic successes can be traced back to them: thanks Gino and Rita!

Antonio Forenza

The University of Texas at Austin

May 2006

Antenna and Algorithm Design
in MIMO Communication Systems
Exploiting the Spatial Selectivity of Wireless Channels

Publication No. _____

Antonio Forenza, Ph.D.
The University of Texas at Austin, 2006

Supervisor: Robert W. Heath, Jr.

Cellular telephony and wireless Internet access are creating a growing demand for high quality wireless communications. Unfortunately, the current wireless communication infrastructure is not fully equipped to offer these unprecedented data rates and quality of service. The major obstacles include limited bandwidth availability, limited transmit power, and fluctuations in signal strength which are intrinsic to the wireless channel. Future wireless standards are relying on innovative core technologies such as multiple-input multiple-output (MIMO) communications to overcome these problems. The spatial dimension due to antenna arrays at the transmitter and receiver of MIMO communication systems can be exploited by sophisticated signal processing techniques to offer high link capacity, enhanced resistance to interference, and robustness to channel fading.

The benefits of MIMO technology are obtained through a combination of antenna arrays that can provide spatial diversity and algorithms that can adapt to the propagation channel. Antenna arrays have to be designed to be robust in different propagation scenarios and provide the degrees of spatial diversity expected by the algorithms. The algorithms can adaptively reconfigure the transmission methods by tracking the changing channel conditions. The premise of the work presented in this dissertation is that antenna arrays and algorithms at the physical layer can be designed, based on performance metrics from different layers, to exploit the channel spatial selectivity, resulting in improved system performance.

This dissertation presents performance analysis and design methodology of MIMO arrays, employing pattern diversity technique, in spatially correlated channels. The proposed array designs consist of collocated circular patch antennas, or circular patch arrays (CPAs). The benefit of pattern diversity, obtained through CPAs, over conventional space diversity technique is first demonstrated through analysis. Then a novel design methodology for compact MIMO arrays optimized with respect to microwave theory and communication theoretic metrics for given size constraints is proposed. This dissertation also presents adaptive algorithms at the physical layer to switch between different MIMO transmission schemes, based on statistical channel information. These adaptive algorithms exploit the spatial selectivity inherent in the channel and are designed to enhance the spectral efficiency of next generation wireless systems, for predefined target error rate.

Table of Contents

Acknowledgments **v**

Abstract **viii**

List of Tables **xv**

List of Figures **xvi**

Chapter 1. Introduction **1**

1.1 Overview on MIMO Communication Systems 1
1.2 MIMO Antenna and Algorithm Design in Correlated Channels 3
1.3 Summary of the Contributions 5
1.4 Notation 8
1.5 Organization of Dissertation 9

Chapter 2. Background on MIMO Channel Models **10**

2.1 Introduction 10
2.2 Description of Clustered Channel Models 13
2.3 Channel Spatial Selectivity 16
2.4 Analytical Channel Models 17
2.4.1 Deterministic Models 19
2.4.2 Stochastic Models 20

Chapter 3. Benefit of Pattern versus Space Diversity **23**

3.1 Introduction 23
3.1.1 Antenna Diversity Techniques 24
3.1.2 Overview on the Pattern Diversity Analysis 26
3.1.3 System Model 28
3.1.4 Circular Patch Array (CPA) 28

3.2 Spatial Correlation in Single-Cluster Channels 33
3.2.1 Spatial Correlation of the CPA 33
3.2.2 Spatial Correlation of the ULA 36
3.3 Analysis of Pattern and Space Diversity 39
3.3.1 Capacity and Error Rate Performance 40
3.3.2 Eigenvalues of the Spatial Correlation Matrix for the CPA 42
3.3.3 Eigenvalues of the Spatial Correlation Matrix for the ULA 44
3.3.4 Pattern and Space Diversity Tradeoff 45
3.4 Performance Results in Clustered MIMO Channel Models . . . 47
3.4.1 Single-Cluster Channels 47
3.4.2 Double-Cluster Channels 49
3.4.3 IEEE 802.11n Channel Models 50
3.4.4 Performance Results with Mutual Coupling Effects . . . 53

Chapter 4. Design of MIMO Arrays in Clustered Channels 56
4.1 Introduction 56
4.2 Optimization Parameters and Problem Formulation 59
4.2.1 Channel and Antenna Parameters 59
4.2.2 Problem Statement 61
4.3 CPA Analysis in Clustered MIMO Channels 63
4.3.1 Spatial Correlation of CPAs in Multi-Cluster Channels . 63
4.3.2 Eigenvalue Analysis 64
4.3.3 Lower Bound on the Ergodic Capacity 67
4.4 MIMO Communication Performance Metrics 70
4.4.1 Normalized Spatial Correlation 70
4.4.2 CPA Performance in Clustered MIMO Channels 72
4.4.3 Performance Metrics for Optimization Algorithms . . . 75
4.5 Microwave Theory Performance Metrics 80
4.5.1 S-parameters 80
4.5.2 Performance Metrics for Optimization Algorithms . . . 80
4.6 Optimization Algorithm for 2-CPA Designs 81

Chapter 5. Capacity Analysis of Adaptive MIMO Systems 85
5.1 Introduction 85
5.1.1 Background on Adaptive MIMO Systems 86
5.1.2 System and Channel Models 88
5.1.3 MIMO Transmission Techniques 89
5.2 Optimal MIMO Capacity with Covariance Feedback 92
5.3 Closed-form Capacity in Correlated Channels 93
5.3.1 Statistical Beamforming (BF) 94
5.3.2 Orthogonal Space-Time Block Codes (OSTBC) 98
5.3.3 Double Space-Time Transmit Diversity (D-STTD) . . . 101
5.3.4 Spatial Multiplexing (SM) 103
5.4 Relative Capacity Investigation 107
5.4.1 Comparison of BF, D-STTD and SM Ergodic Capacities 108
5.4.2 Capacity Crossing-Points between BF and SM 111
5.4.3 Capacity Crossing-Points between OSTBC and SM . . . 115

Chapter 6. BER Analysis of Adaptive MIMO-BICM Systems 117
6.1 Introduction 118
6.1.1 Background on Adaptive MIMO-BICM Systems 118
6.1.2 System Model and Architecture 120
6.1.3 Low Complexity MIMO Transmission Schemes 122
6.1.4 Low Complexity MIMO-BICM Receivers 123
6.2 Link-Level Capacity of MIMO-BICM 125
6.2.1 Statistical Beamforming (BICM-SB) 126
6.2.2 Zero-Forcing Receivers (BICM-ZF) 127
6.2.3 LLC Performance Comparison 127
6.3 General Expressions for the Error Probability 129
6.3.1 BER Union Bound 130
6.3.2 Exact Expression for the C-PEP 130
6.3.3 Saddlepoint Approximation for the C-PEP 131
6.4 Analysis of MIMO-BICM with Statistical Beamforming 132
6.4.1 Moment Generating Function of Log-Likelihood Metric . 132

6.4.2 Closed-form C-PEP Based on Saddlepoint Approximation 136
6.4.3 Simplified C-PEP 136
6.4.4 BER Performance Results 136
6.5 Analysis of MIMO-BICM with OSTBC 137
6.5.1 Moment Generating Function of Log-Likelihood Metric . 137
6.5.2 Closed-form C-PEP Based on Saddlepoint Approximation 139
6.5.3 Simplified C-PEP 139
6.5.4 BER Performance Results 140
6.6 Analysis of MIMO-BICM with Zero-Forcing Receivers 140
6.6.1 Moment Generating Function of Log-Likelihood Metric . 140
6.6.2 Closed-form C-PEP Based on Saddlepoint Approximation 142
6.6.3 Simplified C-PEP at High SNR 144
6.6.4 BER Performance Results 145

Chapter 7. Practical Adaptive MIMO Algorithms 146
7.1 Introduction 146
7.2 Fundamentals of Adaptive MIMO Systems 148
7.2.1 MIMO Wireless Channels 148
7.2.2 Modulation and Coding Schemes 151
7.2.3 MIMO Schemes 152
7.2.4 Definition of the MIMO Transmission Modes 153
7.3 Adaptive MIMO Transmission Techniques 155
7.3.1 Throughput-Based Adaptive Methods 155
7.3.2 Diversity-Based Adaptive Methods 160
7.3.3 Joint Diversity/Throughput-Based Adaptive Methods . 162
7.4 Adaptation Based on Lookup Tables 162
7.4.1 MIMO Transmission Modes 163
7.4.2 Link-quality Regions and Metrics 163
7.4.3 Generating the Look-up Table 164
7.4.4 Switching Algorithm Operation 165
7.4.5 Simulation Results 166
7.5 Adaptation Based on Closed-form BER with BICM 168

7.5.1 BER Performance Comparison in Correlated Channels . 169
7.5.2 Analytical BICM Switching Scheme 171
7.5.3 Switching Between SB and SM 172
7.5.4 Switching Between OSTBC and SM 176
7.6 Practical Implementation Issues 178

Chapter 8. Conclusions **182**
8.1 Summary 182
8.2 Future Work 183

Appendices **185**

Appendix A. Proof on the Post-Processing SNR of D-STTD **186**

Appendix B. Derivation of Equation (6.51) **188**

Bibliography **190**

Index **218**

Vita **219**

List of Tables

6.1 Breakdown of distance multiplicities between complement BICM subsets for various QAM/PSK constellations with Gray labelling 135

7.1 Modulation/coding schemes (MCSs) as in the IEEE 802.16e standard [1]. 152

7.2 MIMO transmission modes and corresponding values of spectral efficiency (SE). 154

7.3 Selected MIMO transmission schemes in different channel scenarios and SNR conditions. Each propagation scenario is characterized by given channel spatial correlation (CSC) and line-of-sight (LOS) component. The following SNR regions are considered: Low SNR ($<$ 15 dB), Medium SNR ($\simeq$ 20 dB) and High SNR ($>$ 25 dB). 157

7.4 Typical channel scenarios used by our practical adaptive switching algorithm and corresponding values of the link-quality metric (D_λ). 164

List of Figures

1.1 Successive layers of function in a MIMO wireless communication link. 5

2.1 Geometry of the model representing clusters and propagation paths. The angles ϕ_c and ϕ_0 are the mean AOAs of the cluster and propagation paths, respectively. The angle ϕ_i is the AOA offset of the path. 15

3.1 Effective (dashed lines) and physical (solid lines) radius of circular microstrip antennas with $h = 1.575$ mm as a function of the dielectric constant (ϵ_r) of the substrate. 30

3.2 Radiation patterns of circular patch antennas excited with different modes. In each subplot, different colors correspond to the radiation patterns of the 2 antennas of the CPA. 32

3.3 Correlation coefficients for the CPA, with modes 1, 3, 5, and $\sigma_\phi = 20^o$. 37

3.4 Eigenvalues of the correlation matrix for CPA with mode 3 and $\sigma_\phi = 20^o$ 44

3.5 Envelope correlation and ergodic capacity for the ULA with element spacing of $\lambda/2$ and CPA with mode 3. The channel is simulated with $\sigma_\phi = 15^o$ and $\gamma_o = 5$dB. 48

3.6 Ergodic capacity for the ULA with element spacing of $\lambda/2$ and CPA with different mode numbers. The channel is simulated with $\sigma_\phi = 30^o$ and $\gamma_o = 5$dB. 50

3.7 Ergodic capacity for double-cluster channels as a function of the mean azimuth AoAs (ϕ_1 and ϕ_2) of the clusters, with $\sigma_\phi = 30^o$ and $\gamma_o = 5$dB. The CPA is excited with mode 3. 51

3.8 Ergodic capacity and error rate performance for the CPA with mode 3, ULA1 with $d = \lambda/2$ and ULA2 with $d = 2.5\lambda$, in the IEEE 802.11n standard channel models B and E (NLOS). . . . 52

3.9 Ergodic capacity and error rate performance for the CPA with mode 3, ULA1 with $d = \lambda/2$ and ULA2 with $d = 2.5\lambda$, in the IEEE 802.11n standard channel models D and E (LOS). . . . 53

3.10 Ergodic capacity with mutual coupling effects in different channel scenarios, for the CPA with mode 3 and $\tilde{\rho} = 0.41\lambda$, ULA1 with $d = \lambda/2$ and ULA2 with $d = 2.5\lambda$. 54

4.1 Geometry of the 2-CPA design. 60
4.2 Block diagram of the proposed optimization algorithm for MIMO array designs exploiting pattern diversity. 62
4.3 Exact eigenvalue (λ_2) and lower bound in (4.9) as a function of the mean AoAs ϕ_1 and ϕ_2. The channel is simulated with $N_c = 2$, mean AoAs generated in the range $[0, 180^{\text{o}}]$ and $\sigma_\phi = 20^{\text{o}}$. 66
4.4 Exact eigenvalues (λ_1 and λ_2) and bounds in (4.8) and (4.9). The channel is simulated with variable N_c, mean AoAs generated as $\phi_c^{(i)} = \tilde{\phi}(i-1)/N_c$ (with $i = 1, \ldots, N_c$ and $\tilde{\phi} = 120^{\text{o}}$) and variable AS ($\sigma_\phi$). 67
4.5 Exact and lower bounds to the MIMO ergodic capacity as a function of the angle spread (σ_ϕ) and different numbers of clusters (N_c) with $SNR = 20$ dB. The 2-CPA is simulated with $n = 4$. 69
4.6 Ergodic capacity of the CPA as a function of the cluster mean AOA (ϕ_{c}) and per-cluster AS (σ_ϕ), with $SNR = 10$ dB, $\rho_{\text{o}} = 0.45\lambda$ and $\rho_{\text{f}} = 0.64\rho_{\text{o}}$. 74
4.7 Radiation patterns (over the azimuth plane) of the two elements of the CPA for different values of physical radius ρ_{o}, with $\rho_{\text{f}} = 0.64\rho_{\text{o}}$. 74
4.8 Ergodic capacity of the CPA as a function of the cluster mean AOA, with $\sigma_\phi = 20^{\text{o}}$ and $SNR = 10$ dB. 76
4.9 Comparison of different metrics to evaluate the performance of pattern diversity. 78
4.10 Mean and 10% outage capacity as a function of the physical radius (ρ_{o}) and the feed location (ρ_{f}). The mean and 10% outage capacity are computed through (4.19) and (4.20), respectively. The two antennas of the CPA are designed with physical parameters $h = 1.575$ mm and $\epsilon_r = 6$. 79
4.11 Bandwidth BW_{11} and BW_{22} as a function of the radia $\rho_{\text{o}}^{(1)}$ and $\rho_{\text{o}}^{(2)}$ of the two patch antennas of the CPA. The antenna parameters are: $\rho_{\text{f}}^{(1)} = 0.9\rho_{\text{o}}^{(1)}$, $h^{(1)} = 9$ mm, $\epsilon_r^{(1)} = 2.2$, $\rho_{\text{gp}}^{(1)} = 2\rho_{\text{o}}^{(1)}$, $\rho_{\text{f}}^{(2)} = 0.8\rho_{\text{o}}^{(2)}$, $h^{(2)} = 7$ mm, $\epsilon_r^{(2)} = 8$, $\rho_{\text{gp}}^{(2)} = 1.8\rho_{\text{o}}^{(2)}$. 82
4.12 S-parameters for the optimized CPA design with $\rho_{\text{o}}^{(1)} = 0.43\lambda$ and $\rho_{\text{o}}^{(2)} = 0.22\lambda$. 84

5.1 Empirical, exact and upper bound on the ergodic capacity of BF, in *double-sided* correlated channel Model D (NLOS), with different antenna configurations ($N_t \times N_r$). 98

5.2 Empirical, exact and upper bound on the ergodic capacity of OSTBC for 2x2, 2x4 and 2x6 MIMO systems. The exponential model is used, with $\rho_{\text{tx}} = 0.5$ and $\rho_{\text{rx}} = 0.1$. 101

5.3 Empirical, exact and upper bound on the ergodic capacity of $(2 \times N_r)$ SM system with ZF receiver, in *single-sided* correlated channel Model D (NLOS). 107

5.4 Mean capacity for BF, D-STTD (with ZF), SM (with ZF) and optimal transmission in the IEEE 802.11n channel Model F (NLOS). 108

5.5 Mean capacity for BF, D-STTD (with ZF), SM (with ZF) in the IEEE 802.11n channel Models C and F (NLOS). CP1: crossing-point BF versus D-STTD; CP2: crossing-point D-STTD versus SM. 110

5.6 Crossing-points for a MIMO(N_r,2) system as a function of the angular spread (AS) and number of receive antennas (N_r). Single-sided correlated channel with single cluster and mean angle of departure at 0^{o} (broadside direction). 114

5.7 Capacity crossing-points of OSTBC and SM for MIMO 2x2 systems, as a function of the transmit spatial correlation. The channel is single-sided correlated and the exponential model is used, with $\rho_{\text{tx}} = 0.1$ and $\rho_{\text{tx}} = 0.9$. 116

6.1 MIMO-BICM system architecture. 122

6.2 BICM LLC envelope for the ZF and SB transmission schemes. Two MIMO channel scenarios with exponential correlation coefficients $\rho_{\text{tx}} = 0.5, \rho_{\text{rx}} = 0.5$ and $\rho_{\text{tx}} = 0.9, \rho_{\text{rx}} = 0.1$ are considered. 128

6.3 Simulated and analytical BER for 2×2 BICM-SB with a $\frac{1}{2}$ rate code, and for various modulation schemes. An exponential correlation model is used, with correlation coefficient 0.5 at both the transmitter and receiver. 138

6.4 Simulated and analytical BER of 2×2 BICM-OSTBC employing the optimal $\frac{1}{2}$ rate code ($d_{\text{free}} = 10$). The exponential model is used, with $\rho_{\text{tx}} = 0.5$ and $\rho_{\text{rx}} = 0.1$. 141

6.5 Simulated and analytical BER 2×2 BICM-ZF employing a $\frac{1}{2}$ rate code, and for various modulation schemes. An exponential correlation model is used, with correlation coefficient 0.5 at both the transmitter and receiver. 145

7.1 Signal power measured at two different antennas of a MIMO array, with and without channel spatial correlation. The temporal channel fading is due to Doppler effects. 149

7.2 Power angle/delay profile of typical spatially correlated channel environments. 151
7.3 Block diagram of adaptive MIMO communication systems. . . 156
7.4 Spectral efficiency of different MIMO modes in Table 7.2 (defined as combinations of MCSs and MIMO schemes) for practical 4×4 MIMO systems. 159
7.5 Bit error rate (BER) of the adaptive MIMO transmission scheme versus fixed BF, D-STTD and SM with different MCS, in channel Scenario 4. 166
7.6 Spectral efficiency of the adaptive MIMO transmission scheme versus fixed BF, D-STTD and SM with adaptive MCS, in channel Scenario 3 in [2]. 167
7.7 Spectral efficiency of the adaptive MIMO transmission scheme in different channel scenarios. 168
7.8 BER curves based on the tight C-PEP expressions (6.34) and (6.56) for 2×2 BICM-SB and BICM-ZF respectively. Two exponential correlated channel scenarios are presented, with $\rho_{\text{rx}} = 0.1, \rho_{\text{tx}} = 0.3$, and $\rho_{\text{rx}} = 0.1, \rho_{\text{tx}} = 0.7$. 170
7.9 SNR thresholds corresponding to a target BER of 10^{-3} for BICM-ZF and BICM-SB as a function of ρ_{rx} and ρ_{tx}. Results are shown for 2×2 BICM-ZF with 16QAM and a $1/2$ rate code, and BICM-SB with 64QAM and a $2/3$ rate code. 171
7.10 Throughput achieved by the proposed adaptive algorithm for a 2×2 system with target BER of 10^{-3}, and for correlated channels with $\rho_{\text{rx}} = \rho_{\text{tx}} = 0.5$. Mode and transmission scheme selection is based on the tight C-PEP expressions (6.34) and (6.56). Throughputs with optimal mode selection, and LLC envelope curves, are also given. 173
7.11 Throughputs achieved by the proposed adaptive algorithm for a 2×2 system with target BER 10^{-3}, in different exponential correlated channel scenarios, with $\rho_{\text{rx}} = 0.5$, and ρ_{tx} values of $0.1, 0.5$ and 0.9. Mode and transmission scheme selection is based on the tight C-PEP expressions (6.34) and (6.56). . . . 174
7.12 Throughput comparison of two mode/transmission scheme selection approaches. The first is based on the tight C-PEP expressions (6.34) and (6.52), the second is based on the simplified expressions (6.36) and (6.59). Results are shown for 2×2 systems with targets BERs 10^{-3} and 10^{-6}, and for channels with $\rho_{\text{rx}} = \rho_{\text{tx}} = 0.5$. 175

7.13 BER performance for adaptive MIMO 2x2 systems. The BER of OSTBC and SM are obtained from the approximations in (6.43) and [3], respectively. The exponential model is used, with $\rho_{\text{tx}} = 0.1$ and $\rho_{\text{rx}} = 0.05$. 177

7.14 Spectral efficiency for adaptive MIMO 2x2 systems in different propagation scenarios. The MIMO channel is simulated according to the COST-259 physical channel model [4]. Two channel environments are considered: "Pico-cell, GOL" and "Macro-cell, GTU". 178

Chapter 1

Introduction

1.1 Overview on MIMO Communication Systems

Wireless networking and communication is rapidly becoming an intrinsic part of the social and business fabric worldwide. The number of cellular telephone subscribers has surpassed the number of fixed subscribers in many countries in the world and, in next few years, wireless communication is expected to be the preferred method of Internet access [5]. Wireless communication is attractive because it offers flexibility and mobility with moderate infrastructure costs. As wireless communication shifts from a luxury to necessity, expectations about the capabilities of wireless devices are growing. In cellular voice systems, there is a growing resentment towards poor quality by users, who hate dropped calls, and by network providers, who cannot bear the resulting churn of users from their network. In parallel, there is a growing demand for high-speed wireless Internet access in homes and businesses [6, 7] that offers data rates comparable to digital subscriber lines, cable modems, and leased-lines. Unfortunately, current wireless communication systems are not fully equipped to offer quality and data rates that are competitive with wireline systems. The major problems include limited available bandwidth, low transmit power, and signal fading intrinsic to the wireless channel. Fortunately,

innovative technologies such as multiple-input multiple-output (MIMO) communication are being developed to boost quality and capability of wireless links.

A MIMO communication channel is created when there are antenna arrays at both the transmitter and receiver. Through the use of sophisticated signal processing techniques, MIMO communication can offer high link capacity, enhanced resistance to interference, and link robustness or reductions in fading thanks to diversity. Channel capacity represents the number of bits of information per second that can be reliably transmitted over the wireless link within the frequency band of operation. Link robustness is measured by the number of error bits received per unit of time, or bit error rate. These benefits translate into higher data rate transmissions and better coverage. The benefits of MIMO technology are provided by the additional degrees of freedom in multidimensional wireless links not available in single antenna systems. These multiple degrees of freedom can be exploited in different ways through a variety of MIMO transmission techniques. Spatial multiplexing schemes are designed to enable simultaneous transmission of multiple data streams yielding higher capacity than single antenna systems, for the same available bandwidth. Diversity techniques are conceived to reduce the error rate by encoding the same transmit data across different antennas and time slots through space-time encoders.

MIMO communication is taking a central role in all the major next generation wireless standards including IEEE 802.11n for wireless local area

networks (WLANs) [8–10], IEEE 802.16e for wireless metropolitan area networks (WMANs) [11, 12], 3rd generation partnership project (3GPP) [13–15] and 4G communication for next generation of cellular telephony systems.

1.2 MIMO Antenna and Algorithm Design in Correlated Channels

In practical communications systems, the performance of a MIMO link is affected by the spatial distribution of the multipaths in the propagation environment [16]. Multipaths are essentially multiple wavefronts impinging the receive array with different phases and amplitudes, producing random variations in signal strength across different array elements. This channel effect is known as spatial selectivity. When the propagation channel consists only of a few multipaths, the channel fluctuations are statistically less likely to occur and the signals measured at different antennas of the array are "spatially" correlated. Spatial correlation may have adverse effects on the performance of MIMO systems, since it limits the degrees of freedom available in the wireless link. MIMO antenna arrays can be designed to reduce the spatial correlation, producing additional degrees of diversity and improved performance. Similarly, space-time encoders can be conceived to adaptively reconfigure the MIMO arrays, based on the channel spatial correlation, to efficiently utilize the wireless resources.

Antenna arrays and space-time encoders at the physical layer involve different design challenges. The antennas can be treated, in practice, as part

of a separate "layer". Design and analysis of the physical layer involve tools from signal processing and communication theory, whereas the antennas and RF are designed and analyzed using microwave theory and computational electromagnetics. Physical layer performance is measured using bit error rate and capacity. Antenna array performance is measured using bandwidth and antenna gain. The capabilities of the physical layer are constrained by processing capability and power consumption, while the antenna geometry is limited by available surface area and near-field effects such as mutual coupling. The performance metrics and the constraints of each of these layers have no direct connection and conventional designs of single-antenna wireless systems treat them separately. In MIMO systems, however, the physical layer performance is determined in a complex way by algorithms that operate on the multivariate propagation channel as viewed by the transmit and receive arrays. Therefore, MIMO antenna arrays and algorithms can be designed by accounting for metrics derived from different layers.

The motivation for this antenna and algorithm design methodology is the nested dependency between layers as illustrated in Fig. 1.1. The spatial correlation is a function of both channel characteristics (e.g., angle spread, angles of arrival/departure, number of scatterers) and array parameters (e.g., array geometry, element spacing, element pattern, polarization, mutual coupling), and affects the performance of the space-time processors at the physical layer. Hence, the antenna arrays can be designed, based on metrics from both microwave theory (i.e., bandwidth, antenna gain) and communication the-

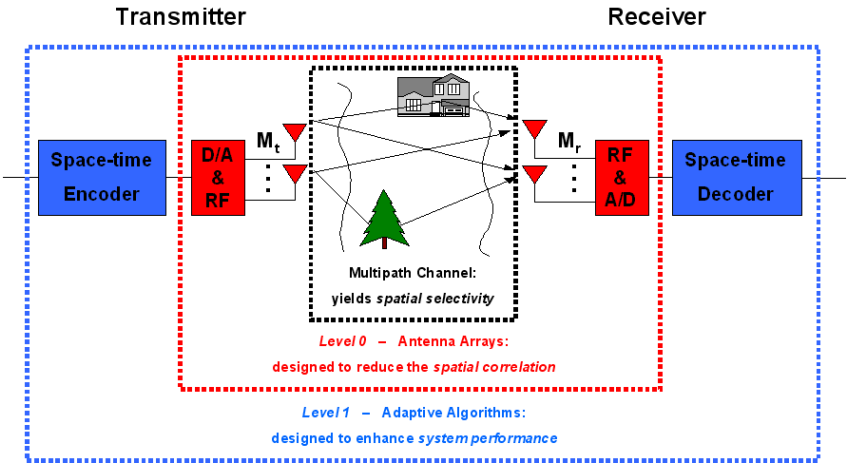

Figure 1.1: Successive layers of function in a MIMO wireless communication link.

ory (i.e., capacity, error rate), to reduce the spatial correlation resulting in improved system performance. Similarly, the adaptive algorithms can be conceived to switch between different MIMO schemes and array configurations, thus exploiting the spatial selectivity of the channel, yielding enhancement in spectral efficiency.

1.3 Summary of the Contributions

Several *antenna array* designs for MIMO systems have been suggested in the past few years, by employing space/polarization/pattern diversity techniques. Space diversity is enabled by antennas placed far apart to produce uncorrelated signals across different array sensors and their performance have been widely analyzed in [16–24]. To exploit polarization and pattern diversity, the antennas are designed to radiate with orthogonal polarizations and radiation patterns as a means to create uncorrelated channels across differ-

ent array elements. The benefits of polarization/pattern diversity have been demonstrated through analysis and measurements in [25–31]. Previous works, however, do not analyze the effect of the antenna radiation patterns on the capacity and error rate performance of pattern diversity. Moreover, though different MIMO antenna designs have been proposed thus far, the current literature has not proposed design criteria and methodology for MIMO arrays accounting for the channel effects. Both these problems are studied in this dissertation.

The diversity provided by the channel through the antenna arrays can be exploited in a MIMO system by the use of *space-time encoders* at the transmitter, and space-time processing at the receiver as a means to enhance system performance. Different MIMO space-time techniques have been designed to provide capacity gain through spatial multiplexing [32–34] or diversity advantage through orthogonal space-time block codes (OSTBC) [35–37]. Recently a new scheme called double space-time transmit diversity (D-STTD) has been proposed in [38] to obtain both capacity and diversity gains. Another common MIMO transmission technique is beamforming [39, 40], where single data stream is weighted by the coefficients of a spatial filter and transmitted over all the antennas. Adaptive switching between these MIMO schemes is a key solution to further exploit the diversity of the channel and provide additional gains in spectral efficiency. This dissertation also proposes new analysis and practical designs of adaptive transmission methods that switch between different MIMO schemes to enhance the spectral efficiency of wireless systems.

We summarize the main contributions presented in this dissertation as follows:

1) Analysis and design of MIMO arrays of circular patch antennas exploiting pattern diversity. This item includes:

- New closed-form expressions of the spatial correlation coefficients of arrays of circular patch antennas in spatially correlated MIMO channel models.
- New closed-form expressions of the spatial correlation coefficients of uniform linear arrays in correlated channels. These expressions are used for studies on pattern diversity.
- Analysis of the benefit of pattern over space diversity techniques in realistic channel models. The performance of pattern diversity is evaluated as a function of the antenna radiation patterns.
- New metrics to evaluate the performance of MIMO arrays, exploiting pattern diversity, that account for channel clustering.
- Novel design methodology for MIMO arrays, exploiting pattern diversity, in correlated channel models. We present the problem statement and solution of the proposed optimization algorithm for arrays of circular patch antennas.

2) Analysis and design of adaptive MIMO algorithms exploiting the spatial selectivity of MIMO channels. This item includes:

- New closed-form capacity expressions for different MIMO schemes in spatially correlated channels.
- Capacity tradeoffs between different MIMO transmission schemes.
- New closed-form expressions of the error rate performance for different MIMO schemes in spatially correlated channels.
- Practical adaptive MIMO transmission algorithm exploiting the spatial selectivity of wireless channels. Two different techniques are proposed for practical implementations of this adaptive algorithm.

The proposed solutions and techniques may be directly applicable to future MIMO wireless systems that are currently in the process of being standardized by IEEE 802.11n, IEEE 802.16e and 3GPP standard bodies.

1.4 Notation

This section gives the notation used throughout this proposal. We use $\mathcal{CN}(0,1)$ to denote a random variable with real and imaginary parts that are i.i.d. according to $\mathcal{N}(0,1/2)$; $\mathbb{C}^{m\times n}$ to denote a complex matrix with dimensions $m \times n$, * to denote conjugation; ^{T} to denote transposition, † to denote conjugation and transposition; $|\cdot|$ to denote the absolute value; $||\cdot||_2$ to denote the vector two-norm; $\langle\cdot,\cdot\rangle$ to denote the complex vector space inner-product; $*$ to denote the convolution; $\otimes$ to denote the Kronecker product; and $\mathcal{E}[\cdot]$ to denote the ensemble average.

1.5 Organization of Dissertation

Chapter 2 presents an overview on correlated MIMO channel models, used for analysis and performance evaluation of the antenna/algorithm designs presented in this dissertation. Chapter 3 presents analytical results describing the benefit of pattern over space diversity. Chapter 4 describes the novel design methodology for MIMO arrays exploiting pattern diversity. The capacity analysis of adaptive MIMO systems is given in Chapter 5, while the BER analysis is reported in Chapter 6. Chapter 7 presents the practical adaptive algorithm with applications to the IEEE 802.16e standard. Finally, conclusions are drawn in Chapter 8.

Chapter 2

Background on MIMO Channel Models

Channel models are one essential component in systems analysis in that they enable performance prediction and comparison of different systems designs in realistic propagation environments. This chapter first provides an overview on clustered spatial channel models that are used to predict the performance of the antenna and algorithm designs proposed in this dissertation. Then it describes the concept of spatial selectivity that is exploited by the proposed designs. Finally, it reviews analytical models for deterministic and stochastic MIMO channel models.

2.1 Introduction

Spatially correlated MIMO channels are typically derived under certain assumptions about the scattering in the propagation environment. One popular correlation model, which we call the clustered channel model, assumes that groups of scatterers are modeled as clusters located around the transmit and receive antenna arrays. Clustered channel models have been validated through measurements [41, 42] and variations have been adopted in different standards such as the *IEEE 802.11n* Technical Group (TG) [43], for wireless local area

networks (WLANs), and the *3GPP* Technical Specification Group (TSG) [44], for third generation cellular systems.

There are two popular approaches to simulate correlated MIMO channels based on methods derived from single-input multiple-output (SIMO) channel models (see [45] and the references therein). The first one is a *deterministic* approach, which generates the MIMO channel matrix based on a geometrical description of the propagation environment (i.e., ray-tracing techniques). The second one is a *stochastic* method, where the spatial correlation across MIMO channels is reproduced by a suitable choice of transmit and receive spatial correlation matrices. Deterministic models are used to predict the performance of MIMO communication systems in realistic propagation environments, since they describe accurately the spatial characteristics of wireless links. Stochastic models (ex. the Kronecker model [16, 46]) are defined using a reduced set of channel parameters (i.e., angle spread, mean angle of arrival/departure) and are suitable for theoretical analysis of correlated MIMO channels.

In theoretical analyses of MIMO systems, it may be desirable to study capacity and error rate performance accounting for spatial correlation effects, due to the propagation channel and the transmit/receive arrays. For this purpose, the channel spatial correlation has to be expressed in closed-form as a function of channel and array parameters. In [47], exact expressions of the spatial correlation coefficients were derived for different spatial distributions (i.e., uniform, Gaussian, Laplacian) of angles of departure/arrival for uniform linear arrays (ULAs). This solution, however, is expressed in terms of sums of Bessel

functions and does not show a direct dependence of the spatial correlation on the channel/array parameters.

In this chapter, we propose new closed-form expressions of the spatial correlation matrices in clustered MIMO channels. We assume a Laplacian distribution of the angles of arrival/departure, which has been demonstrated to be a good fit for the power angular spectrum [48–51] and is practically used by different standards channel models [4,43,44]. The key insight is that a small angle approximation, which holds for moderate angle spreads (i.e., less than $\sim 10^{o}$), allows us to derive a closed-form solution for the spatial correlation function. Using our method, we can avoid the numerical integration in [47] and can easily obtain the correlation as a function of angle spread and arrivals. We develop these results for the commonly used uniform linear array (ULA) and extend these results to the uniform circular array (UCA), perhaps the next most common array geometries for future generation access points. To validate our model, we compare it against existing deterministic and stochastic channel models. To make the comparison, we propose a novel distance metric, derived from the mutual information of the MIMO channel, to evaluate the relative performance of deterministic and stochastic channel models. Then we evaluate this metric in different propagation conditions and show that, for angle spreads lower than $\sim 10^{o}$, our model is a good fit to the more realistic deterministic models.

Besides the analytical tractability, another main benefit of the proposed method versus existing channel models, as we demonstrate, is a reduction in

computational complexity and thus computation time required to compute the spatial correlation matrices. Because the spatial correlation matrices are a function of the cluster size and location, which are often modelled as random, system level simulations will require averaging over many correlation realizations. For example, in the context of network simulators, where many users and channels need to be simulated [52–59], and in detailed propagation studies of the effect of correlation [60, 61], the computational burden to simulate spatially correlated MIMO channels is a relevant issue. Our proposed channel model enables network simulations with significant computational saving, on the order of 10 to 1000 times compared to existing methods.

2.2 Description of Clustered Channel Models

One common technique for modeling multi-path propagation in indoor environments is the Saleh-Valenzuela model [41,62], where waves arriving from similar directions and delays are grouped into clusters. Using this method, a mean angle of arrival (AOA) or departure (AOD) is associated with each cluster and the AOAs/AODs of the sub-paths within the same cluster are assumed to be distributed according to a certain probability density function (pdf). The pdf of the AOAs/AODs is chosen to fit the empirically derived angular distribution of the AOAs/AODs, or power angular spectrum (PAS), of the channel. The size of a cluster is measured by the cluster angular spread (AS) defined as the standard deviation of the PAS.

We denote the PAS with $S_\Omega(\Omega)$, where $\Omega = (\phi, \theta)$ is the solid angle,

ϕ is the azimuth angle and θ is the elevation angle. Note that the PAS over the θ angles is generally assumed to be independent from the ϕ angles [4], and we write $S_\Omega(\Omega) = S_\phi(\phi)S_\theta(\theta)$. Moreover, although the AOAs/AODs are physically distributed over the three dimensional space, it has been proven through channel measurements that most of the energy is localized over the azimuth directions [4]. Under this assumption, we define $S_\phi(\phi) = P_\phi(\phi) * \delta(\phi - \phi_c)$, with $\delta(\phi)$ being the delta function and ϕ_c the mean angle of arrival of the cluster, and $S_\theta(\theta) = \delta(\theta - \pi/2)$ to simplify our analysis.

A graphical representation of the clustered channel model is given in Fig. 2.1 for the two dimensional space. Without loss of generality, we focus on modeling the receiver spatial correlation. Multiple scatterers around the receive array are modeled as clusters. We use the angle ϕ_{c} to denote the mean AOA of one cluster. Within the same cluster, each propagation path is characterized by an angle of arrival ϕ_0 and is generated according to a certain PAS. Depending on the system bandwidth, the excess delay across different paths may not be resolvable. In this case, multiple AOAs are defined with an offset ϕ_i relative to the mean AOA of the propagation path (ϕ_{c}). In typical channel models for indoor environments [43], the propagation paths within the same clusters are generated with the same mean AOA as the cluster and we assume $\phi_0 = \phi_{\mathrm{c}}$.

Several distributions have been proposed thus far to approximate the empirically observed PAS: the n-th power of a cosine function and uniform distributions [63–66], the Gaussian probability density function (pdf) [67], and

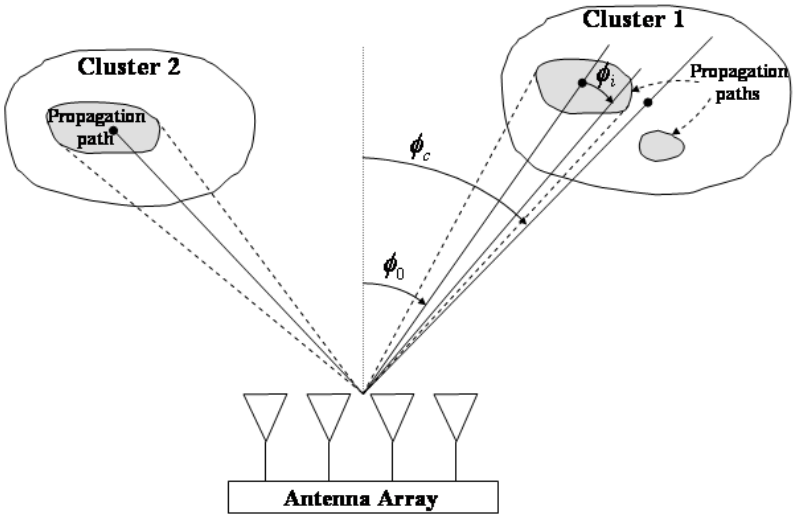

Figure 2.1: Geometry of the model representing clusters and propagation paths. The angles ϕ_c and ϕ_0 are the mean AOAs of the cluster and propagation paths, respectively. The angle ϕ_i is the AOA offset of the path.

the Laplacian pdf [49–51, 62, 68–70]. Through recent measurement campaigns in indoor [50,51,62,69] and outdoor [48,49,68] environments, it has been shown that the PAS is accurately modelled by the truncated Laplacian pdf, given by

$$P_\phi(\phi) = \begin{cases} \frac{\beta}{\sqrt{2}\sigma_\phi} \cdot \mathrm{e}^{-|\sqrt{2}\phi/\sigma_\phi|} & \text{if } \phi \in [-\pi, \pi); \\ 0 & \text{otherwise} \end{cases} \tag{2.1}$$

where ϕ is the random variable describing the AOA offset with respect to the mean angle ϕ_c, σ_ϕ is the standard deviation (RMS) of the PAS, and $\beta = 1/(1 - \mathrm{e}^{-\sqrt{2}\pi/\sigma_\phi})$ is the normalization factor needed to make the function integrate to one. The Laplacian pdf is also used by different standards bodies as in

[4, 43, 44].

2.3 Channel Spatial Selectivity

The spatial selectivity is the result of multipath waves impinging the receiver from different spatial directions [71]. The impinging wavefronts add up constructively and destructively at the receiver, such that the received signal changes randomly from one location to the other as the receiver moves. In MIMO communication systems the effect of the channel spatial selectivity is to create uncorrelated signals across different antennas of the array, which yields spatial diversity.

An analytical and intuitive description of the channel spatial selectivity has been given in [72] through the theory of the multipath shape factors. The multipath shape factor are derived from the Fourier coefficients of the PAS given by

$$F_n = \int_0^{2\pi} P_\phi(\phi) \mathrm{e}^{jn\phi} \mathrm{d}\phi \tag{2.2}$$

where $P_\phi(\phi)$ is the PAS given in (2.1) for Laplacian distributed AoAs. There are three different shape factors defined as [72]

$$\Lambda = \sqrt{1 - \frac{|F_1|^2}{F_0^2}} \quad \gamma = \frac{|F_0 F_2 - F_1^2|}{F_0^2 - |F_1|^2} \quad \phi_{\max} = \frac{1}{2} \arg\left[F_0 F_2 - F_1^2\right] \tag{2.3}$$

where Λ is the angular spread, γ is the angular constriction (a measure of the concentration of the multipaths around two azimuth directions) and $\phi_{\max}$ is the azimuthal direction of maximum fading (an orientation parameter). By definition, these three parameters depend on the distribution of the PAS, which

describes the spatial properties of the propagation channels, and are indicators of the channel spatial selectivity. Note that, the spatial correlation in MIMO systems is the effect produced by the channel spatial selectivity and is also a function of the array parameters as shown later in equation (2.14). The antenna array may be designed to reduce the spatial correlation by exploiting different diversity techniques described in the Chapter 3.

2.4 Analytical Channel Models

This section provides analytical models for the clustered channel model described above. Consider a MIMO communication link with N_t transmit and N_r receive antennas. Suppose that the system is wideband and operating in an indoor environment that is accurately modeled using the clustered channel model. Under this assumption, the channel consists of multiple sample taps that are associated with different clusters. Because the transmitted signals are bandlimited, it is sufficient to model only the discrete-time impulse response (see e.g. [73])

$$\mathbf{H}[t] = \sum_{\ell=0}^{L-1} \mathbf{H}_\ell[t]\ \delta[t-\ell] \tag{2.4}$$

obtained from sampling the band-limited continuous-time impulse response where t denotes the discrete-time index, L is the number of effectively nonzero channel taps, $\delta[t-\ell]$ is the Kronecker delta function[1], and $\mathbf{H}_\ell[t]$ is the $N_r \times N_t$

[1]The Kronecker delta is defined as

$$\delta[t-\ell] = \begin{cases} 1 & \text{if } t = \ell; \\ 0 & \text{otherwise.} \end{cases}$$

channel matrix for the ℓ-th tap. We assume that the taps are uncorrelated and we focus now on modeling each channel tap. To simplify the notation, we omit the index n assuming to model the channel at a given time instant.

Each channel tap consists of a fixed or line-of-sight (LOS) component $\overline{\mathbf{H}}_\ell$ and a scattered or non-LOS (NLOS) component $\widetilde{\mathbf{H}}_\ell$ and can be written as [33]

$$\mathbf{H}_\ell = \sqrt{\frac{K}{K+1}}\overline{\mathbf{H}}_\ell + \sqrt{\frac{1}{K+1}}\widetilde{\mathbf{H}}_\ell \tag{2.5}$$

where K is the Rician K-factor. Note that, for the most practical channel models [43, 44] the LOS component is associated only to the first (earliest) channel tap.

We assume the LOS component of the channel to be rank one and we generate it as [43, 74]

$$\overline{\mathbf{H}}_\ell = \mathbf{a}_r(\Omega_r) \cdot \mathbf{a}_t^\dagger(\Omega_t) \tag{2.6}$$

where $\mathbf{a}_t(\Omega)$ and $\mathbf{a}_r(\Omega)$ are the transmit and receive array responses, respectively, while Ω_t and Ω_r are the angles of departure/arrival corresponding to the LOS component at the transmitter and receiver sides, respectively. To model the NLOS component there are essentially two different methods: *deterministic* and *stochastic* channel models. Hereafter, we briefly describe each of them.

2.4.1 Deterministic Models

In deterministic channel models the entries of the MIMO channel matrix are expressed as a function of the channel spatial parameters. The ℓ-th matrix tap $\mathbf{H}_\ell$ is given by [75, 76]

$$\widetilde{\mathbf{H}}_\ell = \frac{1}{\sqrt{N}} \sum_{i=1}^{N} \alpha_i \mathbf{a}_{\mathrm{r}}(\phi_{\ell,i}^{\mathrm{r}}) \mathbf{a}_{\mathrm{t}}^{\dagger}(\phi_{\ell,i}^{\mathrm{t}}) \tag{2.7}$$

where N is the number of rays per cluster, α_i is the complex Rayleigh channel coefficient, $\phi_{\ell,i}^{\mathrm{t}}$ and $\phi_{\ell,i}^{\mathrm{r}}$ are the AOD and AOA, respectively, of the i-th ray within the ℓ-th cluster, generated according to the Laplacian pdf in (2.1). Moreover, $\mathbf{a}_{\mathrm{t}}$ and $\mathbf{a}_{\mathrm{r}}$ are the transmit and receive array responses, respectively, given by

$$\mathbf{a}_{\mathrm{t}}(\phi_{\ell,i}^{\mathrm{t}}) = \left[1,\ \mathrm{e}^{j\Phi_1(\phi_{\ell,i}^{\mathrm{t}})},\quad \cdots\quad , \mathrm{e}^{j\Phi_{(N_t-1)}(\phi_{\ell,i}^{\mathrm{t}})}\right]^T \tag{2.8}$$

$$\mathbf{a}_{\mathrm{r}}(\phi_{\ell,i}^{\mathrm{r}}) = \left[1,\ \mathrm{e}^{j\Phi_1(\phi_{\ell,i}^{\mathrm{r}})},\quad \cdots\quad , \mathrm{e}^{j\Phi_{(N_r-1)}(\phi_{\ell,i}^{\mathrm{r}})}\right]^T \tag{2.9}$$

where Φ_m is the phase shift of the m-th array element with respect to the reference antenna. Note that the expression of Φ_m varies depending on the array configuration and is a function of the AOA/AOD. Equation (2.7) can be written in closed-form as [77](p.31)

$$\widetilde{\mathbf{H}}_\ell = \mathbf{A}_{\mathrm{r},\ell} \mathbf{H}_\alpha \mathbf{A}_{\mathrm{t},\ell}^{\dagger} \tag{2.10}$$

where $\mathbf{A}_{\mathrm{t},\ell} = [\mathbf{a}_{\mathrm{t}}(\phi_{\ell,1}), ..., \mathbf{a}_{\mathrm{t}}(\phi_{\ell,N})]$, $\mathbf{A}_{\mathrm{r},\ell} = [\mathbf{a}_{\mathrm{r}}(\phi_{\ell,1}), ..., \mathbf{a}_{\mathrm{r}}(\phi_{\ell,N})]$ and $\mathbf{H}_\alpha = 1/\sqrt{N}\mathrm{diag}\,(\alpha_1, ..., \alpha_N)$. We define the channel covariance matrix for the ℓ-th tap as

$$\mathbf{R}_{H,\ell} = \mathcal{E}\left[\mathrm{vec}(\widetilde{\mathbf{H}}_\ell)\mathrm{vec}(\widetilde{\mathbf{H}}_\ell)^{\dagger}\right]. \tag{2.11}$$

2.4.2 Stochastic Models

We use the Kronecker model to describe the stochastic evolution of each matrix tap $\widetilde{\mathbf{H}}_\ell$ as [16]

$$\widetilde{\mathbf{H}}_\ell = \mathbf{R}_\ell^{1/2} \mathbf{Z} \mathbf{S}_\ell^{1/2} \tag{2.12}$$

where $\mathbf{Z}$ is a $N_r \times N_t$ matrix whose entries are independently distributed according to the complex Gaussian distribution. Moreover, $\mathbf{R}_\ell$ and $\mathbf{S}_\ell$ are the spatial correlation matrices at the transmitter and receiver, respectively, which express the correlation of the receive/transmit signals across the array elements. The channel covariance matrix of the stochastic model in (2.12) is given by the Kronecker product of the transmit and receive correlation matrices as

$$\mathbf{R}_{H,\ell} = \mathbf{S}_\ell \otimes \mathbf{R}_\ell. \tag{2.13}$$

Note that the Kronecker model in (2.12) assumes separability between transmit and receive spatial correlation, and has been shown through measurements to underestimate the actual MIMO channel capacity [78–81]. In this dissertation, however, we employ the model in (2.12) since it simplifies the performance analysis of our MIMO antenna and algorithm designs in spatially correlated channels. Moreover, the Kronecker structure has been adopted by the IEEE 802.11n channel model [43], that we use to evaluate the performance of our designs in realistic indoor propagation environments. Contrarily to [43], we do not model the power delay profile (i.e., narrowband assumption) and

Doppler effects, since we aim to measure the performance gains due to the spatial diversity provided by the proposed antenna and algorithm designs, when no time/frequency diversity is available in the system. To validate our designs, we also measure their performance in more realistic channel models described in Section 2.4.1, as shown in the following chapters.

In clustered channel models, the coefficients of $\mathbf{R}_{\mathrm{t}}$ and $\mathbf{R}_{\mathrm{r}}$[2], for a single channel tap are characterized by a certain angular spread and angle of arrival. Since the same method is used to calculate each correlation matrix, we will use the notation $\mathbf{R}$ to refer to both the transmit or receive correlation matrix. Likewise, we will use M, instead of N_r or N_t, to indicate the number of antennas. The (m,n) entry of the matrix $\mathbf{R}$ for spaced array configurations is defined as [47, 68]

$$r_{m,n} = \int_{4\pi} S_{\Omega}(\Omega)\underline{E}_m(\Omega)\underline{E}_n^*(\Omega)\mathrm{e}^{j\Psi_{m,n}(\Omega)}d\Omega \tag{2.14}$$

where $S_{\Omega}(\Omega)$ is the Laplacian pdf in (2.1) and the term $\Psi_{m,n}(\Omega) = \Psi_m(\Omega) - \Psi_n(\Omega)$ accounts for the phase difference between the m-th and n-th array element due to spacing. Note that, for two dimensional channel models, we refer to the phase term in (2.14) as $\Phi_{m,n}(\phi) = \Phi_m(\phi) - \Phi_n(\phi)$.

We observe that the spatial correlation in (2.14) is a function of the *channel* characteristics through $S_{\Omega}(\Omega)$, and *antenna array* parameters such as polarization, radiation pattern through $\underline{E}_m(\Omega)$ and element spacing through $\Psi_{m,n}(\Omega)$. Then, equation (2.14) suggests that the array parameters can be

[2]We omit the subscript ℓ because we focus on a single tap.

tuned as a function of the channel parameter to reduce the spatial correlation, resulting in improved system performance. This dependence is exploited by the cross-layer antenna/algorithm design methodology described in the Chapter 3.

In performance analyses of MIMO systems, it is sometime convenient to express the entries of spatial correlation matrix as a function of a single correlation parameter. For this reason we define the (non-physical) exponential correlation model at the transmitter and receiver as

$$[\mathbf{R}]_{m,n} = \rho_{\text{rx}}^{|m-n|} \qquad\qquad [\mathbf{S}]_{m,n} = \rho_{\text{tx}}^{|m-n|} \tag{2.15}$$

where ρ_{rx} and ρ_{tx} are the receive and transmit spatial correlation coefficients between adjacent antennas. We will use this model to evaluate the performance of adaptive MIMO algorithms described in the Chapters 5, 6 and 7.

Chapter 3

Benefit of Pattern versus Space Diversity

MIMO arrays can be designed to reduce the spatial correlation between different antenna elements, resulting in improved system performance. There are three main antenna diversity techniques commonly employed in MIMO array design: space, polarization and pattern diversity. This chapter demonstrates the benefits of pattern versus space diversity in clustered channel models, described in Chapter 2. It first reviews different antenna diversity techniques and the properties of circular patch antenna arrays, yielding pattern diversity. It then analyzes the spatial correlation and performance tradeoffs of pattern and space diversity in clustered MIMO channel models. Finally, the performance of circular patch arrays in realistic propagation environments is shown through Monte Carlo simulations.

3.1 Introduction

This section first reviews different antenna diversity techniques for MIMO array designs. Then it provides an overview on the proposed analysis of pattern diversity. Finally the system model and properties of arrays of circular patch antennas are described.

3.1.1 Antenna Diversity Techniques

Different antenna diversity techniques have been proposed thus far to reduce the spatial correlation across different array elements. The most common techniques are: space, polarization and pattern diversity, described in [82–85].

Space diversity is enabled by spacing the antennas far apart, such that the propagation multipaths impinge different array elements with different phases, producing uncorrelated signal across different antennas.

Polarization diversity is determined by cross-polarized antennas that receive multipaths with different polarizations, yielding uncorrelated signals across different array elements.

Pattern diversity is created when the antennas have orthogonal radiation patterns to produce uncorrelated channels across different array elements.

For arrays of uniformly spaced antennas, the throughput that a MIMO channel can support depends on element spacing [16–18], number of antennas [19, 20], array aperture [21, 22], and array geometry [16, 23, 24]. Depending on the spatial characteristics of the MIMO channel, the distance between the array elements needs to be multiple of the wavelength to ensure good system performance, as shown in [16–18, 24]. In typical MIMO systems, size and cost constraints often prevent the antennas from being placed far apart (i.e.,

antenna placement in notebook computers or mobile phones). Therefore, space diversity techniques may be insufficient for next generation wireless handsets.

Alternative techniques for reducing array size are multimode diversity [86, 87] and polarization/pattern diversity [25–31, 88–91]. Multimode diversity exploits the difference in radiation patterns of higher order modes to produce low correlated channels across the modes. Practical solutions to exploit multimode diversity are biconical antennas [86] and spiral antennas [87]. While these solutions provide significant diversity gain, they do not aim to reduce the array size and therefore are not suitable for miniaturized designs for handsets or notebook computers. To exploit polarization and pattern diversity, the antennas are designed to radiate with orthogonal radiation patterns and polarizations as a means to create uncorrelated channels across different array elements. Polarization diversity has already been explored in [25–28] and its benefits on system performance have been verified through experimental channel measurements in [92–95]. The benefits of pattern diversity have been shown through practical measurements with array designs employing tri-monopole collocated antennas [31], switched parasitic antennas [29, 30] and dipoles with 90° hybrid [90]. The results in [29–31, 90], however, do not give insights on the performance of MIMO arrays employing pattern diversity as a function of the antenna radiation patterns. In this chapter we will show analytically and through simulations that the performance of these arrays is in fact sensitive to the shape of the antenna radiation patterns and will provide design criteria for arrays using pattern diversity.

3.1.2 Overview on the Pattern Diversity Analysis

We analyze MIMO arrays consisting of collocated circular microstrip antennas. These MIMO arrays exploit pattern diversity without requiring excessive real estate for spacing the antennas. Different modes can be excited inside the microstrip, yielding different capacity/error-rate performance. We will only consider 2-element arrays, where the antennas have the same polarization, to isolate the effect of pattern from polarization diversity. We assume the circular patch antennas are collocated to measure the effect of pattern diversity, when no space diversity is available.

We first study the performance of this circular patch array (CPA) as a function of the physical antenna parameters. In particular, we show that increasing the number of lobes in the antenna radiation patterns (obtained by exciting higher order modes of the CPA) yields higher degree of diversity and better throughput. This result can be used as general design guideline for MIMO array solutions with pattern diversity. Then, we compare the performance of the CPA against a conventional 2-element uniform linear array (ULA) to determine the benefit of pattern over space diversity. We choose the element spacing of the ULA to be greater than half wavelength to reduce pattern distortion due to mutual coupling [30] and measure only the effect of space rather than pattern diversity. We show that the CPA outperforms the ULA with $\lambda/2$ element spacing in any channel scenario. Moreover, the CPA yields similar performance as the ULA with 2.5λ spacing, while satisfying more restrictive size constraints. In this chapter we do not compare the

performance of the CPA against other array solutions for pattern diversity proposed in [29–31, 90]. In fact, our aim is to propose general design criteria and study the theoretical benefits of pattern over space diversity, rather than compare the performance of a practical MIMO array against existing designs.

To enable this theoretical analysis, we derive the exact expression for the spatial correlation coefficients of the CPA for typical clustered MIMO channels, assuming Laplacian distributed angles of arrival/departure. These correlation coefficients are useful tools to study pattern diversity. We employ these coefficients to derive the eigenvalues of the spatial correlation matrix as a function of the antennas and channel parameters for both the CPA and ULA. Then we use these eigenvalues to analytically compute a tradeoff between pattern and space diversity. We express this tradeoff in terms of mode number of the CPA and element spacing of the ULA, showing a theoretical condition for which pattern diversity is more effective than space diversity. We present the performance results in the context of typical channel models for indoor environments, defined by the IEEE 802.11n standard channel model [43] for wireless local area networks (WLANs). Finally, we show how these performance results vary under the effect of mutual coupling across the antennas.

3.1.3 System Model

We model the receive signal of a narrowband MIMO system, with N_t transmit antennas and N_r receive antennas, as

$$\mathbf{y} = \sqrt{\frac{\gamma_o}{N_t}}\,\mathbf{H}\mathbf{x} + \mathbf{n} \tag{3.1}$$

where γ_o is the average signal-to-noise ratio (SNR), $\mathbf{y} \in \mathbb{C}^{N_r \times 1}$ is the receive signal vector, $\mathbf{x} \in \mathbb{C}^{N_t \times 1}$ is the transmit signal vector normalized such that $\mathcal{E}\{||\mathbf{x}||_2^2\} = N_t$), $\mathbf{n} \in \mathbb{C}^{N_r \times 1}$ is the zero-mean additive Gaussian noise with covariance matrix $\mathcal{E}\{\mathbf{n}\mathbf{n}^H\} = \mathbf{I}_{N_r}$ and $\mathbf{H} \in \mathbb{C}^{N_r \times N_t}$ is the MIMO channel matrix.

3.1.4 Circular Patch Array (CPA)

The properties of circular microstrip antennas and annular patch structures have been studied in [96–99]. In [96] it was shown that, by exciting different modes of circular patch antennas, it is possible to obtain different radiation properties. In addition, by varying the size of the antennas as well as the feed location, different polarizations and radiation patterns can be generated in far-field. In this chapter we use the orthogonality of the radiation patterns of circular patch antennas as a means to reduce correlation between the diversity branches of the MIMO array.

We express the electric field of n-th mode excited inside the circular patch antenna as a function of its θ and ϕ far-field components as

$$E_\theta^{(n)}(\phi,\theta) = e^{jn\pi/2}\frac{V_0^{(n)}}{2}k_0\rho\left(J_{n+1} - J_{n-1}\right)\cos\left[n(\phi-\phi_0)\right] \tag{3.2}$$

$$E_{\phi}^{(n)}(\phi,\theta) = -e^{jn\pi/2}\frac{V_0^{(n)}}{2}k_0\rho\left(J_{n+1}+J_{n-1}\right)\cos\theta\sin\left[n(\phi-\phi_0)\right] \tag{3.3}$$

where $V_0^{(n)}$ is the input voltage, k_0 is the wavenumber, $J_n = J_n(k_0\rho\sin\theta)$ is the Bessel function of the second kind and order n, ρ is the radius of the microstrip antenna and ϕ_0 is the reference angle corresponding to the feed point of the antenna [96]. Different radii are defined for different modes to resonate at a given frequency, according to the following formula [98]

$$\bar{\rho} = \frac{\chi_n'\lambda}{2\pi\sqrt{\epsilon_r}} \tag{3.4}$$

where λ is the wavelength (corresponding to the carrier frequency of the system), ϵ_r is the dielectric constant of the substrate of the microstrip and χ_n' is the first zero of the derivative of the Bessel function J_n. Since the values of χ_n' increase as a function of n (for $n \geq 1$), equation (3.4) suggests that for fixed λ and ϵ_r, the size of the circular patch becomes larger for the higher modes. Therefore, higher order modes are impractical for designs with restrictive size constraint. We will account for this constraint in our analysis and determine the mode number that provides good size/performance tradeoff.

The effective radius ($\bar{\rho}$) in (3.4) does not account for fringing effects, and the physical radius (ρ_{o}) of the circular patch antenna may be smaller than (3.4), depending on the height of the microstrip. In the design of the CPA it is possible to predict the physical radius of the circular patch antenna from the effective radius by solving the recursive formula in [98, p.755]. For a circular patch antenna with height $h = 1.575$ mm, we compute the effective and physical radius as a function of the dielectric constant (ϵ_r) of the substrate

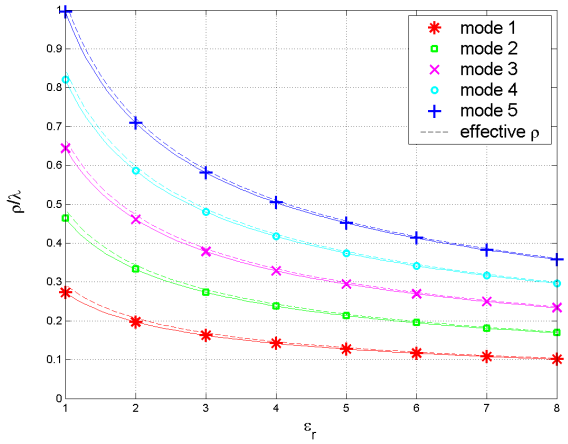

Figure 3.1: Effective (dashed lines) and physical (solid lines) radius of circular microstrip antennas with $h = 1.575$ mm as a function of the dielectric constant (ϵ_r) of the substrate.

as in Fig. 3.1. Note that the values of ρ_o in Fig. 3.1 do not account for possible coupling effects that manifest when two microstrip antennas are collocated, as in our CPA designs. Finding the value of ρ_o that optimizes the performance of CPAs is one of the goals of the optimization algorithm proposed in this dissertation.

To isolate the effect of pattern from space diversity, we assume the patch antennas are collocated and stacked on top of each other, as described in [97]. We excite the same mode for both the elements of the MIMO array and tune the phase ϕ_0 to produce orthogonal radiation patterns across the diversity branches. For the case of a 2-element MIMO array, we feed one antenna with $\phi_0^{(1)} = 0$ and the other antenna with $\phi_0^{(2)} = \pi/(2n)$. As result of this feeding

technique, we get orthogonal radiation patterns for any mode excited within the antennas, as depicted in Fig. 4.7. Note that we discard "mode 0" since it does not yield any pattern diversity due to its isotropic radiation pattern over the azimuth directions, as shown in [96]. In the following sections we will study the effects of pattern diversity as a function of the mode number and will show the performance gains achievable with different modes in different channel models.

We assume the angles of arrival/departure are distributed only over the azimuth directions (i.e., $\theta = \pi/2$). Over these directions, the far-field of the circular patch antenna is only vertically polarized and the ϕ component of the far-field in (3.3) is zero. From equation (3.2) we derive the array response of the CPA as

$$\mathbf{a}_{\text{cpa}}(\phi) = \alpha(\rho, n)\left[\cos(n\phi),\ \ \sin(n\phi)\right]^T \tag{3.5}$$

where $\alpha(\rho, n) = e^{jn\pi/2}(V_0^{(n)}/2)k_0\rho\left[J_{n+1}(k_0\rho) - J_{n-1}(k_0\rho)\right]$ and ϕ is the azimuth angle of arrival/departure. In our analysis we fix the overall power radiated by the array to be a constant for any mode and we assume $||\mathbf{a}_{\text{cpa}}(\phi)||_2^2 = |\alpha(\rho, n)|^2 = N = 2$ for any azimuth direction (ϕ). In practice, it is possible to design the CPA such that the condition of constant "radiated" power ($|\alpha(\rho, n)|^2$) is equivalent to constant "input" power ($|V_0^{(n)}|^2$) across different modes. In particular, we consider the radius in (3.4) for which the circular patch antenna resonates and compute
$\alpha(\rho = \bar{\rho}, n) = (V_0^{(n)}/2)(\chi'_n/\sqrt{\epsilon_r})\left[J_{n+1}(\chi'_n/\sqrt{\epsilon_r}) - J_{n-1}(\chi'_n/\sqrt{\epsilon_r})\right]$. Then, it can be numerically verified that for the most common values of $\epsilon_r \in [2, 6]$,

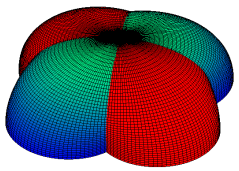

(a) $n = 1$

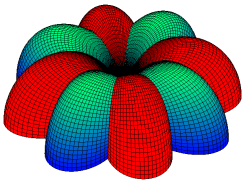

(b) $n = 2$

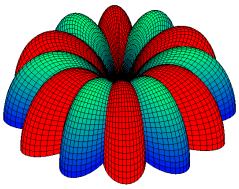

(c) $n = 3$

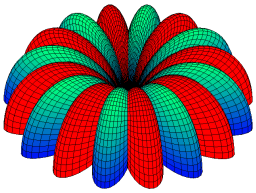

(d) $n = 4$

Figure 3.2: Radiation patterns of circular patch antennas excited with different modes. In each subplot, different colors correspond to the radiation patterns of the 2 antennas of the CPA.

different dielectric constants can be chosen for different values of n, such that $V_0^{(n)}$ is almost constant across different modes. This equivalence between input and radiated power enables a fair performance comparison across different modes for a fixed input power constraint. Note that the analyses presented in the next sections do not account for possible difference in return loss across different modes, which may manifest in practical designs.

3.2 Spatial Correlation in Single-Cluster Channels

In this section, we derive exact and approximate spatial correlation coefficients for CPAs and ULAs, respectively, assuming the MIMO clustered channel model described in the previous section.

3.2.1 Spatial Correlation of the CPA

We model the voltage received at the port of the ℓ-th patch as [100]

$$v_\ell = \int_{4\pi} \underline{e}_\ell(\Omega) \cdot \underline{E}_\ell(\Omega) d\Omega \tag{3.6}$$

where $\Omega = (\phi, \theta)$ is the solid angle, $\underline{E}_\ell(\Omega) = E_{\ell,\theta}\widehat{\theta} + E_{\ell,\phi}\widehat{\phi}$ is the far-field of the circular patch with θ and ϕ components given in equations (3.2) and (3.3), $\underline{e}_\ell(\Omega)$ is the propagating field that impinges the antenna from the angular direction Ω.

From equation (3.6) we derive the correlation coefficient across the ℓ-th and m-th antenna of the MIMO array by computing

$$r_{\ell,m} = \mathcal{E}\{v_\ell v_m^*\} = \int_{4\pi} S(\Omega)\underline{E}_\ell(\Omega)\underline{E}_m^*(\Omega) d\Omega \tag{3.7}$$

where $S(\Omega) = \mathcal{E}\{\underline{e}_\ell(\Omega)\underline{e}^*_m(\Omega)\}$ is the power angular spectrum (PAS) described in Section 2.2. Comparing (3.7) with (2.14), we observe that in (3.7) the phase term is removed since we assume the circular patch antennas are collocated.

We now consider two circular patch antennas, both excited with the n-th mode. We assume the first antenna to be oriented with feed angle $\phi_0^{(1)} = 0$. The second antenna has feed angle $\phi_0^{(2)} = \pi/(2n)$ to produce a radiation pattern orthogonal to the first one. Under these assumptions, substituting equations (3.2) and (3.3) into (3.7), and accounting for the assumptions on the PAS, the autocorrelation coefficient for the first antenna is

$$\begin{aligned} r_{11} \; &= \left|\frac{V_0}{2}k_0\rho\right|^2 \int_{-\pi}^{\pi}\int_{0}^{\pi} P_\phi(\phi) * \delta(\phi-\phi_c)\delta(\theta-\pi/2) \\ &\quad \cdot \left[\cos^2(n\phi)\left[J_{n+1}-J_{n-1}\right]^2 + \cos^2\theta\sin^2(n\phi)\left[J_{n+1}+J_{n-1}\right]^2\right]\sin\theta \; d\theta d\phi. \end{aligned} \tag{3.8}$$

Solving the integral in θ we get

$$r_{11} = \left|\frac{V_0}{2}k_0\rho\right|^2 \left[J_{n+1}(k_0\rho) - J_{n-1}(k_0\rho)\right]^2 \int_{-\pi}^{\pi} P_\phi(\phi)\cos^2\left[n(\phi-\phi_c)\right] d\phi. \tag{3.9}$$

Using the definition in (2.1), the integral in (3.9) can be expanded as

$$\begin{aligned} \int_{-\pi}^{\pi} P_\phi(\phi)\cos^2\left[n(\phi-\phi_c)\right] d\phi \; &= \frac{1}{\sqrt{2}\sigma_\phi}\left[\cos^2(n\phi_c)\int_{-\pi}^{\pi} e^{-|\sqrt{2}\phi/\sigma_\phi|}\cos^2(n\phi)d\phi\right. \\ &\quad \left. + \sin^2(n\phi_c)\int_{-\pi}^{\pi} e^{-|\sqrt{2}\phi/\sigma_\phi|}\sin^2(n\phi)d\phi\right]. \end{aligned} \tag{3.10}$$

To evaluate the integrals in (3.10) we use the properties in [101](eq. 1.5.49.12 on p. 234). Then, we derive the closed-form expression of the auto-correlation

coefficient as a function of the channel parameters ϕ_c and σ_ϕ as

$$\begin{aligned} r_{11}(\phi_c, \sigma_\phi) &= \frac{|\alpha(\rho, n)|^2}{\left(1 - e^{-\sqrt{2}\pi/\sigma_\phi}\right)} \frac{(n\sigma_\phi)^2}{1 + 2(n\sigma_\phi)^2} \\ &\quad \times \left[1 - e^{-\sqrt{2}\pi/\sigma_\phi} + \frac{\cos^2(n\phi_c)}{(n\sigma_\phi)^2} \left(1 - e^{-\sqrt{2}\pi/\sigma_\phi} \cos(n\pi)\right)\right] \end{aligned} \tag{3.11}$$

where $\alpha(\rho, n)$ is defined as in equation (3.5). This correlation coefficient is derived for the single-cluster channel, but its expression can be easily extended to multiple clusters by adding up the correlation coefficients due to each of the clusters, thanks to the independence of clusters. The auto-correlation coefficient for the second patch antenna is derived from equation (3.11). Accounting for the angle shift ($\phi_0^{(2)} = \pi/(2n)$) across the two antennas (i.e., $r_{22}(\phi_c, \sigma_\phi) = r_{11}(\phi_c - \phi_0^{(2)}, \sigma_\phi)$), we find

$$\begin{aligned} r_{22}(\phi_c, \sigma_\phi) &= \frac{|\alpha(\rho, n)|^2}{\left(1 - e^{-\sqrt{2}\pi/\sigma_\phi}\right)} \frac{(n\sigma_\phi)^2}{1 + 2(n\sigma_\phi)^2} \\ &\quad \times \left[1 - e^{-\sqrt{2}\pi/\sigma_\phi} + \frac{\sin^2(n\phi_c)}{(n\sigma_\phi)^2} \left(1 - e^{-\sqrt{2}\pi/\sigma_\phi} \cos(n\pi)\right)\right]. \end{aligned} \tag{3.12}$$

To derive the cross-correlation coefficients we follow similar steps as before, resulting in

$$r_{12} = \frac{\left|\frac{V_0}{2} k_0 \rho\right|^2}{2} \left[J_{n+1}(k_0\rho) - J_{n-1}(k_0\rho)\right]^2 \int_{-\pi}^{\pi} P_\phi(\phi) \sin\left[2n(\phi - \phi_c)\right] d\phi. \tag{3.13}$$

Using the definition of PAS in Section 2.2, we expand the integral in (3.13) as

$$\begin{aligned} \int_{-\pi}^{\pi} P_\phi(\phi) \sin\left[2n(\phi - \phi_c)\right] d\phi &= -\frac{1}{\sqrt{2}\sigma_\phi \left(1 - e^{-\sqrt{2}\pi/\sigma_\phi}\right)} \sin(2n\phi_c) \\ &\quad \times \int_{-\pi}^{\pi} e^{-|\sqrt{2}\phi/\sigma_\phi|} \cos(2n\phi) d\phi. \end{aligned} \tag{3.14}$$

We evaluate the integral in (3.14) by using the property in [101](eq. 1.5.49.11 on p. 234). Substituting (3.14) in (3.13) we find

$$r_{12}(\phi_c, \sigma_\phi) = \frac{|\alpha(\rho, n)|^2}{2} \frac{\sin(2n\phi_c)}{1 + 2(n\sigma_\phi)^2} \tag{3.15}$$

where $\alpha(\rho, n)$ is defined as before. Note that the cross-correlation coefficient r_{21} has the same expression as equation (3.15).

In Fig. 3.3 we show the correlation coefficients of the CPA when modes 1, 3, and 5 are excited inside the microstrip antennas. It is possible to see that, as the mode number (n) increases, the frequency of the oscillations of the auto-correlation (r_{11} and r_{22}, around the value 1) and the cross-correlation (r_{12}, around 0) increases. This is due to the higher number of lobes in the radiation patterns for the higher order modes, as shown in Fig. 4.7. The amplitude of these oscillations decreases for increasing n, which makes the spatial correlation matrix closer to identity. We will find in the next section that this behavior results in increased capacity for the higher order modes.

3.2.2 Spatial Correlation of the ULA

We express the phase term in (2.14) of the m-th array element with respect to the reference antenna as a function of the AOA as

$$\Phi_m(\phi) = kdm \sin(\phi_c - \phi) \tag{3.16}$$

where $m = 0, ..., M-1$, ϕ is the AOA offset with respect to the mean AOA of the cluster ϕ_c (measured from the broadside direction of the ULA), d is

the antenna element spacing and k is the wavenumber. Substituting (3.16) in (2.14), we express the cross-correlation coefficient of the ULA as

$$r_{m,n} = \int_{-\pi}^{\pi} \mathrm{e}^{jkd(m-n)\sin(\phi_c-\phi)}\, P_\phi(\phi)\, d\phi \tag{3.17}$$

where $P_\phi(\phi)$ is the pdf given in (2.1).

Let us express the exponent of the function inside the integral as

$$\sin(\phi_c - \phi) = \sin\phi_c \cos\phi - \cos\phi_c \sin\phi. \tag{3.18}$$

Expanding with a first-order Taylor series (assuming $\phi \approx 0$)

$$\sin(\phi_c - \phi) \approx \sin\phi_c - \phi\cos\phi_c. \tag{3.19}$$

Substituting (3.19) into (3.17) we get

$$r_{m,n} \approx \mathrm{e}^{jkd(m-n)\sin\phi_c} \cdot \int_{-\pi}^{\pi} \mathrm{e}^{-jkd(m-n)\cos(\phi_c)\phi}\, P_\phi(\phi)\, d\phi. \tag{3.20}$$

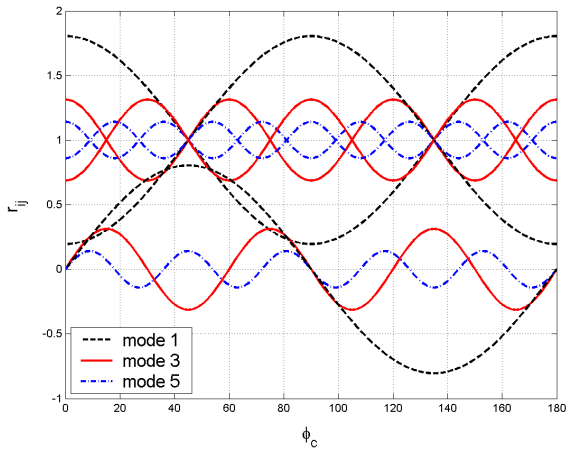

Figure 3.3: Correlation coefficients for the CPA, with modes 1, 3, 5, and $\sigma_\phi = 20^o$.

From (2.1) we observe that the truncated Laplacian PAS is zero outside the range $[-\pi, \pi)$. Therefore, the integration of $P_\phi(\phi)$ truncated over $[-\pi, \pi)$ is approximately equivalent to integration over the real line. Then, substituting (2.1) into (3.20) we get

$$r_{m,n}(\phi_{\rm c}, \sigma_\phi) \approx {\rm e}^{jkd(m-n)\sin\phi_{\rm c}} \cdot \int_{-\infty}^{\infty} e^{-jkd(m-n)\cos(\phi_{\rm c})\phi} \; \frac{\beta}{\sqrt{2}\sigma_\phi} {\rm e}^{-|\sqrt{2}\phi/\sigma_\phi|} \; d\phi. \quad (3.21)$$

Equation (3.21) consists of the product of a complex exponential term times an integral term. The integral term is the characteristic function of the Laplacian pdf in (2.1), and it can be expressed as

$$b_{m,n}(\phi_{\rm c}, \sigma_\phi) = \int_{-\infty}^{\infty} e^{-jkd(m-n)\cos(\phi_{\rm c})\phi} \; \frac{\beta}{\sqrt{2}\sigma_\phi} {\rm e}^{-|\sqrt{2}\phi/\sigma_\phi|} \; d\phi = \mathcal{F}_\omega \left\{ \frac{\beta}{\sqrt{2}\sigma_\phi} {\rm e}^{-|\sqrt{2}\phi/\sigma_\phi|} \right\} \quad (3.22)$$

where $\mathcal{F}_\omega$ denotes the Fourier transform evaluated at $\omega = kd(m-n)\cos\phi_{\rm c}$. Solving (3.22), we get

$$r_{m,n}(\phi_{\rm c}, \sigma_\phi) = \frac{\beta}{1 + \frac{\sigma_\phi^2}{2} \cdot [kd(m-n)\cos\phi_{\rm c}]^2} \quad (3.23)$$

with $m, n = 0, ..., (M-1)$. Therefore, substituting (3.23) in (3.21) we derive the following closed-form for the correlation coefficients across all the array elements

$$r_{m,n}(\phi_{\rm c}, \sigma_\phi) \approx \frac{\beta \; {\rm e}^{jkd(m-n)\sin\phi_{\rm c}}}{1 + \frac{\sigma_\phi^2}{2} \cdot [kd(m-n)\cos\phi_{\rm c}]^2}. \quad (3.24)$$

The complex exponential term in (3.21) can be written as

$${\rm e}^{jkd(m-n)\sin\phi_{\rm c}} = {\rm e}^{jkdm\sin\phi_{\rm c}} \cdot {\rm e}^{-jkdn\sin\phi_{\rm c}} \quad (3.25)$$

where the multiplicative factors at the right hand side of (3.25) are the entries of the steering vector of the ULA, given by

$$\mathbf{a}_{\text{ula}}(\phi_{\text{c}}) = \left[1,\ \mathrm{e}^{jkd\sin\phi_{\text{c}}},\quad \cdots\quad ,\mathrm{e}^{jkd(M-1)\sin\phi_{\text{c}}}\right]^T. \tag{3.26}$$

Using the definition in (3.26), we derive the spatial correlation matrix, with complex entries given by (3.24), as

$$\mathbf{R}(\phi_{\text{c}},\sigma_\phi) \approx \left[\mathbf{a}_{\text{ula}}(\phi_{\text{c}})\cdot\mathbf{a}^{\dagger}_{\text{ula}}(\phi_{\text{c}})\right]\odot\mathbf{B}_{\text{ula}}(\phi_{\text{c}},\sigma_\phi) \tag{3.27}$$

where $\odot$ denotes the Shur-Hadamard (or elementwise) product, $\mathbf{a}(\phi_{\text{c}})$ is the array response (column vector) for the mean azimuth AOA (ϕ_{c}) and $\mathbf{B}_{\text{ula}}$ is the matrix with entries $b_{m,n}$. A similar result was given in [102, 103], where the Gaussian distribution was used for the PAS. In our case, however, we computed the matrix $\mathbf{R}(\phi_{\text{c}},\sigma_\phi)$ for the case of Laplacian pdf, given by (2.1).

3.3 Analysis of Pattern and Space Diversity

In this section we analytically derive some tradeoffs between pattern and space diversity, employing the CPA and ULA described above. First we show that capacity and error rate performance are a function of the eigenvalues of the spatial correlation matrix. Then we use the correlation coefficients derived in (3.11), (3.12) and (3.15) to compute the eigenvalues of $\mathbf{R}$ in closed-form as a function of array and channel parameters for the CPA and the ULA. Comparing the eigenvalues for the CPA and the ULA, we provide a formula to predict when pattern diversity is more effective than space diversity, as a

function of the array and channel parameters. We will show that the gain due to pattern diversity is a function of the mode number (n) of the microstrip antennas, whereas the gain of space diversity depends on the element spacing (d) of the ULA.

3.3.1 Capacity and Error Rate Performance

We consider the tight upper bound to the ergodic capacity for spatial multiplexing (SM) systems (with equal power allocation across the transmit antennas) reported in [104]. We assume zero-mean single-sided (only at the transmitter) correlated MIMO channels. This upper bound is expressed as

$$C \leq \log_2 \left[\sum_{k=0}^{N_{\min}} \left(\frac{\gamma_o}{N_t} \right)^k \frac{N_r!}{(N_r - k)!} \sum_{\nu_k} |\mathbf{R}_{\nu_k}^{\nu_k}| \right] \tag{3.28}$$

where $N_{\min} = \min(N_r, N_t)$, ν_k is an ordered subset of $\{1, ..., N_{\min}\}$ with measure $|\nu_k| = k$ and $\mathbf{R}_{\nu_k}^{\nu_k}$ denotes the $k \times k$ sub-matrix lying in the ν_k rows and ν_k columns of the transmit spatial correlation matrix $\mathbf{R}$.

For the case of $N_t = N_r = N = 2$, we get $|\mathbf{R}_{\nu_0}^{\nu_0}| = 1$, $|\mathbf{R}_{\nu_1}^{\nu_1}| = N = 2$ and $|\mathbf{R}_{\nu_2}^{\nu_2}| = |\mathbf{R}| = \lambda_1 \lambda_2$. Then, we may express the upper bound in (3.28) as

$$C \leq \log_2 \left[1 + 2\ \gamma_o + \frac{\gamma_o^2}{2} \lambda_1 \lambda_2 \right] \tag{3.29}$$

where λ_1 and λ_2 are the eigenvalues of the spatial correlation matrix $\mathbf{R}$. Equation (3.29) shows that the capacity increases as a function of the product of the eigenvalues ($\lambda_1 \lambda_2$).

We derive the error rate performance as a function of the eigenvalues of $\mathbf{R}$ as well. The error rate performance depends on the type of space-time

codes (e.g., spatial multiplexing or space-time block codes or space-time trellis codes). As we consider $N = 2$, we focus on error rate estimate for the Alamouti scheme [35], recognizing that the Alamouti scheme is not capacity achieving as (3.28) [34, p.115]. In the high SNR regime, the average probability of symbol error is upper-bounded by [33, p.102]

$$P_e \leq N_e \left(\frac{\gamma_o \, d_{\min}^2}{8} \right)^{-r} \prod_{i=1}^{r} \frac{1}{\lambda_i} \tag{3.30}$$

where r and λ_i are the rank and eigenvalues of $\mathbf{R}$, respectively, while N_e and $d_{\min}$ are the number of nearest neighbors and minimum distance of the symbol constellation, respectively. For the case of $N_t = N_r = N = 2$ and full rank $\mathbf{R}$, we simplify the expression in (3.30) as

$$P_e \leq N_e \left(\frac{8}{\gamma_o \, d_{\min}^2} \right)^{2} \frac{1}{\lambda_1 \lambda_2}. \tag{3.31}$$

The error rate performance improves as the product $\lambda_1 \lambda_2$ increases.

In equations (3.29) and (3.31) we found that the capacity and error rate performance of a 2×2 MIMO system is a function of the product $\lambda_1 \lambda_2$. We will use this product as a measure of system performance. In the next subsections we will derive the eigenvalues of $\mathbf{R}$ in closed-form as a function of the channel and antenna parameters for the CPA and ULA. Then, we will use these expressions to derive some tradeoffs between pattern and space diversity.

3.3.2 Eigenvalues of the Spatial Correlation Matrix for the CPA

The eigenvalues ($\lambda_{1,2}$) of the 2×2 spatial correlation matrix ($\mathbf{R}$) can be expressed as

$$\lambda_{1,2} = \frac{1}{2}\left[(r_{11} + r_{22}) \pm \sqrt{4r_{12}r_{21} + (r_{11} - r_{22})^2}\right]. \tag{3.32}$$

Substituting equations (3.11), (3.12), and (3.15) into (4.5) and simplifying, we derive the eigenvalues of the correlation matrix for the CPA as

$$\begin{aligned}\lambda_{1,2}^{\text{cpa}} &= \frac{|\alpha(\rho,n)|^2}{2}\frac{1}{1+2(n\sigma_\phi)^2}\cdot\left\{\left[2(n\sigma_\phi)^2 + \frac{1-e^{-\sqrt{2}\pi/\sigma_\phi}\cos(n\pi)}{1-e^{-\sqrt{2}\pi/\sigma_\phi}}\right]\right. \\ &\left. \pm\sqrt{\sin^2(2n\phi_c) + \left(\frac{1-e^{-\sqrt{2}\pi/\sigma_\phi}\cos(n\pi)}{1-e^{-\sqrt{2}\pi/\sigma_\phi}}\right)^2\cos^2(2n\phi_c)}\right\}.\end{aligned} \tag{3.33}$$

We note that for n integer, the term $\cos(n\pi)$ assumes values $+1$ or -1 depending on whether n is even or odd. When n is *even* the expression (3.33) simplifies to

$$\lambda_{1,2}^{\text{cpa}} = \frac{|\alpha(\rho,n)|^2}{2}\left[1 \pm \frac{1}{1+2(n\sigma_\phi)^2}\right]. \tag{3.34}$$

Recall that $|\alpha(\rho,n)|^2 = N = 2$ (i.e., trace($\mathbf{R}$) $= N$) as specified for equation (3.5). Then, we get the following closed-form expression of the eigenvalues of $\mathbf{R}$ as a function of the channel and antenna parameters

$$\lambda_{1,2}^{\text{cpa}} = 1 \pm \frac{1}{1+2(n\sigma_\phi)^2}. \tag{3.35}$$

Note that these eigenvalues depend only on the cluster angular spread, but not on the mean angle of arrival of the cluster, due to the symmetry of the orthogonal radiation patterns of the two elements of the CPA.

When n is *odd*, equation (3.33) becomes

$$\lambda_{1,2}^{\text{cpa}} = \frac{1}{1+2(n\sigma_\phi)^2} \cdot \left\{ \left[2(n\sigma_\phi)^2 + \frac{1+e^{-\sqrt{2}\pi/\sigma_\phi}}{1-e^{-\sqrt{2}\pi/\sigma_\phi}} \right] \pm \sqrt{\sin^2(2n\phi_c) + \left(\frac{1+e^{-\sqrt{2}\pi/\sigma_\phi}}{1-e^{-\sqrt{2}\pi/\sigma_\phi}} \right)^2 \cos^2(2n\phi_c)} \right\} \tag{3.36}$$

where we applied the usual power normalization $|\alpha(\rho, n)|^2 = N = 2$. In this case the eigenvalues of $\mathbf{R}$ are a function of the cluster mean angle of arrival/departure (ϕ_c). However, the ratio within the square-root is close to 1, especially for high values of σ_ϕ, which makes the term under the square-root almost constant (i.e., independent on ϕ_c) and equal to 1. Therefore, the oscillations of the eigenvalues as a function of ϕ_c are small around their mean value as shown in Fig. 3.4, where we plotted also the envelope correlation coefficients as reference. For high angle spread (σ_ϕ) and n odd, we can write

$$\lambda_{1,2}^{\text{cpa}} \approx 1 \pm \frac{1}{1+2(n\sigma_\phi)^2}. \tag{3.37}$$

Computing the limit of (3.35) and (3.36) for $n \to \infty$ we find that

$$\lim_{n\to\infty} \lambda_{1,2}^{\text{cpa}} = 1. \tag{3.38}$$

As the mode number increases, the eigenvalues become closer to 1 and the product $\lambda_1\lambda_2$ is maximized. This maximization is due to the higher decorrelation between the diversity branches of the CPA for the higher order modes, which results in improved channel capacity and error rate performance, according to (3.29) and (3.31). This result can be physically explained as follows:

for high n the radiation pattern of the circular patch antenna is characterized by a large number of lobes, which yields high *pattern diversity*.

3.3.3 Eigenvalues of the Spatial Correlation Matrix for the ULA

We use the approximate expression of the correlation coefficients for ULAs with Laplacian distributed power azimuth spectrum, derived in [105]

$$r_{\ell,m} \approx \frac{e^{jk_0 d(m-\ell)\sin\phi_c}}{1+\frac{\sigma_\phi^2}{2}\cdot\left[k_0 d(m-\ell)\cos\phi_c\right]^2} \tag{3.39}$$

where d is the element spacing of the ULA. Using equation (4.5) and simplifying, we find that

$$\lambda_{1,2}^{\text{ula}} = 1 \pm \frac{1}{1+\frac{\sigma_\phi^2}{2}\left(k_0 d\cos\phi_c\right)^2}. \tag{3.40}$$

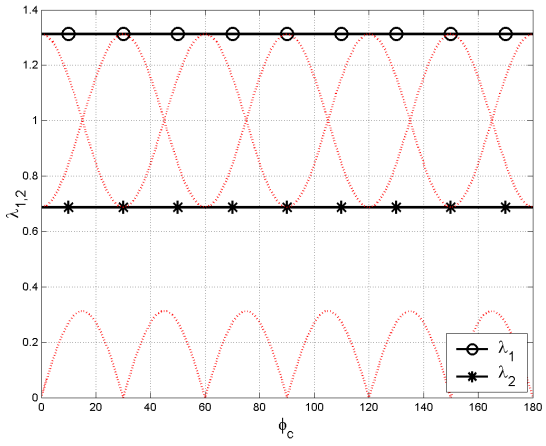

Figure 3.4: Eigenvalues of the correlation matrix for CPA with mode 3 and $\sigma_\phi = 20^o$

We then compute the limit of (3.40) for $d \to \infty$ as

$$\lim_{d\to\infty} \lambda_{1,2}^{\text{ula}} = 1. \tag{3.41}$$

Equation (3.41) reveals a well known result: increasing the element spacing produces high *space diversity*, which yields increased channel capacity [16, 24] and reduced error rate.

3.3.4 Pattern and Space Diversity Tradeoff

In equations (3.29) and (3.31), we showed that the capacity and error rate performance of a 2×2 MIMO system depends on the product of the eigenvalues of $\mathbf{R}$ (i.e., $\lambda_1\lambda_2$). Here we compare the eigenvalues for the CPA and ULA obtained in the previous subsections to derive a condition for which one array performs better than the other. This condition will define the tradeoff between pattern diversity (for the CPA) and space diversity (for the ULA). We assume the product of the eigenvalues for the CPA in (3.35) to be larger that the ULA in (3.40), which is the condition for which the CPA outperforms the ULA, according to (3.29) and (3.31). Then, we write

$$\begin{aligned} \lambda_1^{\text{cpa}}\lambda_2^{\text{cpa}} &= 1 - \left[\frac{1}{1+2(n\sigma_\phi)^2}\right]^2 \\ &> 1 - \left[\frac{1}{1+\frac{\sigma_\phi^2}{2}\left(k_0 d\cos\phi_c\right)^2}\right]^2 = \lambda_1^{\text{ula}}\lambda_2^{\text{ula}}. \end{aligned} \tag{3.42}$$

Solving this inequality we derive

$$\boxed{n > \bar{d}\pi\cos\phi_c} \tag{3.43}$$

where $\bar{d} = d/\lambda$ is the element spacing normalized with respect to the wavelength. Interestingly, the expression (3.43) does not depend on σ_ϕ, which suggest that the pattern/space diversity tradeoff is independent on the angular spread of the channel. Moreover, at endfire directions (i.e., $\phi_c = \pi/2$) the CPA always outperforms the ULA, since the inequality $n > 0$ is always satisfied. At broadside directions (i.e., $\phi_c = 0$) we get

$$n > \bar{d}\pi \tag{3.44}$$

which can be used as rule of thumb to choose an optimal mode number in the design of the CPA. As example, to design a CPA that outperforms a ULA of dipoles half wavelength spaced apart, we would need at least $n = 2$. *This expression also reveals under which conditions pattern diversity is more effective than space diversity.*

To get an insight on the diversity gain achievable with the CPA over the ULA, we compute the SNR gain as a function of the eigenvalues of $\mathbf{R}$. We assume the same predefined target symbol error probability (P_e) and constellation type (characterized by N_e and $d_{\min}$) for transmissions with either the CPA or ULA. Then, from (3.31) we express the SNR gain as

$$G = \frac{\gamma_{\text{o,ula}}}{\gamma_{\text{o,cpa}}} = \sqrt{\frac{\lambda_1^{\text{cpa}}\lambda_2^{\text{cpa}}}{\lambda_1^{\text{ula}}\lambda_2^{\text{ula}}}} \tag{3.45}$$

where the expression of the product of eigenvalues is given by (3.42). We now consider a practical example where the CPA is excited with mode 4 and the ULA has element spacing $d = \lambda/2$. We assume $\sigma_\phi = 20^{\text{o}}$ and $\phi_c \in$

$[0, 60^{o}]$, which is the range of values for which the approximation in (3.39) holds with negligible error, as specified in [105]. Under these assumptions, pattern diversity (with the CPA) yields SNR gains over space diversity (with the ULA) in the range 1-3 dB. We will validate this theoretical result through simulations in the next section.

3.4 Performance Results in Clustered MIMO Channel Models

In this section we present some numerical performance results that compare the CPA and ULA in terms of MIMO channel capacity and symbol error rate (SER). We first show how these arrays perform in single and double cluster channels. Then, we present capacity and error rate performance in typical channel models for indoor environments, consistent with the IEEE 802.11n standard channel model [43]. Finally, we measure the performance degradation of the two arrays due to mutual coupling.

3.4.1 Single-Cluster Channels

Here we simulate the MIMO channel with a single cluster, generated with variable mean angle of arrival/departure (ϕ_c) and fixed angular spread σ_ϕ. In Fig. 4.4 we compare the envelope correlation coefficients of the CPA (with mode 3) against the ULA (with element spacing of $\lambda/2$), for single cluster with $\sigma_\phi = 15^{o}$. We generate the correlation coefficients of the ULA through the exact expression derived in [47] for Laplacian distributed angles of arrival. The

auto-correlation coefficients of the ULA are always one by definition, whereas the cross-correlation varies as a function of ϕ_c. In particular, at the broadside direction (i.e., $\phi_c = 0^o$), r_{12} reaches its lowest value, which results in the spatial correlation matrix to be closer to identity. On the other hand, at the endfire direction (i.e., $\phi_c = 90^o$), r_{12} becomes very close to the auto-correlation coefficients, producing a correlation matrix close to rank one. In the same plot it is depicted the MIMO channel capacity at $\gamma_o = 5$ dB for the two arrays. We compute the ergodic capacity employing the tight upper bound for zero mean single-sided spatially correlated MIMO channels reported in (3.29). The capacity of the CPA has small oscillations around its mean value (which are not visible in Fig. 4.4), due to the slow oscillations of the eigenvalues of $\mathbf{R}$ as reported in equation (3.36). The capacity of the ULA reaches its maximum and

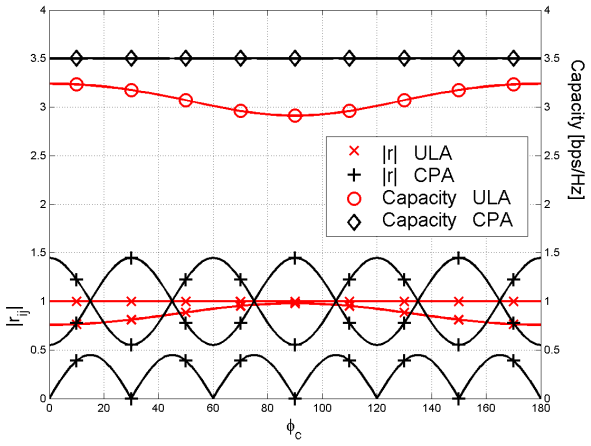

Figure 3.5: Envelope correlation and ergodic capacity for the ULA with element spacing of $\lambda/2$ and CPA with mode 3. The channel is simulated with $\sigma_\phi = 15^o$ and $\gamma_o = 5$dB.

minimum values at broadside and endfire directions, respectively, as already acknowledged in [24]. Interestingly, the CPA outperforms the ULA for any direction of arrival.

In Fig. 3.6 we report the ergodic capacity (i.e., upper bound) at $\gamma_o = 5$ dB for the ULA and the CPA with different modes, in single-cluster channel with $\sigma_\phi = 30^o$. For "mode 1" the CPA outperforms the ULA only for angles close to endfire directions. In fact, the radiation pattern of "mode 1" consists of only two lobes over the azimuth directions (as depicted in Fig. 3.2(a)), which makes pattern diversity less effective than space diversity. For the higher modes, the CPA always provides better performance than the ULA, in agreement with the analytical results presented in (3.44). Moreover, the maximum capacity of the CPA is close to its saturation point when "mode 3" is employed. Note that the higher the mode number the larger the size of the microstrip antenna for fixed dielectric constant of the substrate and carrier frequency, as shown in (3.4). Therefore, "mode 3" is a good tradeoff in terms of antenna size and MIMO performance.

3.4.2 Double-Cluster Channels

We now generate two clusters with variable mean angle of arrival and measure the MIMO capacity for the CPA (with "mode 3") and ULA. The MIMO mean capacity is derived according to the upper bound in (3.29) for zero-mean single-sided correlated MIMO channels.

In Fig. 3.7(a) we report the mean capacity as a function of the two

mean angles of arrival of the clusters (ϕ_1 and ϕ_2). The ULA is simulated with element spacing $d = \lambda/2$. It is possible to see that the CPA outperforms the ULA for any channel scenario (i.e., combination of ϕ_1 and ϕ_2). Then, we compare the performance of the CPA against the ULA with spacing $d = 2.5\lambda$ in Fig. 3.7(b). We notice that only at broadside directions (i.e., ϕ_1,$\phi_2 \approx 0$) the ULA outperforms the CPA. In this case, to improve the performance of the CPA we would need to increase the mode number, as suggested by the inequality (3.44).

3.4.3 IEEE 802.11n Channel Models

Here we compare the performance of the CPA and ULA in typical clustered channels for indoor environments, described in the IEEE 802.11n stan-

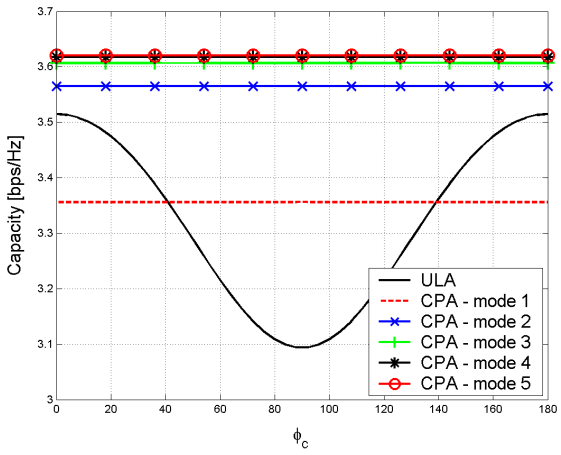

Figure 3.6: Ergodic capacity for the ULA with element spacing of $\lambda/2$ and CPA with different mode numbers. The channel is simulated with $\sigma_\phi = 30^o$ and $\gamma_o = 5$dB.

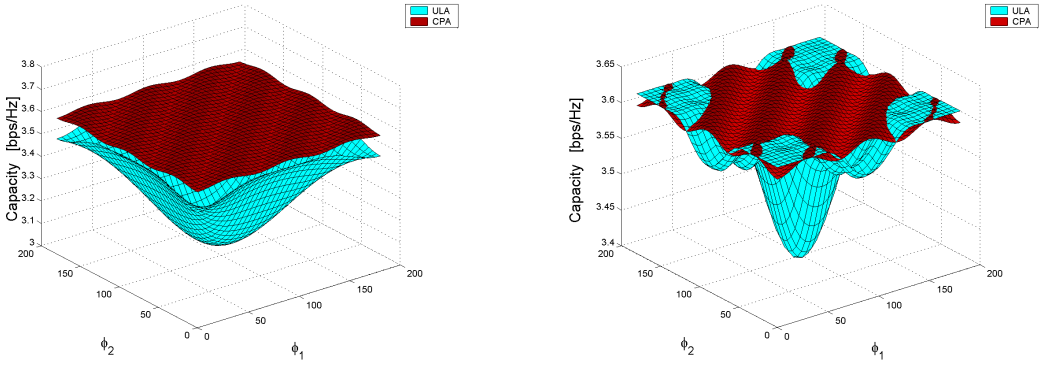

(a) ULA with $d = \lambda/2$

(b) ULA with $d = 2.5\lambda$

Figure 3.7: Ergodic capacity for double-cluster channels as a function of the mean azimuth AoAs (ϕ_1 and ϕ_2) of the clusters, with $\sigma_\phi = 30^o$ and $\gamma_o = 5$dB. The CPA is excited with mode 3.

dard channel model [43]. We assume Ricean double-sided correlated channel as in (2.5) and compute the LOS component in equation (2.6) by using the array response for the CPA and ULA given by (3.5) and (3.26), respectively. We study the performance of these arrays in terms of MIMO channel capacity and symbol error rate (SER), through Monte Carlo simulations. To derive the SER curves we simulate a 2×2 narrowband MIMO system, according to equation (3.1). We employ QPSK modulation, Alamouti scheme at the transmitter [35] and maximum ratio combining (MRC) receiver. We compare the performance of three different arrays: CPA with mode 3, ULA1 with element spacing $d = \lambda/2$ and ULA2 with element spacing $d = 2.5\lambda$.

In Fig. 3.8 we show the mean channel capacity and SER simulated in

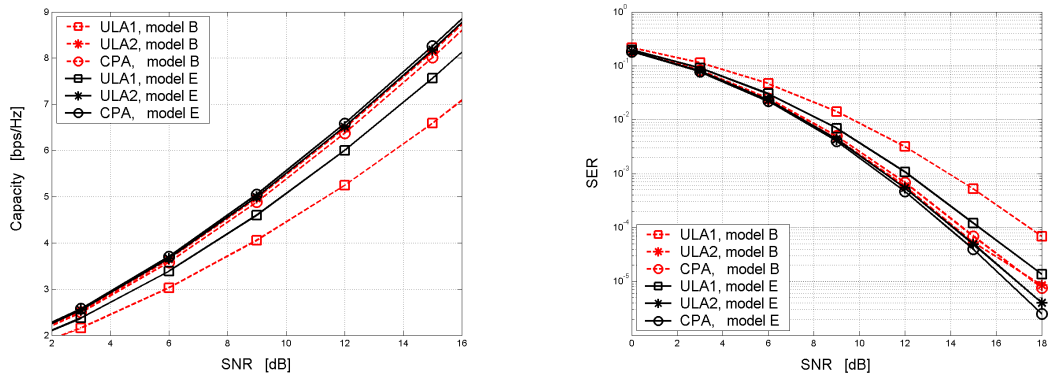

(a) Ergodic capacity

(b) Symbol error rate

Figure 3.8: Ergodic capacity and error rate performance for the CPA with mode 3, ULA1 with $d = \lambda/2$ and ULA2 with $d = 2.5\lambda$, in the IEEE 802.11n standard channel models B and E (NLOS).

the NLOS channel models B and E, described in [43]. It is possible to see that in high SNR regime the CPA yields about 3 dB and 1 dB gain over the ULA1, in channel models B and E, respectively. Note that these gains match the ones theoretically derived in Section 3.3.4, for single-cluster channels. Moreover, the CPA performs similarly to the ULA2, providing more or less gain depending on the channel model.

In Fig. 3.9 we show similar results as in Fig. 3.8, for the case of LOS channel models D and E. Based on the SER results, the CPA provides SNR gains of ~ 2 dB (in high SNR regime) over the ULA1 in channel models D and E. Then, in the LOS case the SNR gains of the CPA over the ULA1 is reduced compared to the NLOS case. Also, the CPA performs similarly to the ULA2,

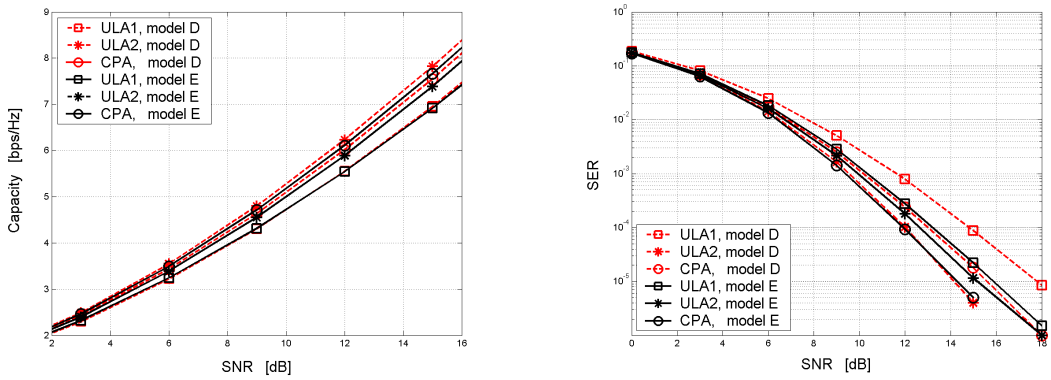

(a) Ergodic capacity

(b) Symbol error rate

Figure 3.9: Ergodic capacity and error rate performance for the CPA with mode 3, ULA1 with $d = \lambda/2$ and ULA2 with $d = 2.5\lambda$, in the IEEE 802.11n standard channel models D and E (LOS).

as for the NLOS case. Note that these results do not account for mutual coupling effects, which may affect the performance of the arrays especially for small element spacing (i.e., $d = \lambda/2$). In the next subsection we show how the performance of these arrays vary due to mutual coupling.

3.4.4 Performance Results with Mutual Coupling Effects

Fig. 3.10 depicts the average MIMO channel capacity (with correlation only at the receive side), accounting for mutual coupling, as a function of the SNR. We measured the effects of mutual coupling for the ULA and CPA through FEKO, an EM software tool based on the method of moments. Then, we used the model for mutually-coupled antennas described in [106, 107] to

estimate the MIMO capacity through Monte Carlo simulations. We designed the antennas to operate at the carrier frequency of 2.45 GHz, which is the operating frequency of WLANs. For the CPA we excited the mode 3 with $\epsilon_r = 2.5$, physical radius $\tilde{\rho} = 0.41\lambda$, feed point $\rho_0 = 0.8\rho$, height of the patch $h = 1.575$ mm.

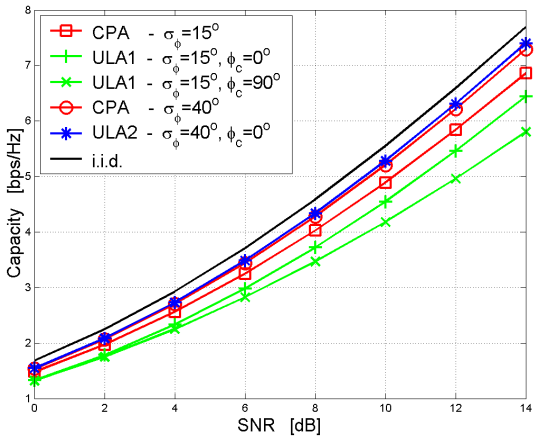

Figure 3.10: Ergodic capacity with mutual coupling effects in different channel scenarios, for the CPA with mode 3 and $\tilde{\rho} = 0.41\lambda$, ULA1 with $d = \lambda/2$ and ULA2 with $d = 2.5\lambda$.

The first set of curves is referred to the ULA with element spacing $\lambda/2$ (i.e., ULA1) and low angle spread (i.e., $\sigma_\phi = 15^o$). In this channel condition, the CPA yields 0.8 dB and 1.8 dB gains at $\gamma_o = 10$ dB over the ULA at broadside and endfire directions, respectively. Therefore, in this conditions, pattern diversity yields higher performance than space diversity, as expected. The second set of curves is obtained for the ULA with element spacing 2.5λ (i.e., ULA2), high angle spread (i.e., $\sigma_\phi = 40^o$) and cluster located at broadside

direction of the ULA2. The MIMO capacity of the CPA is very close to the ULA2, while satisfying more limited size constraints. These results clearly show the benefit of pattern diversity versus space diversity with 2-element ULA and CPA, in single-cluster MIMO channels.

Chapter 4

Design of MIMO Arrays in Clustered Channels

Antenna design for MIMO communication systems requires higher degree of effort compared to conventional single antenna systems. The performance of MIMO arrays is evaluated through metrics that account for the higher complexity of the multivariate channel statistics. This chapter reviews recent advances in the design of MIMO arrays, defining techniques and metrics commonly used for these designs. The objective of this chapter is to propose a new array design methodology that jointly optimizes multiple performance metrics. The proposed design methodology employs antenna theory and communication theoretic performance metrics, and is arguably a cross-layer design problem.

4.1 Introduction

Motivated by the results in Chapter 3, we now define a novel optimization algorithm for CPA designs, accounting for both far-field (i.e., scattering in the propagation environment) and near-field (i.e., mutual coupling) effects. Complete models to analyze the performance of compact MIMO arrays were

proposed in [106, 107]. In [106, 107] the transfer function of MIMO systems (relating the input signals to the output of the receiver) was defined to model the propagation channel as well as the coupled transmit and receive antennas. While these models can be used to evaluate exhaustively the performance of given MIMO array designs, they may not be suitable to optimize the array parameters in different propagation conditions, due to high computational complexity. In this chapter we propose a practical optimization algorithm to design MIMO arrays, by treating the far- and near-field effects separately. We define the objective function of the optimization method based on MIMO communication performance metrics (to account for the propagation channel) and microwave theory performance metrics (determining the antenna efficiency and the effect of mutual coupling).

In Chapter 3 we studied the theoretical capacity and error rate for CPA designs in clustered MIMO channel models, showing that performance gains due to pattern diversity are essentially determined by the shape of the antenna radiation patterns. While in Chapter 3 we employed ideal radiation patterns derived from theoretical analysis, here we evaluate numerically these patterns through electromagnetic (EM) software tools, to account for the near-field effects. We first present channel and antenna parameters used as inputs to the optimization algorithm for CPA designs. We also derive a lower bound on the ergodic capacity in clustered MIMO channels, demonstrating that the CPA performance can be measured over a reduced set of channel parameters with minimal error. This result yields significant computational complexity

reduction for the proposed optimization algorithm. Then we present a new definition of spatial correlation coefficient suitable for studies on pattern diversity in realistic clustered channel models. From the correlation coefficients we derive numerically the MIMO ergodic capacity in correlated channels and define two communication theoretic metrics, that measure average and outage performance of CPAs in different propagation conditions. We evaluate these metrics as a function of the antenna parameters.

Additionally, we evaluate the near-field effects of CPAs by defining the antenna bandwidth from the scattering parameters [108]. Theoretical analysis on the impedance bandwidth of circular microstrip antennas as a function of the physical antenna parameters were presented in [96, 109]. Here, we exploit the results in [96,109] to evaluate bandwidth and mutual coupling effects as a function of the antenna parameters (i.e., radius of the circular patch, feed position). Finally, we propose an optimization algorithm that maximizes the objective function derived from communication theoretic and microwave theory performance metrics to produce optimal CPA designs. To make our discussion concrete, we consider practical system parameters (i.e., frequency band) and clustered channel models as in the IEEE 802.11n standard for wireless local area networks (WLANs). The proposed optimization methodology is conceived for CPA designs, but can be extended to any MIMO array design exploiting pattern diversity.

4.2 Optimization Parameters and Problem Formulation

In this section we describe the channel and antenna parameters used by the proposed optimization algorithm for CPAs. Then we present the problem formulation and algorithm block-diagram.

4.2.1 Channel and Antenna Parameters

There are essentially three *channel parameters* that characterize clustered MIMO channel models:

- **Number of clusters** (N_c);
- **Mean AOA** of the clusters: $\mathbf{\Phi} = [\phi_c^{(1)}, \ldots, \phi_c^{(N_c)}]$, with $\phi_c^{(i)} \in \mathcal{A}_\phi$;
- **Angle spread** of the clusters: $\mathbf{\Sigma} = [\sigma_\phi^{(1)}, \ldots, \sigma_\phi^{(N_c)}]$, with $\sigma_\phi^{(i)} \in \mathcal{A}_\sigma$

where $\mathcal{A}_\phi$ and $\mathcal{A}_\sigma$ denote the set of values of $\phi_c^{(i)}$ and $\sigma_\phi^{(i)}$, respectively. For example, the IEEE 802.11n channel model [43] assumes $\mathcal{A}_\phi = \{0^o, \ldots, 360^o\}$ and $\mathcal{A}_\sigma = \{15^o, \ldots, 50^o\}$.

Our CPA design consists of two circular microstrip antennas stacked one on top of the other as in Fig. 4.1. Each microstrip antenna consists of circular ground plane, substrate and patch, and is excited via coaxial feed. The two microstrip antennas are designed with different radia and dielectric constant of the substrate to excite the same mode number 3. The theoretical relationship between radius and dielectric constant for different mode numbers was shown in Fig. 3.1.

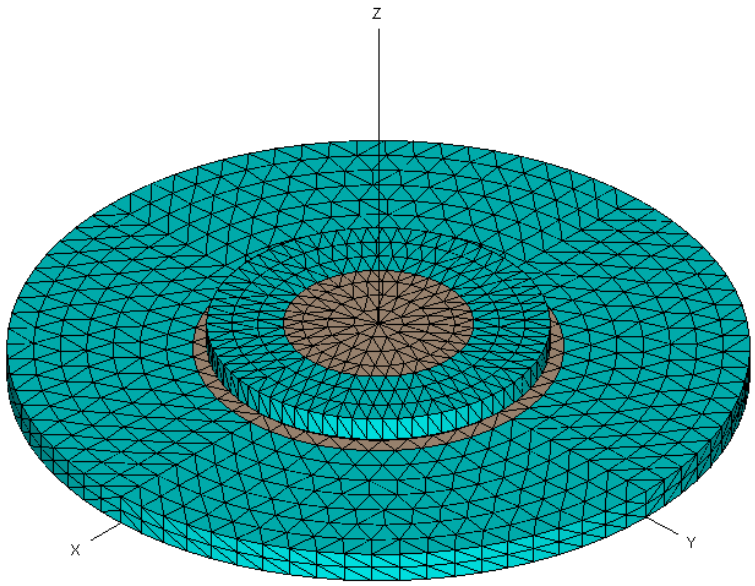

Figure 4.1: Geometry of the 2-CPA design.

The *antenna parameters* describing the physical characteristics of the two elements of the CPA are:

- **Physical radius** (ρ_o) of the circular microstrip antennas;
- **Feed radial position** (ρ_f): defined as the distance between the center of the circular patch antenna and the feeding point (assuming coaxial feed);
- **Height** (h) of the antenna substrate;
- **Dielectric constant** (ϵ_r) of the antenna substrate

where ρ_{f} is defined in the range $[0, \rho_{\mathrm{o}}]$ and typically $\epsilon_r \in [2.2, 12]$.

4.2.2 Problem Statement

The goal of the algorithm proposed in this chapter is to numerically compute the values of antenna parameters that optimize the CPA performance (according to metrics defined later in this chapter) in a variety of propagation scenarios, characterized by different combinations of channel parameters.

The optimization parameters are defined by the following vector describing the physical characteristics of each antenna element of the CPA

$$\mathbf{x}_m = \left[\rho_{\mathrm{o}}^{(m)}, \rho_{\mathrm{f}}^{(m)}, h^{(m)}, \epsilon_r^{(m)}\right] \tag{4.1}$$

where $m \in \{1, 2\}$ for 2-element arrays[1] and $\mathbf{x} = [\mathbf{x}_1, \mathbf{x}_2]$ contains the physical parameters of the 2-CPA. The vector $\mathbf{x}$ takes its values from the set $\mathcal{X} \subset \mathbb{R}^8$ that defines the physical constraints of the array design and the *feasible set* for the optimization algorithm. Note that $\mathbf{x}$ may also contain additional entries, such as the radius of the circular ground plane (ρ_{gp}) and the coaxial feed pin (r_{c}).

Fig. 4.2 depicts the block diagram of the proposed optimization algorithm for MIMO array designs. For given input $\mathbf{x}$, the antenna patterns are computed numerically through EM software tools and used in combination with the channel parameters to predict the performance of MIMO arrays in

[1]For the rest of this chapter, we denote the bottom patch in Fig. 4.1 with "1" and the top patch with "2".

correlated channels. Different communication theoretic metrics can be used to evaluate the performance of the array (i.e., capacity or error rate). In this chapter we use the MIMO ergodic capacity. From the EM tools we also derive the scattering parameters (i.e., S-parameters) to measure the antenna bandwidth and mutual coupling effects. These performance metrics are fed to the optimization algorithm that computes the optimal set of antenna parameters $\mathbf{x}^{\text{opt}}$.

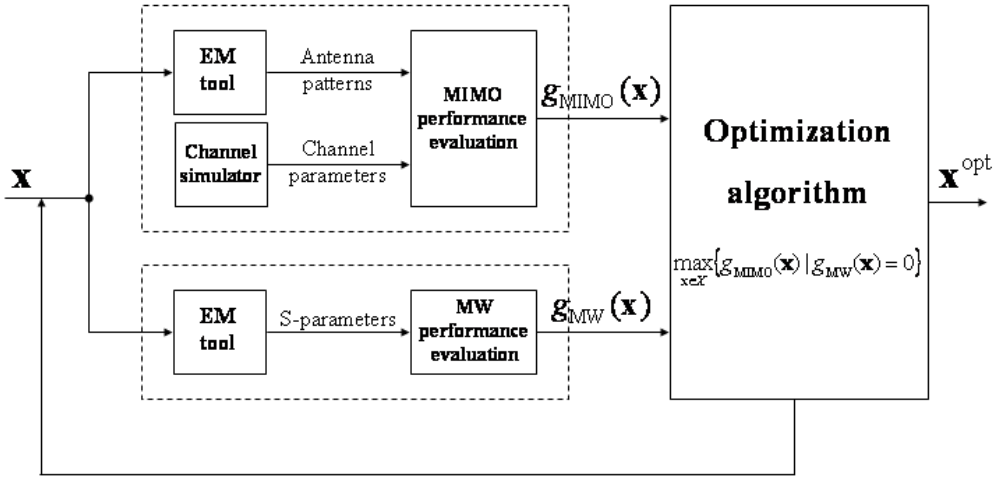

Figure 4.2: Block diagram of the proposed optimization algorithm for MIMO array designs exploiting pattern diversity.

4.3 CPA Analysis in Clustered MIMO Channels

Here we compute in closed-form the spatial correlation coefficients of CPAs in multi-cluster channel models. From these coefficients, we analytically derive a lower bound on the MIMO ergodic capacity and demonstrate that the CPA performance can be evaluated over a reduced set of channel parameters with minimal error. This result is used to simplify the proposed optimization algorithm, yielding significant reduction in computational complexity.

4.3.1 Spatial Correlation of CPAs in Multi-Cluster Channels

For a narrowband system with N_c clusters, the spatial correlation between the ℓ-th and m-th antennas of the MIMO array can be expressed as

$$r_{\ell,m} = \frac{1}{N_c} \sum_{i=1}^{N_c} r_{\ell,m}^{(i)} \tag{4.2}$$

where $r_{\ell,m}^{(i)}$ is the correlation coefficient corresponding to the i-th cluster, and the normalization factor before the summation is to satisfy the trace constraint of the spatial correlation matrix (i.e., $\mathrm{Tr}(\mathbf{R}) = N$).

In Section 3.2 we derived closed-form expressions of the correlation coefficients in single-cluster channels (i.e., $N_c = 1$). Now we compute analytically these correlation coefficients accounting for multiple clusters. To simplify this analysis we assume that the N_c clusters experience the same angle spread (i.e., $\sigma_\phi^{(i)} = \sigma_\phi$, $\forall i = 1, \ldots, N_c$). Under this assumption, substituting (3.11)

and (3.15) into (4.2), we write the auto- and cross-correlation coefficients as

$$\begin{aligned} r_{1,1}(N_c, \mathbf{\Phi}, \sigma_\phi) &= \frac{|\alpha(\rho, n)|^2}{\left(1 - e^{-\sqrt{2}\pi/\sigma_\phi}\right)} \frac{(n\sigma_\phi)^2}{1 + 2(n\sigma_\phi)^2} \\ &\quad \times \left[1 - e^{-\sqrt{2}\pi/\sigma_\phi} + \frac{1 - e^{-\sqrt{2}\pi/\sigma_\phi}\cos(n\pi)}{N_c(n\sigma_\phi)^2} \sum_{i=1}^{N_c} \cos^2(n\phi_c^{(i)})\right] \end{aligned} \tag{4.3}$$

and

$$r_{1,2}(N_c, \mathbf{\Phi}, \sigma_\phi) = \frac{|\alpha(\rho, n)|^2}{2N_c\left[1 + 2(n\sigma_\phi)^2\right]} \sum_{i=1}^{N_c} \sin(2n\phi_c^{(i)}). \tag{4.4}$$

Note that the auto-correlation coefficient for the second patch is derived from equation (4.3), accounting for the angle shift ($\phi_0^{(2)}$) across the two antennas, and $r_{2,2}(\phi_c, \sigma_\phi) = r_{1,1}(\phi_c - \phi_0^{(2)}, \sigma_\phi)$. Moreover, the cross-correlation coefficient $r_{2,1}$ has the same expression as (4.4).

4.3.2 Eigenvalue Analysis

The eigenvalues $\lambda_{(1,2)}$ of the 2×2 spatial correlation matrix ($\mathbf{R}$) are computed as

$$\begin{aligned} \lambda_{(1,2)} &= \lambda_{(1,2)}(N_c, \mathbf{\Phi}, \sigma_\phi) \\ &= \frac{1}{2}\left[(r_{1,1} + r_{2,2}) \pm \sqrt{4r_{1,2}r_{2,1} + (r_{1,1} - r_{2,2})^2}\right] \end{aligned} \tag{4.5}$$

where λ_1 and λ_2 are the maximum and minimum eigenvalues of spatial correlation matrix $\mathbf{R}$, respectively. The eigenvalues in (4.5) depend on the channel parameters (i.e., N_c, $\mathbf{\Phi}$ and σ_ϕ) through the spatial correlation coefficients in (4.3) and (4.4). Hereafter, we derive bounds to these eigenvalues for the CPA, assuming the mode number n is even. Similar results can be easily derived for n odd, by using similar approximation as in [110].

We expand the two terms in (4.5) within the brackets by substituting the correlation coefficients in (4.3) and (4.4), and obtain

$$\begin{aligned} r_{1,1}+r_{2,2} &= \frac{|\alpha(\rho,n)|^2}{\left(1-e^{-\sqrt{2}\pi/\sigma_\phi}\right)}\frac{(n\sigma_\phi)^2}{1+2(n\sigma_\phi)^2} \\ &\quad\times\left[2\left(1-e^{-\sqrt{2}\pi/\sigma_\phi}\right)+\frac{1-e^{-\sqrt{2}\pi/\sigma_\phi}\cos(n\pi)}{N_c(n\sigma_\phi)^2}\sum_{i=1}^{N_c}\left[\cos^2(n\phi_c^{(i)})+\sin^2(n\phi_c^{(i)})\right]\right] \\ &= \frac{|\alpha(\rho,n)|^2}{\left(1-e^{-\sqrt{2}\pi/\sigma_\phi}\right)}\frac{(n\sigma_\phi)^2}{1+2(n\sigma_\phi)^2}\left[2\left(1-e^{-\sqrt{2}\pi/\sigma_\phi}\right)+\frac{1-e^{-\sqrt{2}\pi/\sigma_\phi}\cos(n\pi)}{(n\sigma_\phi)^2}\right] \\ &\overset{(n \text{ even})}{=} |\alpha(\rho,n)|^2 \end{aligned} \tag{4.6}$$

and

$$\begin{aligned} 4r_{1,2}r_{2,1}+(r_{1,1}-r_{2,2})^2 &\overset{(n \text{ even})}{=} \left[\frac{|\alpha(\rho,n)|^2}{1+2(n\sigma_\phi)^2}\right]^2 \\ &\quad\times\left\{\left[\frac{1}{N_c}\sum_{i=1}^{N_c}\cos(2n\phi_c^{(i)})\right]^2+\left[\frac{1}{N_c}\sum_{i=1}^{N_c}\sin(2n\phi_c^{(i)})\right]^2\right\} \\ &\quad\leq\left[\frac{|\alpha(\rho,n)|^2}{1+2(n\sigma_\phi)^2}\right]^2. \end{aligned} \tag{4.7}$$

Note that the upper bound in (4.7) follows from the inequalities $\cos y \leq 1$ and $\sin y \leq 1$, $\forall y \in [0, 2\pi)$.

Substituting (4.6) and (4.7) into (4.5) we derive the bounds to the eigenvalues of the CPA as

$$\lambda_1(\sigma_\phi) \leq 1+\frac{1}{1+2(n\sigma_\phi)^2} \tag{4.8}$$

$$\lambda_2(\sigma_\phi) \geq 1-\frac{1}{1+2(n\sigma_\phi)^2}. \tag{4.9}$$

Fig. 4.3 compares the exact eigenvalue λ_2 in (4.5) against the lower bound in (4.9). The channel is simulated with $N_c = 2$, mean AOAs generated

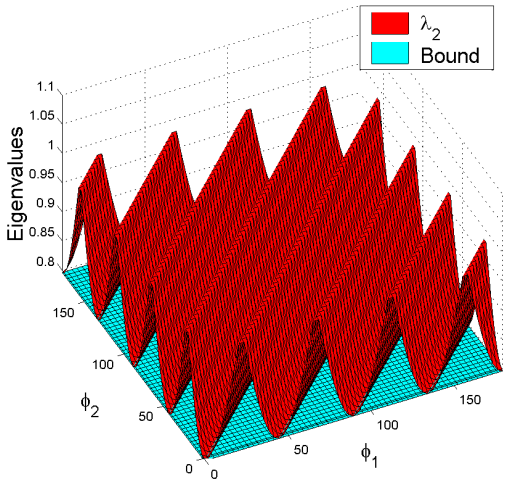

Figure 4.3: Exact eigenvalue (λ_2) and lower bound in (4.9) as a function of the mean AoAs ϕ_1 and ϕ_2. The channel is simulated with $N_c = 2$, mean AoAs generated in the range $[0, 180^{\text{o}}]$ and $\sigma_\phi = 20^{\text{o}}$.

in the range $[0, 180^{\text{o}}]$ and $\sigma_\phi = 20^{\text{o}}$. It is possible to see that the lower bound is close to the exact expression of λ_2 for any combination of values of ϕ_1 and ϕ_2, denoting the mean AOAs of the clusters.

In Fig. 4.4 we compare the bounds to λ_1 and λ_2 against their exact expressions as a function of the cluster AS and for different values of N_c. The mean AOAs are generated as $\phi_c^{(i)} = \tilde{\phi}(i-1)/N_c$ (with $i = 1, \ldots, N_c$ and $\tilde{\phi} = 120^{\text{o}}$) and variable AS ($\sigma_\phi$). Fig. 4.4 shows that the bounds in (4.8) and (4.9) are close to the exact expression of the eigenvalues in (4.5) for $\sigma_\phi > 15^{\text{o}}$. This value corresponds to the lowest AS defined in the IEEE 802.11n channel model [43], which makes the proposed bound practical for indoor environments

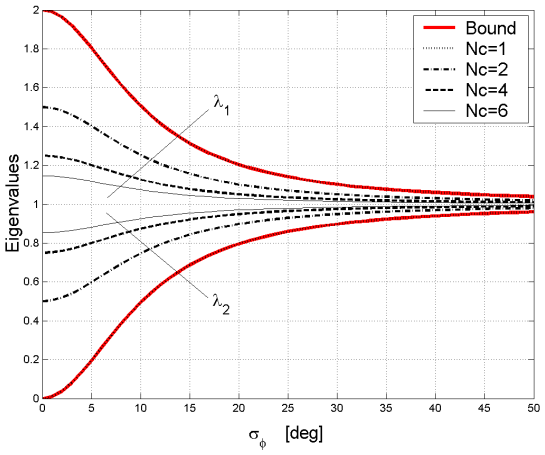

Figure 4.4: Exact eigenvalues (λ_1 and λ_2) and bounds in (4.8) and (4.9). The channel is simulated with variable N_c, mean AoAs generated as $\phi_c^{(i)} = \tilde{\phi}(i-1)/N_c$ (with $i = 1, \ldots, N_c$ and $\tilde{\phi} = 120^{\text{o}}$) and variable AS ($\sigma_\phi$).

in the context of WLANs.

4.3.3 Lower Bound on the Ergodic Capacity

In the subsection 4.2.1 we showed that clustered channel models are defined by a large set of parameters. Optimizing the design of 2-CPAs over many channel parameters to account for different propagation conditions would be computationally expensive. In this section we propose a simple lower bound on the MIMO ergodic capacity expressed as a function of a reduced set of channel parameters. We show this bound corresponds to the capacity of single-cluster channels. We use this bound to optimize CPA designs with respect to the worst case scenario, thereby reducing the computational complexity of the

optimization algorithm.

A tight lower bound on the MIMO ergodic capacity for zero-mean single-sided spatially correlated channels with $N_r \leq N_t$ was proposed in [111]

$$C \geq p \log \left[1 + \frac{\gamma_o}{N_t} \exp \left(\frac{1}{p} \left(\sum_{t=0}^{p-1} \psi(q-t) + \ln |\mathbf{R}| \right) \right) \right] \tag{4.10}$$

where $p = \min(N_r, N_t)$, $q = \max(N_r, N_t)$, γ_o is the average SNR and $\psi(\cdot)$ is the Euler Digamma function [111]. For the case of $N_r = N_t = 2$, equation (4.10) simplifies as

$$C \geq 2 \log \left[1 + \frac{\gamma_o}{2} \exp \left(\frac{\psi(1) + \psi(2)}{2} \right) \sqrt{|\mathbf{R}|} \right]. \tag{4.11}$$

From (4.8) and (4.9) we derive a lower bound on the determinant of $\mathbf{R}$ as

$$|\mathbf{R}| = \lambda_1 \lambda_2 \geq 1 - \frac{1}{\left[1 + 2(n\sigma_\phi)^2 \right]^2} \tag{4.12}$$

where n is the mode number (assumed to be even) and σ_ϕ is the cluster angle spread (assumed to be the same for all the clusters in the channel). Substituting (4.12) into (4.11) we obtain the following lower bound on the ergodic capacity of clustered MIMO channels with CPAs

$$C \geq 2 \log \left[1 + \frac{\gamma_o}{2} \exp \left(\frac{\psi(1) + \psi(2)}{2} \right) \sqrt{1 - \frac{1}{\left[1 + 2(n\sigma_\phi)^2 \right]^2}} \right]. \tag{4.13}$$

Note that (4.12) corresponds to the determinant of $|\mathbf{R}|$ obtained in single-cluster channels. Hence, equation (4.13) is the lower bound on the MIMO capacity achieved with CPAs in single-cluster channels.

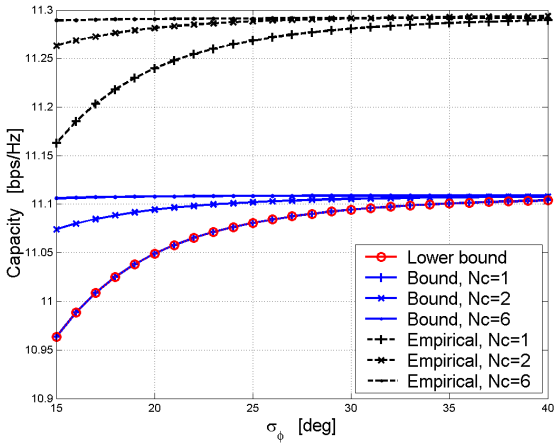

Figure 4.5: Exact and lower bounds to the MIMO ergodic capacity as a function of the angle spread (σ_ϕ) and different numbers of clusters (N_c) with $SNR = 20$ dB. The 2-CPA is simulated with $n = 4$.

Fig. 4.5 depicts the capacity lower bound in (4.13) as well as the lower bounds for different number of clusters (N_c) obtained from (4.11) by using the closed-form correlation coefficients of 2-CPAs derived in subsection 4.3.1. For reference, we report also the empirical capacity curves obtained by Monte Carlo simulations. The MIMO channel is simulated with variable angles spread (σ_ϕ) and $\gamma_o = 20$ dB. The 2-CPA is assumed to radiate with mode $n = 4$.

Fig. 4.5 shows that the lower bound in (4.13) is close to the bounds obtained from (4.11) for different number of clusters, for any value of angle spread. We observe that the bound in (4.13) coincides with the case of single-cluster channels (i.e., poor scattering). Moreover, the capacity loss due to this bound is only of $\sim 1\%$ compared to the case of $N_c = 6$ (i.e., rich scattering),

in the worst case scenario for indoor propagation environments defined by $\sigma_\phi = 15^o$ [43]. Hence, the lower bound for single-cluster channels in (4.13) can be used to predict the MIMO channel capacity in any propagation condition with minimal error. Interestingly, Fig. 4.5 also demonstrates that 2-CPAs with $n = 4$ are robust design solutions in any clustered MIMO channel, since they provide similar capacity either in poor or rich scattering environments.

4.4 MIMO Communication Performance Metrics

In this section, we first present a new definition of spatial correlation, particularly suitable for studies on pattern diversity. Then, we employ this definition to numerically compute the capacity performance of CPAs in different propagation scenarios as a function of the antenna parameters. Finally, we propose two MIMO communication performance metrics that will define the objective function of the proposed optimization algorithm.

4.4.1 Normalized Spatial Correlation

The general definition of spatial correlation between the ℓ-th and m-th elements of MIMO arrays is given by [112, 113]

$$r_{\ell,m} = \frac{\int_{4\pi} S(\Omega)\underline{E}_\ell(\Omega)\underline{E}_m^*(\Omega)d\Omega}{\left[\int_{4\pi} S(\Omega)\left|\underline{E}_\ell(\Omega)\right|^2 d\Omega \int_{4\pi} S(\Omega)\left|\underline{E}_m(\Omega)\right|^2 d\Omega\right]^{1/2}} \tag{4.14}$$

where $\Omega = (\phi, \theta)$ is the solid angle, $S(\Omega)$ is the PAS of the scattered fields and $\underline{E}_\ell(\Omega)$ is the far-field of the ℓ-th antenna of the CPA. Note that (4.14) is derived from (2.14), where we removed the phase term due to the array element

spacing since the antennas of the CPA are collocated. Equation (4.14) can be simplified as in [100], by using the following normalization [29]

$$\int_{4\pi} S(\Omega) \left|\underline{E}_\ell(\Omega)\right|^2 d\Omega = 1 \tag{4.15}$$

defined $\forall \ell = 1, \ldots, N$. The normalization in (4.15), however, holds only when either $S(\Omega)$ is uniformly distributed over the domain of integration or the antennas are characterized by isotropic radiation patterns.

In the most general case of "clustered" channel models (where the scattered energy is concentrated around the mean AOAs of the clusters) and no isotropic antenna radiation patterns (as for antenna designs exploiting pattern diversity), equation (4.15) is not satisfied for any channel conditions, since the antenna gain may vary as a function of the clusters mean AOA. Then, we define a new spatial correlation model as

$$r_{\ell,m} = \frac{\displaystyle\int_{4\pi} S(\Omega)\underline{E}_\ell(\Omega)\underline{E}^*_m(\Omega)d\Omega}{\displaystyle\int_{4\pi} S(\Omega) \left|\underline{E}_{\text{iso}}(\Omega)\right|^2 d\Omega} \tag{4.16}$$

where $\underline{E}_{\text{iso}}(\Omega)$ is the far-field of ideal isotropic radiators. Note that the envelope of (4.16) is not guaranteed to be lower than one, as for the conventional definition of correlation in (4.14), since we normalize the spatial correlation with respect to the antenna gain of ideal isotropic radiators. Moreover, we assume

$$\int_{4\pi} S(\Omega)d\Omega = \int_{4\pi} \left|\underline{E}_{\text{iso}}(\Omega)\right|^2 d\Omega = \int_{4\pi} \left|\underline{E}_\ell(\Omega)\right|^2 d\Omega = 1 \tag{4.17}$$

where the first term of the equality is the condition for $S(\Omega)$ to be a p.d.f., whereas the last two equalities define the transmit power constraint $\forall \ell =$

$1, \ldots, N$. Consistent with the measurement results in [4], we assume the PAS over the θ angles is independent from the ϕ angles and most of the scattered energy propagates over the azimuth directions. Then, we write $S(\Omega) = P(\phi - \phi_c)\delta(\theta - \pi/2)$, where ϕ_c is the mean AOA of the cluster and $P(\phi)$ is generated according to the truncated Laplacian distribution in (2.1).

In the previous section we derived the closed-form expression of the auto- and cross-correlation coefficients of CPAs assuming ideal radiation patterns. In practical designs, near-field effects may produce pattern distortion and affect the performance of the CPA. Hereafter, we evaluate (4.16) numerically by employing realistic antenna radiation patterns computed with FEKO, an EM software tool based on the method of moments.

4.4.2 CPA Performance in Clustered MIMO Channels

We evaluate the MIMO capacity of different CPA designs as a function of the channel characteristics, by varying the physical parameters of the circular patch antennas. A closed-form exact expression of the MIMO ergodic capacity (with equal power allocation across the transmit antennas) for double-sided spatially correlated channels was proposed in [114]. Here, we compute the capacity in [114] by using the our definition of spatial correlation in (4.16), which are a function of both channel and antenna parameters. Our goal is to evaluate the performance of CPAs employed either at the transmit or receive sides, thus we assume only single-sided spatially correlated channels. Moreover, we consider only single-cluster channels, for the reason explained in

subsection 4.3.3.

Fig. 4.6 depicts the MIMO ergodic capacity of the CPA as a function of the cluster mean AOA ($\phi_{\rm c}$) and per-cluster angle spread (σ_ϕ), with $SNR = 10$ dB. The CPA is simulated with parameters $\rho_{\rm o} = 0.45\lambda$ and $\rho_{\rm f} = 0.64\rho_{\rm o}$, $h = 1.575$ mm and $\epsilon_r = 2.2$ to excite mode 3. The radiation patterns of the two antenna elements of the CPA is given in Fig. 4.7(b). We observe that the capacity in Fig. 4.6 increases as a function of the AS and saturates to its maximum value for $\sigma_\phi > 15^{\rm o}$. Moreover, the capacity varies with respect to the mean AOA, unlike the theoretical results presented in [110]. These oscillations are due to the irregularity of the antenna radiation patterns in Fig. 4.7(b) (produced by near-field effects), and the notches in the capacity curve occur at the angles $\phi_{\rm c} = 15^{\rm o}, 195^{\rm o}$ due to the reduced power radiated towards those angular directions.

Next, we evaluate the CPA performance with different antenna parameters. We consider three values of radius of the circular microstrip antennas: $\rho_{\rm o} = 0.39\lambda$, 0.45λ, 0.51λ. In Fig. 4.7 we observe that, by varying the radius $\rho_{\rm o}$ and for fixed frequency of operation (i.e., 2.4 GHz as for WLANs), the shape and gain of the antenna radiation patterns vary. The value of $\rho_{\rm o} = 0.45\lambda$ corresponds to the resonant frequency for mode 3 (with $h = 1.575$ mm and $\epsilon_r = 2.2$) as shown in subsection 3.1.4. We observe that the patterns in Fig. 4.7(b) are irregular due to mutual coupling effects, unlike the ideal radiation pattern depicted in Fig. 3.2(c) for mode 3. Moreover, by varying the radius $\rho_{\rm o}$ for fixed carrier frequency, it is not possible to excite mode 3 in the microstrip

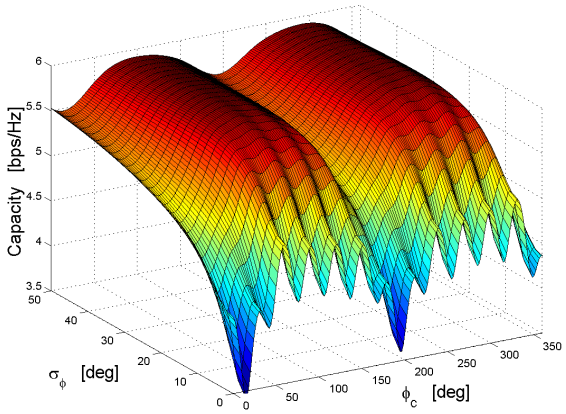

Figure 4.6: Ergodic capacity of the CPA as a function of the cluster mean AOA (ϕ_{c}) and per-cluster AS (σ_{ϕ}), with $SNR = 10$ dB, $\rho_{\mathrm{o}} = 0.45\lambda$ and $\rho_{\mathrm{f}} = 0.64\rho_{\mathrm{o}}$.

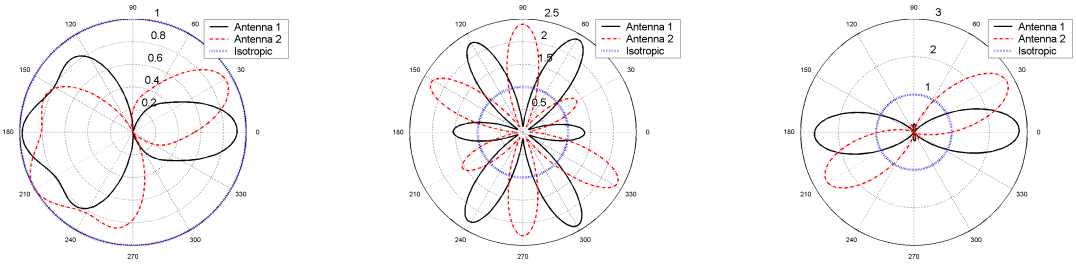

(a) $\rho_{\mathrm{o}} = 0.39\lambda$ (b) $\rho_{\mathrm{o}} = 0.45\lambda$ (c) $\rho_{\mathrm{o}} = 0.51\lambda$

Figure 4.7: Radiation patterns (over the azimuth plane) of the two elements of the CPA for different values of physical radius ρ_{o}, with $\rho_{\mathrm{f}} = 0.64\rho_{\mathrm{o}}$.

anymore, consistently to equation (3.4). As a result, for $\rho_{\mathrm{o}} = 0.39\lambda$ the antenna gains are lower than ideal isotropic radiators, while for $\rho_{\mathrm{o}} = 0.51\lambda$ all

the energy is radiated in two opposite spatial directions.

The effect of these radiation patterns on the systems performance is shown in Fig. 4.8, where we plot the MIMO ergodic capacity as a function of ϕ_c for the three values of ρ_o above. In the same figure we plot also the "ideal" MIMO capacity derived in i.i.d. channels, as reference. We note that the best performance is achieved for $\rho_o = 0.45\lambda$ due to the effect of pattern diversity, whereas for $\rho_o = 0.51\lambda$ the capacity reaches its maximum only in those spatial direction with high antenna gain. Note that the capacity produced by the CPAs may be higher than the ideal capacity due to the power normalization in (4.16) with respect to the gain of isotropic radiators. Here, the physical interpretation of "ideal" performance can be described as the capacity achievable by two ideal isotropic radiators spaced apart at distance much greater than the wavelength (i.e., ideal array exploiting space diversity).

These results reveal that the CPA performance in realistic clustered MIMO channels is sensitive to the antenna parameters. Hereafter, we propose simple metrics to measure the statistical performance of CPAs in clustered channels, that will be used by the proposed optimization algorithm.

4.4.3 Performance Metrics for Optimization Algorithms

One common metric to evaluate the performance of MIMO arrays exploiting pattern diversity is the *inner product* of the antenna radiation pat-

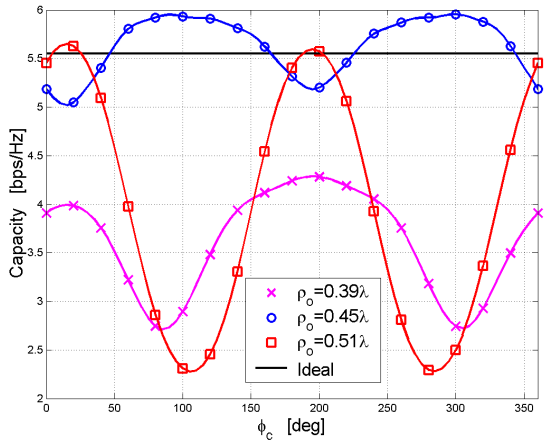

Figure 4.8: Ergodic capacity of the CPA as a function of the cluster mean AOA, with $\sigma_\phi = 20^o$ and $SNR = 10$ dB.

terns [112, 113, 115]

$$\langle \underline{E}_\ell, \underline{E}_m \rangle = \frac{\int_{4\pi} \underline{E}_\ell(\Omega)\underline{E}_m^*(\Omega)d\Omega}{\left[\int_{4\pi} |\underline{E}_\ell(\Omega)|^2 \, d\Omega \int_{4\pi} |\underline{E}_m(\Omega)|^2 \, d\Omega\right]^{1/2}}. \tag{4.18}$$

This metric is derived from (4.14) under the simplistic assumption of uniform distribution of the multipaths (i.e., $S(\Omega)$ has uniform pdf). It is well known that the assumption of uniformly distributed PAS is not realistic and overestimates the MIMO channel capacity [116]. In realistic clustered channel environments, the MIMO ergodic capacity is a function of the cluster mean AOA and AS, as shown in Fig. 4.6. To solve the optimization algorithm for MIMO arrays, however, it is desirable to remove the dependence of the objective function on the channel parameters and express it only as a function of the

antenna physical characteristics, as for the metric in (4.18). Hence, we propose two performance metrics derived from the ergodic capacity that are independent on the channel parameters and measure the statistical performance of MIMO arrays in clustered channels.

We denote with $C(\mathbf{x}; \phi_{\mathrm{c}}, \sigma_{\phi})$ the ergodic capacity as a function of the channel parameters for given CPA design described by $\mathbf{x}$. We define the *mean capacity* ($\overline{C}$) as

$$\begin{aligned} \overline{C}(\mathbf{x}) &= \mathcal{E}_{\phi_{\mathrm{c}},\sigma_{\phi}}\{C(\mathbf{x}; \phi_{\mathrm{c}}, \sigma_{\phi})\} \\ &= \int_{0}^{\infty} C(\mathbf{x}; \phi_{\mathrm{c}}, \sigma_{\phi}) f_{\phi_{\mathrm{c}},\sigma_{\phi}}(\phi_{\mathrm{c}}, \sigma_{\phi}) d\phi_{\mathrm{c}} d\sigma_{\phi} \end{aligned} \tag{4.19}$$

where $f_{\phi_{\mathrm{c}},\sigma_{\phi}}(\cdot)$ is the joint p.d.f. of ϕ_{c} and σ_{ϕ}, and we assume ϕ_{c} and σ_{ϕ} are independent and with uniform distributions, that is reasonable assumption for practical channel models. The mean capacity measures the average performance of the array in different propagation scenarios. Additionally, it is desirable to account for the notches in the capacity curve in Fig. 4.6, by introducing a notion of "outage". We define the 10% *outage capacity* ($C_{10\%}$) as

$$P\left[C(\mathbf{x}; \phi_{\mathrm{c}}, \sigma_{\phi}) \leq C_{10\%}(\mathbf{x})\right] = \int_{0}^{C_{10\%}(\mathbf{x})} C(\mathbf{x}; \phi_{\mathrm{c}}, \sigma_{\phi}) f_{\phi_{\mathrm{c}},\sigma_{\phi}}(\phi_{\mathrm{c}}, \sigma_{\phi}) d\phi_{\mathrm{c}} d\sigma_{\phi} = 10\% \tag{4.20}$$

where P denotes the probability of a random variable. Note that the ergodic capacity $C(\mathbf{x}; \phi_{\mathrm{c}}, \sigma_{\phi})$ in (4.19) and (4.20) is numerically evaluated through the closed-form expression in [114] and using the definition of spatial correlation in (4.16).

Fig. 4.9 compares the three metrics mentioned above: the mean capacity in (4.19), the 10% outage capacity in (4.20) and the conventional envelope of the inner product in (4.18). The circular patch antennas are simulated through FEKO with $\rho_{\mathrm{f}} = 0.8\rho_{\mathrm{o}}$, $h = 1.575$ mm and $\epsilon_r = 6$. Different values of radius are considered $\rho_{\mathrm{o}} = 0.12\lambda, 0.2\lambda, 0.29\lambda, 0.36\lambda, 0.44\lambda$ to excite modes $n = 1, 2, 3, 4, 5$, respectively. Note that some values of ρ_{o} are slightly different from the theoretical ones reported in Fig. 3.1 due to near-field effects between the two antenna elements of the CPA. In Fig. 4.9 it is possible to see that both

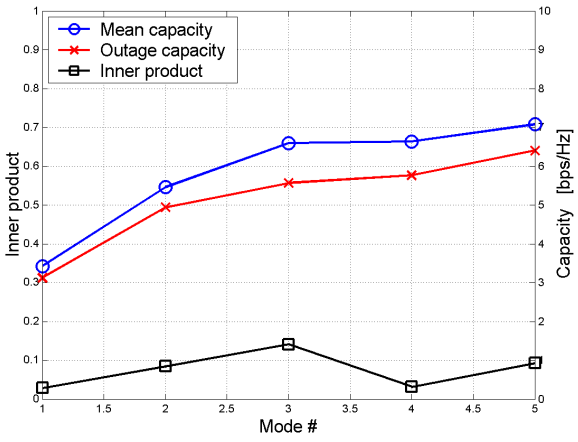

Figure 4.9: Comparison of different metrics to evaluate the performance of pattern diversity.

mean and outage capacity increase as a function of the mode number due to the beneficial effect of pattern diversity, consistently to the theoretical results presented in Chapter 3. On the other hand, we observe that the inner product oscillates around the value of 0.1, since the radiation patterns are orthogonal

for any mode number. This result demonstrates that (4.19) and (4.20) are better measures of the effect of pattern diversity on systems performance, in realistic clustered MIMO channels, than the conventional inner product (4.18).

Finally, we compute the metrics in (4.19) and (4.20) as a function of the antenna parameters. Fig. 4.10(a) and Fig. 4.10(b) show the mean and outage capacity versus radius (ρ_{o}) and feeding location (ρ_{f}) of the circular microstrip antennas (with $h = 1.575$ mm and $\epsilon_r = 2.2$). It is possible to see that in both cases the maximum is reached for $\rho_{\mathrm{o}} \approx 0.45\lambda$ for most of the values of ρ_{f}. These functions will be used in the optimization algorithm to determine the best values of antenna parameters on the communication theoretic point of view.

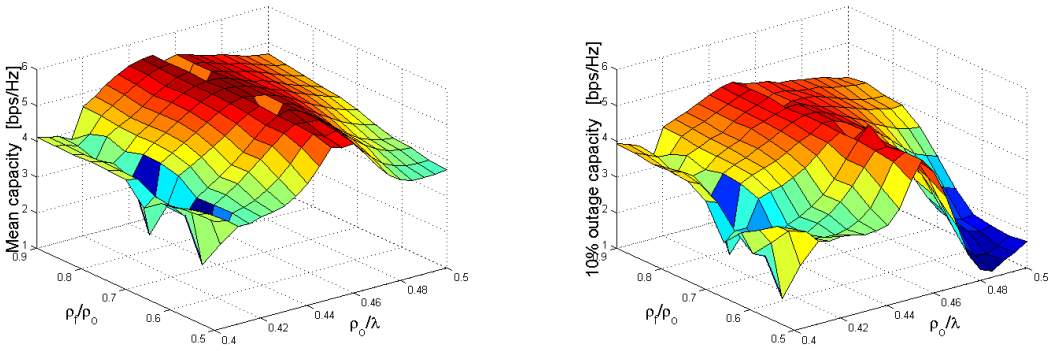

(a) Mean capacity $\overline{C}(\mathbf{x})$

(b) Outage capacity $C_{10\%}(\mathbf{x})$

Figure 4.10: Mean and 10% outage capacity as a function of the physical radius (ρ_{o}) and the feed location (ρ_{f}). The mean and 10% outage capacity are computed through (4.19) and (4.20), respectively. The two antennas of the CPA are designed with physical parameters $h = 1.575$ mm and $\epsilon_r = 6$.

4.5 Microwave Theory Performance Metrics

Hereafter, we present different metrics from microwave theory used to evaluate the efficiency of CPA designs as a function of the physical antenna parameters.

4.5.1 S-parameters

The antenna efficiency depends on the losses at the input or within the structure of an antenna, and indicates the amount of radiated power for given input power [98]. The antenna efficiency is generally measured in terms of return loss or S_{11} and S_{22} scattering parameters, for 2-port antenna designs. Typical target value used to measure the bandwidth of S_{11} and S_{22} is -10 dB.

Due to the proximity of the two circular patch antennas, the performance of the CPA may be affected by mutual coupling effects. Mutual coupling results in distortion of the antenna radiation patterns [117–121] and power loss [122–124]. The effect of pattern distortion on the MIMO channel capacity was shown in Section 4.4.2. Power loss due to mutual coupling is generally measured in terms of the S_{12} and S_{21} scattering parameters, for 2-element arrays. The target value for the bandwidth of S_{12} and S_{21} is -20 dB.

4.5.2 Performance Metrics for Optimization Algorithms

The values of the S-parameters, expressed as a function of the frequency, depend on the physical characteristics of the antennas. To optimize the physical parameters of CPA designs we employ the bandwidth BW_{11} and

BW_{22} defined as the measure of the set of frequencies for which $|S_{11}|$ and $|S_{22}|$ are below -10 dB, respectively. Similarly, BW_{12} and BW_{21} denote the bandwidth of $|S_{12}|$ and $|S_{21}|$, respectively, for the target -20 dB.

Fig. 4.11 depicts the bandwidths BW_{11} and BW_{22} for the two ports of the CPA as a function of the radii $\rho_{\rm o}^{(1)}$ and $\rho_{\rm o}^{(2)}$ of the two patches. The bandwidth is expressed in percentage value with respect to the carrier frequency $f_{\rm c} = 2.44$ GHz for WLANs and is measured within the frequency band $[2.2, 2.7]$ GHz. Moreover, the substrate of the bottom and top patches are characterized by $\epsilon_r^{(1)} = 2.2$ and $\epsilon_r^{(2)} = 8$, respectively. We observe that BW_{11} and BW_{22} reach values of $\sim 5\%$ for $\rho_{\rm o}^{(1)} \approx 0.42\lambda$ and $\rho_{\rm o}^{(2)} \approx 0.22\lambda$. These are the values radius for which the two patch antennas resonate with mode 3 for the given values of ϵ_r, similarly to the theoretical results in Fig. 3.1.

Note that the bandwidth of the circular patch antennas is also a function of the substrate height h and dielectric constant ϵ_r, feed location $\rho_{\rm f}$ and size of the ground plane $\rho_{\rm gp}$ as shown in [98,109]. To optimize the CPA design over these physical parameters we formulate a multidimensional optimization algorithm as in the following section.

4.6 Optimization Algorithm for 2-CPA Designs

So far, we studied the performance of CPA designs as a function of the antenna parameters and defined different metrics. Here, we present a novel algorithm to optimize the performance of CPAs by jointly maximizing performance metrics from communication theory (i.e., MIMO channel capacity) and

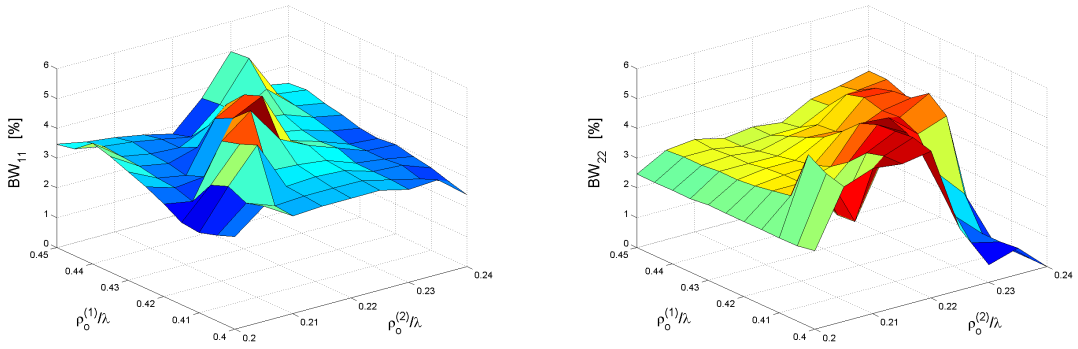

Figure 4.11: Bandwidth BW_{11} and BW_{22} as a function of the radia $\rho_{\mathrm{o}}^{(1)}$ and $\rho_{\mathrm{o}}^{(2)}$ of the two patch antennas of the CPA. The antenna parameters are: $\rho_{\mathrm{f}}^{(1)} = 0.9\rho_{\mathrm{o}}^{(1)}$, $h^{(1)} = 9$ mm, $\epsilon_r^{(1)} = 2.2$, $\rho_{\mathrm{gp}}^{(1)} = 2\rho_{\mathrm{o}}^{(1)}$, $\rho_{\mathrm{f}}^{(2)} = 0.8\rho_{\mathrm{o}}^{(2)}$, $h^{(2)} = 7$ mm, $\epsilon_r^{(2)} = 8$, $\rho_{\mathrm{gp}}^{(2)} = 1.8\rho_{\mathrm{o}}^{(2)}$.

microwave theory (i.e., bandwidth).

In Fig. 4.10 we showed that mean and outage capacity of the CPA vary as a function of $\mathbf{x}$. We define the objective function of the optimization algorithm based on *MIMO communication performance* as

$$\mathrm{g}_{\mathrm{MIMO}}(\mathbf{x}) = w_1\overline{C}(\mathbf{x}) + w_2 C_{10\%}(\mathbf{x}) \tag{4.21}$$

where w_1 and w_2 are weighting values. Note that the values of w_1 and w_2 can be chosen depending on whether the design has to be optimized with respect to average or outage performance.

Similarly, Fig. 4.11 shows the antenna bandwidth is also a function of $\mathbf{x}$. We denote the bandwidth of the scattering parameter S_{ij} as $BW_{ij}(\mathbf{x}) =$

$|[\underline{f}_{ij}(\mathbf{x}), \overline{f}_{ij}(\mathbf{x})]|$, where $|\cdot|$ is the measure of a set and $\underline{f}_{ij}$ and $\overline{f}_{ij}$ characterize the range of frequencies that satisfy the predefined target (i.e., -10 dB for S_{11} and S_{22}, -20 dB for S_{12} and S_{21}). Moreover, we define $\mathcal{BW} = [\underline{f}, \overline{f}]$ as the target frequency band. For designs conceived for WLANs applications, we assume $\mathcal{BW} = [2.4, 2.48]$ GHz. With these definitions, we write the *microwave theory performance* metric as

$$\mathrm{g}_{\mathrm{MW}}(\mathbf{x}) = I_{A_{11}}(\mathbf{x})\ I_{A_{22}}(\mathbf{x})\ I_{A_{12}}(\mathbf{x})\ I_{A_{21}}(\mathbf{x}) - 1 \tag{4.22}$$

where $A_{ij} = \{\mathbf{x}|\underline{f}_{ij}(\mathbf{x}) \leq \underline{f}, \overline{f}_{ij}(\mathbf{x}) \geq \overline{f}\}$ and $I_{A_{ij}}(\cdot)$ denotes the indicator function[2].

The goal of the proposed optimization algorithm is to determine the CPA design that provides statistically the best capacity performance in correlated channels, while satisfying predefined target bandwidth requirements. Hence, we use (4.21) as objective function and (4.22) to define the (non-linear) equality constraint, and formulate the optimization problem as

$$\mathbf{x}^{\mathrm{opt}} = \arg\max_{\mathbf{x}\in\mathcal{X}} \{\mathrm{g}_{\mathrm{MIMO}}(\mathbf{x})|\mathrm{g}_{\mathrm{MW}}(\mathbf{x}) = 0\} \tag{4.23}$$

where the feasible set is given by

$$\mathcal{S} = \{\mathbf{x} \in \mathcal{X}|\mathrm{g}_{\mathrm{MW}}(\mathbf{x}) = 0\}\,. \tag{4.24}$$

[2]The indicator function is defined as

$$I_A(y) = \begin{cases} 1 & \text{if } y \in A; \\ 0 & \text{otherwise.} \end{cases}$$

Finally, we solve the optimization problem in (4.23) and find that the antenna parameters that optimize the performance of the CPA are $\rho_{\mathrm{o}}^{(1)} = 0.43\lambda$ and $\rho_{\mathrm{o}}^{(2)} = 0.22\lambda$, with $\rho_{\mathrm{f}}^{(1)} = 0.9\rho_{\mathrm{o}}^{(1)}$, $h^{(1)} = 9$ mm, $\epsilon_r^{(1)} = 2.2$, $\rho_{\mathrm{gp}}^{(1)} = 2\rho_{\mathrm{o}}^{(1)}$, $\rho_{\mathrm{f}}^{(2)} = 0.8\rho_{\mathrm{o}}^{(2)}$, $h^{(2)} = 7$ mm, $\epsilon_r^{(2)} = 8$, $\rho_{\mathrm{gp}}^{(2)} = 1.8\rho_{\mathrm{o}}^{(2)}$. Fig. 4.12 shows the S-parameters for our proposed CPA design. We observe that the return loss $|S_{11}|$ and $|S_{22}|$ for the two ports of the CPA is below -10 dB within the target frequency band $\mathcal{BW} = [2.4, 2.48]$ GHz for WLANs. Similarly, the parameters $|S_{12}|$ and $|S_{21}|$ are way below -20 dB within $\mathcal{BW}$, guaranteeing very good isolation between the two ports of the CPA.

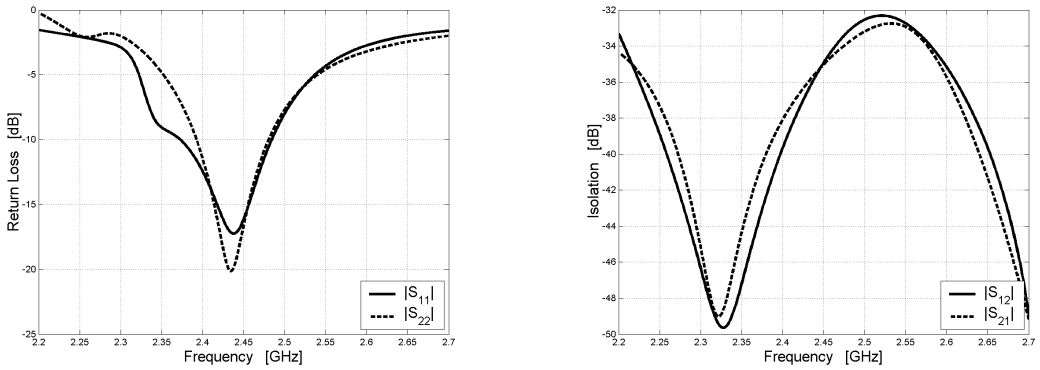

Figure 4.12: S-parameters for the optimized CPA design with $\rho_{\mathrm{o}}^{(1)} = 0.43\lambda$ and $\rho_{\mathrm{o}}^{(2)} = 0.22\lambda$.

Chapter 5

Capacity Analysis of Adaptive MIMO Systems

MIMO technology exploits the spatial components of the wireless channel to provide significant capacity gain and increased link robustness, through multiplexing and diversity techniques. Understanding the tradeoffs between multiplexing and diversity schemes is critical in designs of adaptive algorithms that switch between different MIMO schemes as a function of the propagation conditions. One way to study these diversity/multiplexing tradeoffs in spatially correlated channels is by theoretical capacity analysis. This chapter first presents a general overview on adaptive MIMO systems. Then, theoretical closed-form capacity expressions are derived for different types of space-time encoder/decoders in spatially correlated channels. These capacity expressions are used to analyze the relative performance of the MIMO transmission schemes in different propagation scenarios.

5.1 Introduction

This section first presents a background on adaptive MIMO systems. Then describes the system and channel models used for theoretical capacity analysis. Finally, it provides an overview on common MIMO transmission

techniques and reviews some recent advances in the analysis of the theoretical capacity of these schemes in spatially correlated channels.

5.1.1 Background on Adaptive MIMO Systems

Various MIMO techniques such as beamforming, spatial multiplexing, space-time coding (see [33] and references within) have been proposed to exploit the channel characteristics in different ways. The suitability and performance of a given MIMO technique depends on the channel characteristics. For instance, for line-of-sight (LOS) rank-deficient channels, or channels with high levels of spatial correlation, it is well known that robust diversity-based schemes such as beamforming or space-time coding should be employed. On the other hand, for rich-scattering environments spatial multiplexing techniques yielding high spectral efficiencies are more appropriate.

Performance tradeoffs between multiplexing and diversity have been studied in an information-theoretic sense in [125]. Practical adaptive algorithms to switch between transmit diversity (TD) and spatial multiplexing schemes were proposed in [126, 127]. The algorithm described in [126] exploited the instantaneous channel knowledge to improve error rate performance for fixed data rate transmission. The adaptive method in [127] was designed to enhance spectral efficiency, exploiting statistical time/frequency selectivity indicators.

Alternatively, the spatial selectivity of the channel is another dimension that can be explored. The spatial selectivity, defined as in [71], depends

on the characteristics of the propagation environment such as angle spread, number of scatterers, angle of arrival/departure [16, 24]. The effect of the spatial selectivity is to create statistically uncorrelated signals across different antennas of the MIMO array and it is typically revealed through the eigenvalues of the transmit and receive spatial correlation matrices [128]. The spatial correlation across the array elements affects the capacity [33] and error rate performance [73] of MIMO systems.

In this dissertation we present a new MIMO transmission approach that adapts to the changing channel conditions based on the spatial selectivity information. The proposed system switches between different MIMO transmission schemes as a means of approaching the spatially-correlated MIMO channel capacity with low-complexity. Since the adaptation is based on the long-term spatial characteristics of the channel, it can be carried out at slow rate, avoiding feedback overhead.

We consider four low-complexity open-loop MIMO schemes, namely statistical beamforming (BF)[1], orthogonal space-time block codes (OSTBC), double space-time transmit diversity (D-STTD) and spatial multiplexing (SM). In this chapter we derive new closed-form capacity results for BF, OSTBC, D-STTD and SM with linear receivers, and demonstrate the significant information-theoretic improvements obtained by adapting between these schemes based on the spatial selectivity information. We also show that the capacity of our low-

[1]We define statistical BF as an open-loop scheme, under the assumption of uplink/downlink reciprocity of the channel spatial statistics.

complexity system approaches that of the optimal solution. We then derive accurate analytical approximations for the signal-to-noise ratios (SNR) corresponding to the crossing-points of the BF, OSTBC and SM capacity curves. These crossing-points determine the relative performance of the transmission schemes, and are shown to depend explicitly on the channel statistics through the eigenvalues of the spatial correlation matrices.

5.1.2 System and Channel Models

We model the receive signal vector of a narrowband MIMO system, employing N_t transmit and N_r receive antennas, as in (3.1)

$$\mathbf{y} = \sqrt{\gamma}\,\mathbf{H}\mathbf{x} + \mathbf{n} \tag{5.1}$$

where $\mathbf{x} \in \mathbb{C}^{N_t \times 1}$ is the transmit signal vector satisfying the power constraint $E\left[\mathbf{x}^{\dagger}\mathbf{x}\right] = N_t$, and $\mathbf{n} \in \mathbb{C}^{N_r \times 1}$ is the noise vector $\sim \mathbb{CN}\left(\mathbf{0}_{N_r \times 1}, \mathbf{I}_{N_r}\right)$. Also, $\mathbf{H} \in \mathbb{C}^{N_r \times N_t}$ is the spatially-correlated Rayleigh fading channel matrix, assumed to be known perfectly at the receiver, $\gamma = \gamma_{\mathrm{o}}/N_t$ is the average SNR per transmit antenna, $\gamma_{\mathrm{o}} = E_s/N_{\mathrm{o}}$ is the average SNR, E_s is the average energy per transmit symbol and N_{o} is the noise variance.

Under the narrowband assumption, we simplify the model for correlated Rayleigh MIMO channels in (2.12) as

$$\mathbf{H} = \mathbf{R}^{1/2}\mathbf{Z}\mathbf{S}^{1/2} \tag{5.2}$$

where $\mathbf{Z} \in \mathbb{C}^{N_r \times N_t}$ contains independent complex i.i.d. Gaussian entries with zero mean and unit variance, and $\mathbf{S}$ and $\mathbf{R}$ denote the transmit and receive

spatial correlation matrices respectively. We normalize the MIMO channel matrix such that $\mathcal{E}\left[||\mathbf{H}||_F^2\right] = N_r N_t$ and define

$$\mathbf{R}_H = \mathbf{S} \otimes \mathbf{R}. \tag{5.3}$$

The matrices $\mathbf{R}_H$, $\mathbf{S}$ and $\mathbf{R}$ have the eigenvalue decompositions

$$\mathbf{R}_H = \mathbf{U}_H \mathbf{\Lambda}_H \mathbf{U}_H^\dagger, \qquad \mathbf{S} = \mathbf{U}_s \mathbf{\Lambda}_s \mathbf{U}_s^\dagger, \qquad \mathbf{R} = \mathbf{U}_r \mathbf{\Lambda}_r \mathbf{U}_r^\dagger. \tag{5.4}$$

5.1.3 MIMO Transmission Techniques

This section reviews four common MIMO transmission schemes: BF, OSTBC, D-STTD and SM. These schemes have been actively considered by different standardization bodies [8–11, 13–15] and will be part of the adaptive MIMO transmission method proposed in this Chapter 7.

Beamforming (BF) schemes multiply the transmit symbols by the complex weights of a spatial filter. With $n_s = 1$, the transmit signal in (5.1) is a vector $\mathbf{x}$ defined as

$$\mathbf{x} = \mathbf{w}a \tag{5.5}$$

where $a \in \mathbb{C}$ is the transmit symbol and $\mathbf{w} \in \mathbb{C}^{N_t \times 1}$ is the weight vector. There are two ways of implementing beamforming: based on the instantaneous or statistical channel information. When *instantaneous* BF is employed, the transmitter needs to know the channel state information (CSI) via feedback channels or by exploiting the uplink/downlink channel reciprocity. *Statistical* BF estimates the weight vector from the dominant eigenvector of the chan-

nel spatial correlation matrix and, hence, feedbacks are not required if the uplink/downlink reciprocity of the channel statistics can be exploited.

Statistical BF is in fact the optimal transmission strategy in the low SNR regime, when only the channel distribution information is available at the transmitter. The optimality condition for BF to be capacity achieving was derived in [129] for multiple-input single-output (MISO) systems. These results were extended to MIMO systems in [130,131] for single-sided correlated and Rician channels and in [132] for double-sided correlated channels. Knowing the optimal solution of the transmit covariance matrix, it is possible to derive bounds and exact expressions of the ergodic capacity. The main results in this area are derived for MISO systems in [133] and for MIMO systems in [134, 135], where exact expressions of the ergodic capacity and cumulative density function of the mutual information were computed for single-sided correlated MIMO channels. In this chapter, new closed-form capacity expressions are derived to extend these results to double-sided spatially correlated channels.

Orthogonal Space-Time Block Codes (OSTBC) transmits parallel streams over n_s consecutive symbol periods and the symbols are encoded across different antennas. For the Alamouti scheme [35], the transmit signal matrix $\mathbf{X}$ in (5.1) is given by

$$\mathbf{X} \triangleq \left[\begin{array}{cc} \mathbf{x}(0) & \mathbf{x}(1) \end{array} \right] = \left[\begin{array}{cc} a_1 & -a_2^* \\ a_2 & a_1^* \end{array} \right] \tag{5.6}$$

where $\mathbf{x}(0)$ and $\mathbf{x}(1)$ are the transmit signal vectors for the first and second symbol periods, respectively. In the following sections we propose a novel

closed-form capacity expression for OSTBC in double-sided correlated MIMO channels.

Double space-time transmit diversity (D-STTD) scheme was first proposed in [38] to achieve both diversity and multiplexing gains. D-STTD transmits parallel streams over four antennas in $n_s = 2$ consecutive symbol periods, and the symbols are encoded over each pair of antennas according to the Alamouti scheme [35]. For D-STTD scheme, the transmit signal matrix $\mathbf{X}$ in (5.1) is given by

$$\mathbf{X} \triangleq \left[\begin{array}{cc} \mathbf{x}(0) & \mathbf{x}(1) \end{array} \right] = \left[\begin{array}{cc} a_1 & -a_2^* \\ a_2 & a_1^* \\ a_3 & -a_4^* \\ a_4 & a_3^* \end{array} \right] \tag{5.7}$$

where $\mathbf{x}(0)$ and $\mathbf{x}(1)$ are the transmit signal vectors for the first and second symbol periods, respectively. There is not much analysis done on the theoretical capacity of D-STTD. In this chapter we present a general expression of the ergodic capacity of D-STTD.

Spatial multiplexing (SM) can be implemented as closed-loop or open-loop scheme. In closed-loop SM, the channel is assumed to be known at the transmitter and multiple parallel streams are transmitted over the eigenmodes of the channel. This scheme has been proved to be the capacity achieving strategy [33,132]. In open-loop SM, no channel state information is available at the transmitter and equal power is allocated across different transmit antennas. With $n_s = 1$, the transmit signal vector $\mathbf{x}$ in (5.1) is given by

$$\mathbf{x} = [a_1, a_2, ..., a_{N_t}]^T \tag{5.8}$$

where $a_m \in \mathbb{C}$ is the signal transmitted from the m^{th} antenna. At the receiver, both linear or non-linear filters [33] can be implemented to demodulate the parallel data streams transmitted through SM.

For MIMO systems employing open-loop SM with non-linear receivers the exact ergodic capacity was computed in integral form for single-sided correlated channels in [136–138] and for double-sided correlated channels in [114]. Tight upper bounds on the ergodic capacity are provided in closed-form in [104] for double-sided correlated MIMO channels and in [111, 139] for Rician spatially correlated channels. In this chapter, we propose a newly derived exact capacity expression of SM with linear receivers for single-sided correlated MIMO channels, to enable the analysis on the adaptive MIMO transmission scheme.

5.2 Optimal MIMO Capacity with Covariance Feedback

We first present the optimal capacity-achieving transmission strategy for the case of CDIT. The ergodic MIMO capacity is achieved using zero-mean Gaussian input signalling, and is given by the well-known formula

$$C = \max_{\mathbf{Q}:\mathrm{tr}(\mathbf{Q})=E_s} \mathcal{E}\left[\log_2\left|\mathbf{I}_{N_r} + \frac{\mathbf{HQH}^\dagger}{N_\mathrm{o}}\right|\right] \tag{5.9}$$

where the maximization is over the set of all power-constrained input covariance matrices $\mathbf{Q}$. Under the assumptions in Section 5.1.2 for zero-mean spatially correlated channels, the capacity achieving $\mathbf{Q}$ is given by [132]

$$\mathbf{Q}^{\mathrm{opt}} = \mathbf{U}_s \mathbf{\Lambda}_{\mathbf{Q}}^{\mathrm{opt}} \mathbf{U}_s^\dagger \tag{5.10}$$

where $\mathbf{\Lambda}_{\mathbf{Q}}^{\text{opt}}$ is the diagonal power allocation matrix

$$\mathbf{\Lambda}_{\mathbf{Q}}^{\text{opt}} = \arg \max_{\mathbf{\Lambda_Q}:\text{tr}\left(\mathbf{\Lambda_Q}\right)=E_s} \mathcal{E}\left[\log_2 \left| \mathbf{I}_{N_r} + \sum_{i=1}^{N_t} \frac{\lambda_{s,i}\lambda_i^{\mathbf{Q}}\mathbf{w}_i\mathbf{w}_i^{\dagger}}{N_{\text{o}}} \right|\right] \tag{5.11}$$

where

$$\mathbf{w}_i = \left[\sqrt{\lambda_{r,1}}w_{i,1},\, \ldots,\, \sqrt{\lambda_{r,N_r}}w_{i,N_r}\right]^T \tag{5.12}$$

and where $w_{i,j}$ are i.i.d. complex Gaussian random variables with zero mean and unit variance. Also, $\lambda_{s,i}$, $\lambda_{r,i}$ and $\lambda_i^{\mathbf{Q}}$ denote the i^{th} eigenvalue of $\mathbf{S}$, $\mathbf{R}$ and $\mathbf{Q}$ respectively. From (5.11) and (5.12) we see that the capacity achieving transmission scheme (defined by $\mathbf{Q}^{\text{opt}}$) depends explicitly on the eigenvalues of the transmit and receive correlation matrices. Unfortunately, for any given $\mathbf{S}$ and $\mathbf{R}$, the calculation of $\mathbf{\Lambda}_{\mathbf{Q}}^{\text{opt}}$ requires numerical optimization which is undesirable when designing practical systems due to its high computational complexity. The aim of the proposed adaptive method is to approximate the optimal capacity[2] by switching between low-complexity MIMO transmission schemes depending on the channel conditions.

5.3 Closed-form Capacity in Correlated Channels

We now present capacity expressions for the following transmission techniques: BF, OSTBC, D-STTD and SM. In the next section we compare these capacities with the optimal capacity in (5.9), and show that the ca-

[2]For the rest of the dissertation, we use the term "optimal capacity" to refer to the capacity with optimum signalling in MIMO systems with only channel covariance feedback, given by (5.10) and (5.11).

pacity obtained by adaptively switching across these low-complexity schemes approaches the optimal capacity.

5.3.1 Statistical Beamforming (BF)

In this subsection we derive a new closed-form exact capacity expression for statistical BF transmission in double-sided correlated channels. We also derive a tight upper bound, which will be particularly useful for examining the relative performance of BF and SM, as shown in the next section, and for identifying switching criteria for our practical adaptive algorithm. Note that BF capacity expressions were previously derived in [133] and [134, 135] for MISO and MIMO systems, respectively. These results, however, only considered MIMO channels with single-sided correlation.

Throughout this chapter, we assume that the BF receiver employs maximum ratio combining (MRC). The input covariance matrix for this system is given by

$$\mathbf{Q}^{\mathrm{BF}} = \mathbf{U}_s \mathbf{\Lambda}_{\mathrm{BF}} \mathbf{U}_s^{\dagger} \tag{5.13}$$

where

$$\mathbf{\Lambda}_{\mathrm{BF}} = \mathrm{diag}\left(E_s,\, 0,\, \ldots, 0\right) \tag{5.14}$$

Note that the first column of $\mathbf{U}_s$ is the eigenvector corresponding to the largest eigenvalue of $\mathbf{S}$, which we denote $\lambda_{s,\max}$. As mentioned in [132] and [130], statistical BF is in fact optimum (ie. $\mathbf{\Lambda}_{\mathrm{BF}} = \mathbf{\Lambda}_{\mathrm{opt}}$) in the low SNR regime.

Exact Ergodic Capacity

Using (5.13) and (5.2) in (5.9) gives

$$C_{\mathrm{BF}} = \mathcal{E}\left[\log_2\left|\mathbf{I}_{N_r} + \frac{1}{N_{\mathrm{o}}}\mathbf{R}^{1/2}\mathbf{Z}\mathbf{S}^{1/2}\mathbf{Q}^{\mathrm{BF}}\mathbf{S}^{\dagger/2}\mathbf{Z}^{\dagger}\mathbf{R}^{\dagger/2}\right|\right]. \tag{5.15}$$

Next, substituting the eigenvalue decompositions (5.4) and (5.13), yields

$$C_{\mathrm{BF}} = \mathcal{E}\left[\log_2\left|\mathbf{I}_{N_r} + \frac{1}{N_{\mathrm{o}}}\mathbf{U}_r\mathbf{\Lambda}_r^{1/2}\mathbf{U}_r^{\dagger}\mathbf{Z}\mathbf{U}_s\mathbf{\Lambda}_s^{1/2}\mathbf{U}_s^{\dagger}\mathbf{U}_s\mathbf{\Lambda}_{\mathrm{BF}}\mathbf{U}_s^{\dagger}\mathbf{U}_s\mathbf{\Lambda}_s^{1/2}\mathbf{U}_s^{\dagger}\mathbf{Z}^{\dagger}\mathbf{U}_r\mathbf{\Lambda}_r^{1/2}\mathbf{U}_r^{\dagger}\right|\right]. \tag{5.16}$$

Since $\mathbf{U}_s$ and $\mathbf{U}_r$ are unitary matrices, we get $\mathbf{U}_s^{\dagger}\mathbf{U}_s = \mathbf{I}_{N_t}$ and the matrices $\mathbf{U}_r^{\dagger}\mathbf{Z}$ and $\mathbf{Z}\mathbf{U}_s$ (respectively $\mathbf{U}_s^{\dagger}\mathbf{Z}^{\dagger}$ and $\mathbf{Z}^{\dagger}\mathbf{U}_r$) have the same distribution as $\mathbf{Z}$ (respectively $\mathbf{Z}^{\dagger}$), recognizing that $\mathbf{Z}$ is invariant under unitary transformation. With these properties, the expectation in (5.16) is statistically equivalent to

$$C_{\mathrm{BF}} = \mathcal{E}\left[\log_2\left|\mathbf{I}_{N_r} + \frac{1}{N_{\mathrm{o}}}\mathbf{\Lambda}_r^{1/2}\mathbf{Z}\mathbf{\Lambda}_s^{1/2}\mathbf{\Lambda}_{\mathrm{BF}}\mathbf{\Lambda}_s^{1/2}\mathbf{Z}^{\dagger}\mathbf{\Lambda}_r^{1/2}\right|\right]. \tag{5.17}$$

Substituting (5.14) into (5.17) we obtain

$$C_{\mathrm{BF}} = \mathcal{E}\left[\log_2\left|\mathbf{I}_{N_r} + \gamma_{\mathrm{o}}\lambda_{s,\max}\tilde{\mathbf{z}}\tilde{\mathbf{z}}^{\dagger}\right|\right] \tag{5.18}$$

where $\tilde{\mathbf{z}} = \left[\sqrt{\lambda_{r,1}}z_1, ..., \sqrt{\lambda_{r,N_r}}z_{N_r}\right]^T$, and the z_i's are i.i.d. zero mean unit variance complex Gaussian random variables. Note that z_i is the i-th entry of the first column of $\mathbf{Z}$. We now invoke the property

$$|\mathbf{I}_n + \mathbf{A}\mathbf{B}| = |\mathbf{I}_m + \mathbf{B}\mathbf{A}| \tag{5.19}$$

for arbitrary $\mathbf{A} \in \mathbb{C}^{n\times m}$ and $\mathbf{B} \in \mathbb{C}^{m\times n}$, to obtain

$$C_{\mathrm{BF}} = \mathcal{E}\left[\log_2\left(1 + \gamma_{\mathrm{o}}\lambda_{s,\max}\tilde{\mathbf{z}}^{\dagger}\tilde{\mathbf{z}}\right)\right] \tag{5.20}$$

$$= \mathcal{E}\left[\log_2\left(1 + \frac{\gamma_{\mathrm{o}}\lambda_{s,\max}\eta}{2}\right)\right] \tag{5.21}$$

where

$$\eta = \sum_{i=1}^{N_r} \lambda_{r,i} \varepsilon_i \tag{5.22}$$

where the ε_i's are i.i.d. exponentially-distributed random variables and, as such, η is a central quadratic form. Since the exponential distribution is a special case of the chi-squared distributed with *even* (ie. 2) degrees of freedom, we use a general result from [140] to represent the p.d.f. of η as

$$f(\eta) = \sum_{i=1}^{N_r} A_i \, p(\lambda_{r,i}\eta) \tag{5.23}$$

where $p(\cdot)$ denotes an exponential p.d.f., and

$$\begin{aligned} A_i &= \left(\prod_{j=1}^{N_r} (-2\lambda_{r,j})^{-1} \right) \left(\prod_{j=1, j\neq i}^{N_r} \left(\frac{1}{2\lambda_{r,i}} - \frac{1}{2\lambda_{r,j}} \right)^{-1} \right) \\ &= \prod_{j=1, j\neq i}^{N_r} \left(\frac{\lambda_{r,i}}{\lambda_{r,i} - \lambda_{r,j}} \right). \end{aligned} \tag{5.24}$$

Hence we have

$$f(\eta) = \sum_{i=1}^{N_r} \prod_{j=1, j\neq i}^{N_r} \left(\frac{\lambda_{r,i}}{\lambda_{r,i} - \lambda_{r,j}} \right) \frac{\exp\left(-\frac{\eta}{2\lambda_{r,i}} \right)}{2\lambda_{r,i}}. \tag{5.25}$$

The capacity is now given by

$$\begin{aligned} C_{\mathrm{BF}} &= \int_0^\infty \log_2 \left(1 + \frac{\gamma_{\mathrm{o}} \lambda_{s,\max} \eta}{2} \right) f(\eta) \, \mathrm{d}\eta \\ &= \sum_{i=1}^{N_r} \prod_{j=1, j\neq i}^{N_r} \left(\frac{\lambda_{r,i}}{\lambda_{r,i} - \lambda_{r,j}} \right) \int_0^\infty \log_2 \left(1 + \frac{\gamma_{\mathrm{o}} \lambda_{s,\max} \eta}{2} \right) \frac{\exp\left(-\frac{\eta}{2\lambda_{r,i}} \right)}{2\lambda_{r,i}} \mathrm{d}\eta. \end{aligned} \tag{5.26}$$

To evaluate the integrals in (5.36) we use the property [141]

$$\int_0^\infty \ln(1 + \beta x) \, \exp(-\mu x) \, \mathrm{d}x = -\frac{1}{\mu} \exp\left(\frac{\mu}{\beta} \right) \mathrm{Ei}\left(-\frac{\mu}{\beta} \right) \tag{5.27}$$

for $\mathrm{Re}(\mu) > 0$ and $-\pi < \arg\beta < \pi$, where $\mathrm{Ei}(\cdot)$ is the exponential integral. For Hermitian positive definite $\mathbf{R}$, the required conditions are met, and we use (5.37) to obtain

$$C_{\mathrm{BF}} = -\frac{1}{\ln 2}\sum_{i=1}^{N_r}\left(\prod_{j=1,j\neq i}^{N_r}\left(\frac{\lambda_{r,i}}{\lambda_{r,i}-\lambda_{r,j}}\right)\exp\left(\frac{1}{\gamma_{\mathrm{o}}\lambda_{s,\max}\lambda_{r,i}}\right)\mathrm{Ei}\left(-\frac{1}{\gamma_{\mathrm{o}}\lambda_{s,\max}\lambda_{r,i}}\right)\right). \tag{5.28}$$

We clearly see that the BF capacity depends explicitly on the long-term channel characteristics through the eigenvalues of the spatial correlation matrices.

Ergodic Capacity Upper Bound

We upper bound the BF capacity by applying Jensen's inequality to (5.20) as follows

$$C_{\mathrm{BF}} = \mathcal{E}\left[\log_2\left(1+\gamma_{\mathrm{o}}\lambda_{s,\max}\tilde{\mathbf{z}}^{\dagger}\tilde{\mathbf{z}}\right)\right] \tag{5.29}$$

$$\leq \log_2\left(1+\gamma_{\mathrm{o}}\lambda_{s,\max}\ \mathcal{E}\left[\tilde{\mathbf{z}}^{\dagger}\tilde{\mathbf{z}}\right]\right) \tag{5.30}$$

$$= \log_2\left(1+\gamma_{\mathrm{o}}\lambda_{s,\max}N_r\right). \tag{5.31}$$

Note that this upper bound applies for both single-sided and double-sided correlated Rayleigh MIMO channels.

Numerical Capacity Results

In Fig. 5.1 we present BF capacity curves based on the exact expression (5.28) and upper bound (5.31). The correlated MIMO channels are generated according to IEEE 802.11n Model D (NLOS) in [43]. For comparison, empirically-generated BF capacity curves, obtained using (5.9), are also shown.

We clearly see that, in all cases, the exact capacity curves match precisely with the empirical results, and the upper bound is tight.

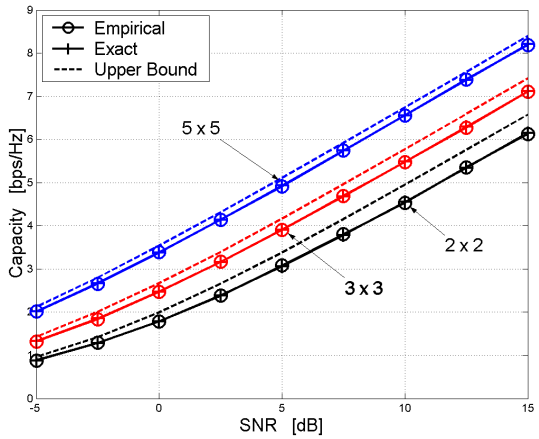

Figure 5.1: Empirical, exact and upper bound on the ergodic capacity of BF, in *double-sided* correlated channel Model D (NLOS), with different antenna configurations ($N_t \times N_r$).

5.3.2 Orthogonal Space-Time Block Codes (OSTBC)

In this subsection we derive a new closed-form expression and a much simpler upper bound expression for the capacity of OSTBC with a MRC receiver in spatially-correlated channels. These results will be used to investigate the relative performance of OSTBC with respect to SM transmission in various correlated channel scenarios.

The ergodic capacity of OSTBC can be expressed as

$$C_{\text{OSTBC}} = R_{\text{c}} \mathcal{E}\left[\log_2\left(1 + \frac{\gamma_{\text{o}}}{R_{\text{c}} N_t} ||\mathbf{H}||_{\text{F}}^2\right)\right] \tag{5.32}$$

where $\mathbf{H} = \mathbf{R}^{1/2}\mathbf{Z}\mathbf{S}^{1/2}$ is the double-sided correlated MIMO channel matrix, generated according to the stochastic model in Section 2.4.2. Moreover, $R_{\mathrm{c}} = n_s/N$ is the rate of the OSTBC, n_s is the number of symbols transmitted per block and N is the number of symbol periods per block. For double-sided spatially correlated channels we find

$$\begin{aligned} ||\mathbf{H}||_{\mathrm{F}}^2 &= \mathrm{vec}(\mathbf{H})^{\dagger}\mathrm{vec}(\mathbf{H}) \\ &= \mathrm{vec}(\mathbf{Z})^{\dagger}\mathbf{R}_H\mathrm{vec}(\mathbf{Z}) \\ &= \mathrm{vec}(\mathbf{Z})^{\dagger}\mathbf{U}_H\mathbf{\Lambda}_H\mathbf{U}_H\mathrm{vec}(\mathbf{Z}) \\ &= \mathrm{vec}(\mathbf{Z})^{\dagger}\mathbf{\Lambda}_H\mathrm{vec}(\mathbf{Z}) \\ &= \frac{1}{2}\sum_{i=1}^{r}\lambda_{H,i}\varepsilon_i \end{aligned} \tag{5.33}$$

where $\mathbf{R}_H$ is defined in (5.3), $r = \mathrm{rank}(\mathbf{R}_H)$, $\lambda_{H,i}$ are the non-zero diagonal entries of $\mathbf{\Lambda}_H$ in (5.4) and ε_i's are i.i.d. exponentially distributed random variables. Note that we invoke the property

$$\mathrm{vec}(\mathbf{H}) = (\mathbf{S}^{1/2} \otimes \mathbf{R}^{1/2})\mathrm{vec}(\mathbf{Z}) = \mathbf{R}_H^{1/2}\mathrm{vec}(\mathbf{Z}) \tag{5.34}$$

following from (5.3). We now define $\eta = \sum_{i=1}^{r}\lambda_{H,i}\varepsilon_i$, which is clearly a central quadratic form in Gaussian random vectors. Using a general result from [140], the p.d.f. of η is found to be

$$f(\eta) = \sum_{i=1}^{r}\left(\prod_{j=1,j\neq i}^{r}\frac{\lambda_{H,i}}{\lambda_{H,i}-\lambda_{H,j}}\right)\frac{\exp\left(-\frac{\eta}{2\lambda_{H,i}}\right)}{2\lambda_{H,i}}. \tag{5.35}$$

Using (5.32) and (5.35), the capacity is now given by

$$\begin{aligned} C_{\text{OSTBC}} &= R_{\text{c}} \int_0^{\infty} \log_2 \left(1 + \frac{\gamma_{\text{o}}}{2R_{\text{c}}N_t}\eta\right) f(\eta)\, \mathrm{d}\eta \\ &= R_{\text{c}} \sum_{i=1}^{r} \prod_{j=1, j\neq i}^{r} \left(\frac{\lambda_{H,i}}{\lambda_{H,i} - \lambda_{H,j}}\right) \\ &\quad \times \int_0^{\infty} \log_2 \left(1 + \frac{\gamma_{\text{o}}}{2R_{\text{c}}N_t}\eta\right) \frac{\exp\left(-\frac{\eta}{2\lambda_{H,i}}\right)}{2\lambda_{H,i}} \mathrm{d}\eta. \end{aligned} \tag{5.36}$$

To evaluate the integrals in (5.36) we use the property [141]

$$\int_0^{\infty} \ln(1+\beta x)\, \exp(-\mu x)\, \mathrm{d}x = -\frac{1}{\mu} \exp\left(\frac{\mu}{\beta}\right) \mathrm{Ei}\left(-\frac{\mu}{\beta}\right) \tag{5.37}$$

for $\mathrm{Re}(\mu) > 0$ and $-\pi < \arg\beta < \pi$, where $\mathrm{Ei}(\cdot)$ is the exponential integral. For Hermitian positive definite $\mathbf{Q}$, the required conditions are met, and we use (5.37) to obtain

$$\begin{aligned} C_{\text{OSTBC}} = -\frac{R_{\text{c}}}{\ln 2} \sum_{i=1}^{r} \Bigg(& \prod_{j=1, j\neq i}^{r} \left(\frac{\lambda_{H,i}}{\lambda_{H,i} - \lambda_{H,j}}\right) \\ & \times \exp\left(\frac{R_{\text{c}}N_t}{\gamma_{\text{o}}\lambda_{H,i}}\right) \mathrm{Ei}\left(-\frac{R_{\text{c}}N_t}{\gamma_{\text{o}}\lambda_{H,i}}\right)\Bigg). \end{aligned} \tag{5.38}$$

We clearly see that the OSTBC capacity depends explicitly on the long-term channel characteristics through the eigenvalues of the spatial correlation matrices.

We can derive a simpler expression which provides more insights by examining the upper bound on OSTBC capacity by applying Jensen's inequality to (5.32) to obtain

$$C_{\text{OSTBC}} \leq R_{\text{c}} \log_2 \left(1 + \frac{\gamma_{\text{o}}}{R_{\text{c}}} N_r\right). \tag{5.39}$$

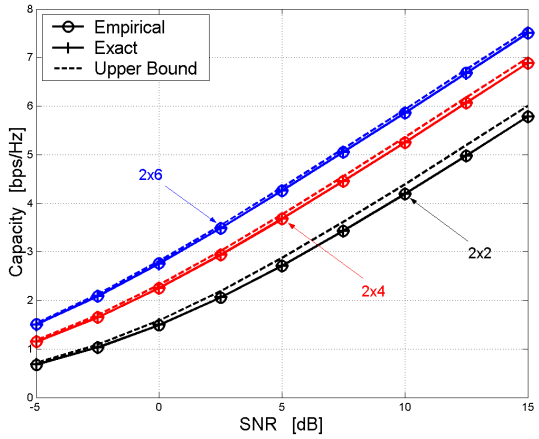

Figure 5.2: Empirical, exact and upper bound on the ergodic capacity of OSTBC for 2x2, 2x4 and 2x6 MIMO systems. The exponential model is used, with $\rho_{\text{tx}} = 0.5$ and $\rho_{\text{rx}} = 0.1$.

Note that this upper bound applies for both single-sided and double-sided correlated Rayleigh MIMO channels.

In Fig. 5.2 we compare the capacity expression (5.38) and upper bound (5.39) with empirically generated (simulated) capacity curves, in exponentially correlated channels with various antenna configurations. We see that the closed-form expression (5.38) is exact and the upper bound (5.39) is tight in all cases.

5.3.3 Double Space-Time Transmit Diversity (D-STTD)

In this subsection we consider the capacity of D-STTD. Although closed-form solutions are difficult to obtain even for the simplest case of i.i.d. Rayleigh MIMO channels (see below), here we formulate a new capacity expression suit-

able for efficient numerical evaluation.

Consider the D-STTD scheme proposed in [38] where $N_t = 4$ transmitted symbols (denoted $x_1, \ldots, x_4$ in the following) are encoded over 2 consecutive channel uses. Following the notations in [38], we define the stacked signal vectors

$$\bar{\mathbf{y}} \triangleq \begin{bmatrix} \bar{\mathbf{y}}_1 \\ \bar{\mathbf{y}}_2 \\ \vdots \\ \bar{\mathbf{y}}_{N_r} \end{bmatrix}, \quad \bar{\mathbf{x}} \triangleq \begin{bmatrix} a_1 \\ a_2^* \\ a_3 \\ a_4^* \end{bmatrix}, \quad \mathcal{H} \triangleq \begin{bmatrix} \mathcal{H}_{1,a} & \mathcal{H}_{1,b} \\ \mathcal{H}_{2,a} & \mathcal{H}_{2,b} \\ \vdots & \vdots \\ \mathcal{H}_{N_r,a} & \mathcal{H}_{N_r,b} \end{bmatrix} \tag{5.40}$$

with $\bar{\mathbf{y}}_m = [y_m(0),\ y_m^*(1)]^T$ and

$$\mathcal{H}_{m,a} \triangleq \begin{bmatrix} h_{m,1} & -h_{m,2} \\ h_{m,2}^* & h_{m,1}^* \end{bmatrix}, \quad \mathcal{H}_{m,b} \triangleq \begin{bmatrix} h_{m,3} & -h_{m,4} \\ h_{m,4}^* & h_{m,3}^* \end{bmatrix}. \tag{5.41}$$

where $h_{i,j}$ denotes the $(i,j)^{\text{th}}$ entry of the MIMO channel matrix $\mathbf{H}$ in (5.1). The equivalent input-output relation for D-STTD transmission can then be written as

$$\bar{\mathbf{y}} = \sqrt{\frac{E_s}{N_t}}\, \mathcal{H}\bar{\mathbf{x}} + \bar{\mathbf{n}} \tag{5.42}$$

where $\bar{\mathbf{n}}$ is the complex Gaussian noise. Note that the elements $\bar{\mathbf{y}}_m$ of the equivalent received vector $\bar{\mathbf{y}}$ contain the signals at the m^{th} receive antenna over the two consecutive symbol time-slots.

As for SM, we consider low-complexity linear receivers. The post-processing SNR for the k^{th} stream (ie. γ_k) in this case is then given by (5.47) and (5.48) for MMSE and ZF receivers, respectively, but with $\mathbf{H}$ replaced by the equivalent D-STTD channel matrix $\mathcal{H}$ in (5.40).

The D-STTD capacity with linear receivers can be derived based on an approach similar to [142] (where linear-dispersion codes were considered), and has the expression

$$C_{\mathrm{D-STTD}} = \mathcal{E}_{\gamma_k}\left[\frac{1}{2}\sum_{k=1}^{N_t}\log_2(1+\gamma_k)\right] \tag{5.43}$$

where the normalization factor of $\frac{1}{2}$ accounts for the two channel uses spanned by the D-STTD symbols. To evaluate (5.43), we require a closed-form expression for the p.d.f. of γ_k. Such an expression cannot be obtained even in the simplest i.i.d. Rayleigh case since $\mathcal{H}\mathcal{H}^\dagger$ does not follow a complex Wishart distribution. However the computation of (5.43) can be made efficient by observing that $\gamma_1 = \gamma_2$ and $\gamma_3 = \gamma_4$ and, moreover, that the random variables γ_k (for $k = 1, \ldots, 4$) are identically distributed (See Appendix A for proof). As such, (5.43) can be simplified as[3]

$$C_{\mathrm{D-STTD}} = 2\ \mathcal{E}_{\gamma}\left[\log_2\left(1+\gamma\right)\right]. \tag{5.44}$$

5.3.4 Spatial Multiplexing (SM)

In this subsection we derive a new closed-form exact capacity expression for SM with linear receivers. As for the BF case, we also derive a tight upper bound which will be useful for examining the relative performance of BF and SM in the next section, and for identifying switching criteria for our practical algorithm.

[3]Note that we drop the k subscript since the SNR statistics are identical for each stream.

For SM transmission, we assume equal-power allocation across the N_t transmit antennas, such that the input covariance matrix is given by

$$\mathbf{Q}^{\mathrm{SM}} = \frac{E_s}{N_t}\mathbf{I}_{N_t}. \tag{5.45}$$

In this case, the SM capacity has been investigated in the literature when high complexity maximum-likelihood (ML) receivers are employed. In particular, exact expressions and tight bounds are now available for both single-sided [137, 138] and double-sided [114] correlated Rayleigh MIMO channels. Recently, in [111, 139] capacity bounds were also derived for SM with ML recievers, for the more general case of double-sided correlated Rician MIMO channels. In [143], it was shown that, for systems with $N_t \leq N_r$, SM transmission with ML receivers is in fact optimum (ie. $\mathbf{Q}^{\mathrm{SM}} = \mathbf{Q}^{\mathrm{opt}}$) in the high SNR regime.

In contrast, closed-form capacity results for SM systems employing low complexity linear receivers do not appear to be available.

Exact Ergodic Capacity

For SM with linear receivers, the MIMO channel is effectively decoupled into N_t parallel streams, for which the capacity is given by [144]

$$C_{\mathrm{SM}} = \sum_{k=1}^{N_t} \mathcal{E}_{\gamma_k}\left[\log_2\left(1+\gamma_k\right)\right] \tag{5.46}$$

where γ_k is the conditional post-processing SNR for the k-th stream. We consider minimum mean-square error (MMSE) and zero-forcing (ZF) linear

receivers, for which γ_k is given by

$$\gamma_k = \frac{1}{\left[\left(\mathbf{I}_{N_t} + \frac{\gamma_o}{N_t}\mathbf{H}^\dagger\mathbf{H}\right)^{-1}\right]_{k,k}} - 1 \tag{5.47}$$

and

$$\gamma_k = \frac{\gamma_o}{N_t} \frac{1}{\left[(\mathbf{H}^\dagger\mathbf{H})^{-1}\right]_{k,k}} \tag{5.48}$$

respectively [145], where $[\cdot]_{k,k}$ denotes the k^{th} diagonal element.

The expectations in (5.46) cannot be computed in closed-form in general. To make our analysis mathematically tractable, for the remainder of this section we consider transmit correlated Rayleigh MIMO channels (ie. $\mathbf{R} = \mathbf{I}_{N_r}$) and ZF receivers[4]. Note, however, that MMSE receivers slightly outperform ZF receivers at low to moderate SNRs, and hence these receivers will be considered for our practical adaptive system proposed in Chapter 7. For the ZF case with transmit correlation, γ_k has p.d.f. [144]

$$f(\gamma_k) = \frac{N_t\left[\mathbf{S}^{-1}\right]_{k,k}}{\gamma_o} \frac{\exp\left(-\frac{\gamma_k N_t\left[\mathbf{S}^{-1}\right]_{k,k}}{\gamma_o}\right)}{\Gamma(N_r - N_t + 1)} \left(\frac{\gamma_k N_t\left[\mathbf{S}^{-1}\right]_{k,k}}{\gamma_o}\right)^{N_r - N_t} \tag{5.49}$$

Using (5.49), along with the identity [134]

$$\int_0^\infty \ln(1+by)\, y^{n-1} \exp(-cy)\, dy = \Gamma(n) \exp\left(\frac{c}{b}\right) \sum_{m=1}^{n} \frac{\Gamma\left(-n+m, \frac{c}{b}\right)}{c^m b^{n-m}} \tag{5.50}$$

where $\Gamma(\cdot,\cdot)$ is the incomplete gamma function, and the relation [146]

$$\left[\mathbf{S}^{-1}\right]_{k,k} = \frac{\left|\mathbf{S}^{kk}\right|}{|\mathbf{S}|} \tag{5.51}$$

[4]Note that the results also apply for channels with receive correlation when $N_r = N_t$. In this case, $\mathbf{S}$ is replaced by $\mathbf{R}$ in the final expression.

where $\mathbf{S}^{kk}$ corresponds to $\mathbf{S}$ with the k^{th} row and column removed, the SM capacity (5.46) can be evaluated as

$$C_{\text{SM}} = \sum_{k=1}^{N_t} \frac{\exp\left(\frac{\left|\mathbf{S}^{kk}\right|N_t}{|\mathbf{S}|\gamma_{\text{o}}}\right)}{\ln 2} \sum_{m=1}^{N_r-N_t+1} \frac{\Gamma\left(m-N_r+N_t-1, \frac{\left|\mathbf{S}^{kk}\right|N_t}{|\mathbf{S}|\gamma_{\text{o}}}\right)}{\left(\frac{\left|\mathbf{S}^{kk}\right|N_t}{|\mathbf{S}|\gamma_{\text{o}}}\right)^{m-N_r+N_t-1}}. \tag{5.52}$$

As for the BF case, we see that the SM capacity depends on the long-term channel characteristics through the eigenvalues of the spatial correlation matrix (i.e. through the determinant). This dependence is exploited by our practical adaptive algorithm presented in Chapter 7.

Ergodic Capacity Upper Bound

We upper bound the capacity of SM with ZF receivers by applying Jensen's inequality to (5.46) as follows

$$\begin{aligned} C_{\text{SM}} &= \sum_{k=1}^{N_t} \mathcal{E}_{\gamma_k}\left[\log_2\left(1+\gamma_k\right)\right] \\ &\leq \sum_{k=1}^{N_t} \log_2\left(1+\mathcal{E}_{\gamma_k}\left[\gamma_k\right]\right) \end{aligned} \tag{5.53}$$

We evaluate the expectations in (5.53) using the p.d.f. of γ_k given in (5.49), and the identity [141]

$$\int_0^\infty x^n \exp\left(-\mu x\right) \mathrm{d}x = n!\mu^{-n-1} \tag{5.54}$$

for $\Re e\left[\mu\right] > 0$, and simplify the resulting expression to obtain the capacity upper bound

$$C_{\text{SM}} \leq \sum_{k=1}^{N_t} \log_2\left(1+\frac{\left(N_r-N_t+1\right)|\mathbf{S}|\,\gamma_{\text{o}}}{N_t\,|\mathbf{S}^{kk}|}\right) \tag{5.55}$$

Numerical Capacity Results

Fig. 5.3 compares the exact capacity (5.52) and upper bound (5.55) for SM with ZF receivers against the empirical results obtained from Monte Carlo simulations. As for the BF case, we generated the MIMO channel according to Model D (NLOS) in [43], with single-sided correlation and different antenna configurations. Fig. 5.3 shows perfect match between the exact and empirical capacity and the upper bound is relatively tight, especially for high numbers of receive antennas.

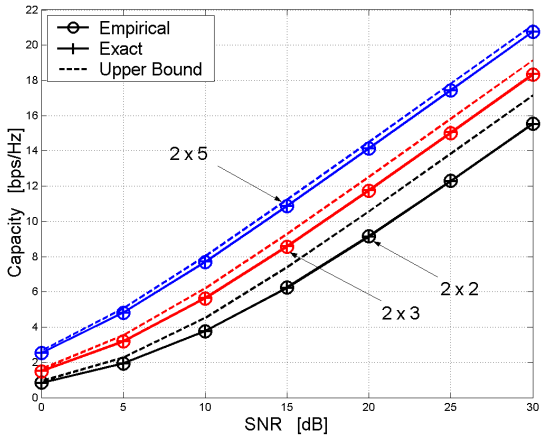

Figure 5.3: Empirical, exact and upper bound on the ergodic capacity of $(2 \times N_r)$ SM system with ZF receiver, in *single-sided* correlated channel Model D (NLOS).

5.4 Relative Capacity Investigation

In this section we invoke the results of the preceding section to investigate the relative capacity performance of BF, OSTBC, D-STTD and SM schemes in spatially-correlated Rayleigh MIMO channels.

5.4.1 Comparison of BF, D-STTD and SM Ergodic Capacities

In Fig. 5.4 we present ergodic capacity curves for BF, D-STTD with ZF receivers, and SM with ZF receivers, based on (5.28), (5.44) and (5.46), respectively. Results are shown for a 4×4 MIMO system, and the channel is generated according to IEEE 802.11n channel Model F (NLOS) [43]. The optimal capacity curve is also shown for comparison, which were generated by numerically solving the optimization problem (5.11). Note that, since the objective function in (5.11) is not convex, and because the problem is subject to an equality constraint, the maximization in (5.11) was performed using a constrained genetic algorithm [147].

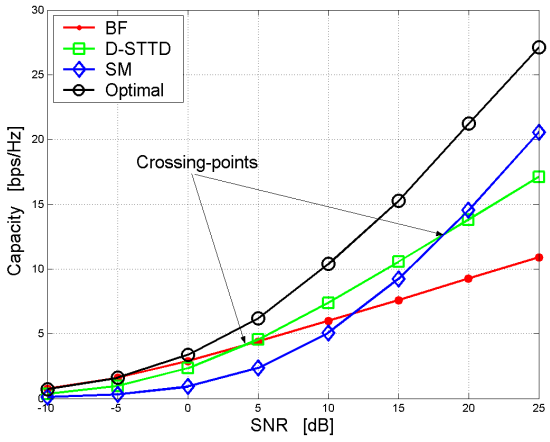

Figure 5.4: Mean capacity for BF, D-STTD (with ZF), SM (with ZF) and optimal transmission in the IEEE 802.11n channel Model F (NLOS).

As marked on the figure, we see that the capacity curves for the three low complexity schemes intersect, and that each scheme provides the highest

capacity, with respect to the others, for a certain range of SNRs. Specifically, we see that at low SNRs BF achieves the highest capacity of the low complexity schemes. In fact, for SNRs below -5 dB, BF achieves the optimal capacity, which agrees with previous results in [130, 132]. For moderate SNRs (i.e. between 4 dB and 18 dB), D-STTD achieves the highest capacity, whereas SM performs the best for high SNRs. We note that the capacity gap at large SNR between the SM and optimal capacity curves could be reduced by employing other higher-complexity receivers than linear receivers, such as successive interference cancelation (SIC). For our practical adaptive algorithm presented in Chapter 7 however, we consider low-complexity codes for which linear receivers are preferable over SIC receivers (for more details, see [148]).

These results demonstrate that there are significant capacity benefits to be gained (over fixed transmission) by adaptively switching between the low complexity transmission schemes we are considering, based on the operating SNR. As seen from the figure, such an adaptive scheme would perform closer to the optimal curve for all SNRs. Note, however, that although optimal transmission still yields a noticeable capacity advantage at many SNRs, this transmission approach is not suitable for practical MIMO systems due to the high computational complexity involved in solving the optimization problem (5.11). On the other hand, our low complexity adaptive MIMO approach is particularly suited to practical systems.

Fig. 5.5 shows capacity curves for the same low complexity transmission schemes as in Fig. 5.4, comparing different channel correlation scenarios. In

particular, IEEE 802.11a Models C and F [43] are considered, where Model C is characterized by a lower angle spread and a smaller number of scatterer clusters than Model F, resulting in higher levels of spatial correlation. We see that the relative capacity performance of the transmission schemes varies significantly, depending on the channel correlation scenario. Specifically, for Model C the crossing points of the BF/D-STTD and D-STTD/SM capacity curves (marked on the figure as CP1 and CP2, respectively) occur at SNRs *thresholds* of 8.2 dB and 31.8 dB, respectively. For Model F, these thresholds occur at the much lower SNRs of 3.7 dB and 18.4 dB respectively. These results suggest that a practical switching algorithm for the proposed low complexity adaptive MIMO approach (i.e. based on BF, D-STTD, and SM), should be designed to exploit *both* the average SNR and channel spatial correlation information.

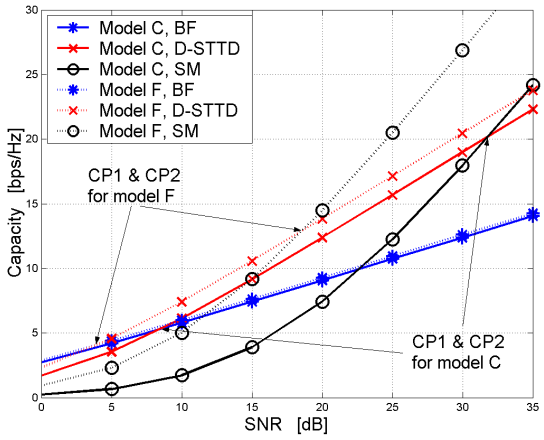

Figure 5.5: Mean capacity for BF, D-STTD (with ZF), SM (with ZF) in the IEEE 802.11n channel Models C and F (NLOS). CP1: crossing-point BF versus D-STTD; CP2: crossing-point D-STTD versus SM.

In the following subsection, we gain further insights into the key parameters affecting the relative capacity performance, by deriving closed-form theoretical expressions for the capacity crossing-points in some representative scenarios, for the case of BF and SM transmission.

5.4.2 Capacity Crossing-Points between BF and SM

Our crossing-point investigation is based on the tight upper bounds (5.31) and (5.55), for BF and SM transmission respectively. To derive the theoretical crossing points it is useful to manipulate the SM capacity (5.55) into a slightly different form. We start by writing

$$\begin{aligned} C_{\mathrm{SM}} &\leq \log_2 \left(\prod_{k=1}^{N_t} \left(1 + \frac{(N_r - N_t + 1)\,|\mathbf{S}|\,\gamma_{\mathrm{o}}}{N_t\,|\mathbf{S}^{kk}|} \right) \right) \\ &= \log_2 \left| \mathbf{I}_{N_t} + \mathrm{diag} \left(\frac{(N_r - N_t + 1)\,|\mathbf{S}|\,\gamma_{\mathrm{o}}}{N_t\,|\mathbf{S}^{kk}|} \right) \right| \end{aligned} \tag{5.56}$$

Now, using a determinant expansion from [149, pp. 88], we express the SM capacity as a polynomial in γ_{o} as follows

$$\begin{aligned} C_{\mathrm{SM}} &\leq \log_2 \left(1 + \sum_{k=1}^{N_t} \gamma_{\mathrm{o}}^k \left(\frac{N_r - N_t + 1}{N_t} \right)^k \mathrm{tr}_k \left(\mathrm{diag} \left(\frac{|\mathbf{S}|}{|\mathbf{S}^{11}|}, \ldots, \frac{|\mathbf{S}|}{|\mathbf{S}^{N_t N_t}|} \right) \right) \right) \\ &= \log_2 \left(1 + \sum_{k=1}^{N_t} \gamma_{\mathrm{o}}^k \left(\frac{N_r - N_t + 1}{N_t} |\mathbf{S}| \right)^k \mathrm{tr}_k \left(\mathbf{A} \right) \right) \end{aligned} \tag{5.57}$$

where

$$\mathbf{A} = \mathrm{diag} \left(\frac{1}{|\mathbf{S}^{11}|}, \ldots, \frac{1}{|\mathbf{S}^{N_t N_t}|} \right). \tag{5.58}$$

and where $\mathrm{tr}_k(\cdot)$ denotes the k^{th} elementary symmetric function (e.s.f.), defined as [146, 150]

$$\mathrm{tr}_k(\mathbf{X}) = \sum_{\{\underline{\alpha}\}} \prod_{i=1}^{k} \lambda_{x,\alpha_i} = \sum_{\{\underline{\alpha}\}} \left|\mathbf{X}_{\underline{\alpha}}^{\underline{\alpha}}\right| \tag{5.59}$$

for arbitrary Hermitian positive-definite $\mathbf{X} \in \mathbb{C}^{n\times n}$. In (6.47), the sum is over all ordered $\underline{\alpha} = \{\alpha_1, \ldots, \alpha_k\} \subseteq \{1, \ldots, n\}$, $\lambda_{x,i}$ denotes the i^{th} eigenvalue of $\mathbf{X}$, and $\mathbf{X}_{\underline{\alpha}}^{\underline{\alpha}}$ is the $k \times k$ principle submatrix of $\mathbf{X}$ formed by taking only the rows and columns indexed by $\underline{\alpha}$.

Comparing (5.57) with the BF capacity bound in (5.31) we find that the SNR threshold γ_{CP} corresponding to the capacity crossing-point is given by the positive solution to the polynomial equation

$$\sum_{k=1}^{N_t} \gamma_{\text{CP}}^{k-1} \left(\frac{N_r - N_t + 1}{N_t}|\mathbf{S}|\right)^k \mathrm{tr}_k\left(\mathbf{A}\right) - N_r\lambda_{s,\max} = 0. \tag{5.60}$$

We now present closed-form expressions for γ_{CP} for two special cases, in order to gain further insight.

Case: $2 \times N_r$

In this case, from (5.58) and (6.47) we have $\mathrm{tr}_1\left(\mathbf{A}\right) = 2$ and $\mathrm{tr}_2\left(\mathbf{A}\right) = 1$, and it is easily shown that the solution to (5.65) is given by

$$\gamma_{\text{CP}} = \frac{4\left(N_r\lambda_{s,\max} - (N_r - 1)|\mathbf{S}|\right)}{\left(N_r - 1\right)^2|\mathbf{S}|^2}. \tag{5.61}$$

This result shows that the SNR thresholds, defining the relative performance of the low complexity transmission schemes, depend explicitly on the *eigenvalues* of the transmit correlation matrix (i.e. through the determinant). This

information is exploited in our proposed practical switching algorithm, as detailed in the following section. It is also interesting to observe that the capacity crossing-point varies inversely to the number of receive antennas, indicating that the relative capacity improvement due to the increased receive diversity is greater for SM transmission than for BF.

For the special case $N_r = 2$, the capacity crossing-point further simplifies as follows

$$\gamma_{\mathrm{CP}} = \frac{4}{|\mathbf{S}|}\left(\frac{2}{\lambda_{s,\min}} - 1\right). \tag{5.62}$$

Case: $3 \times N_r$

In this case, (5.65) reduces to a simple quadratic equation. Solving this, and simplifying using (5.58) and (6.47), we obtain

$$\gamma_{\mathrm{CP}} = \frac{\sqrt{\mathrm{tr}_2\left(\mathbf{A}\right)^2 - 4|\mathbf{A}|\left(\mathrm{tr}(\mathbf{A}) - \frac{3\lambda_{s,\max}N_r}{(N_r-2)|\mathbf{S}|}\right)} - \mathrm{tr}_2(\mathbf{A})}{\frac{2}{3}(N_r-2)|\mathbf{A}||\mathbf{S}|} \tag{5.63}$$

For the special case $N_r = 3$, this result further simplifies to

$$\gamma_{\mathrm{CP}} = \frac{\sqrt{\mathrm{tr}_2\left(\mathbf{A}\right)^2 - 4|\mathbf{A}|\left(\mathrm{tr}(\mathbf{A}) - \frac{9\lambda_{s,\max}}{|\mathbf{S}|}\right)} - \mathrm{tr}_2(\mathbf{A})}{\frac{2}{3}|\mathbf{A}||\mathbf{S}|}. \tag{5.64}$$

Again we see a dependence on the eigenvalues of the transmit spatial correlation matrix.

Numerical Crossing-Point Results

Fig. 5.6 shows the SNR threshold (5.61) as a function of the angular spread (AS), for $N_t = 2$ and different numbers of receive antennas. The correlated MIMO channel is generated assuming a single scatterer cluster around

the transmitter, with a broadside mean angle of departure (with respect to the antenna array).

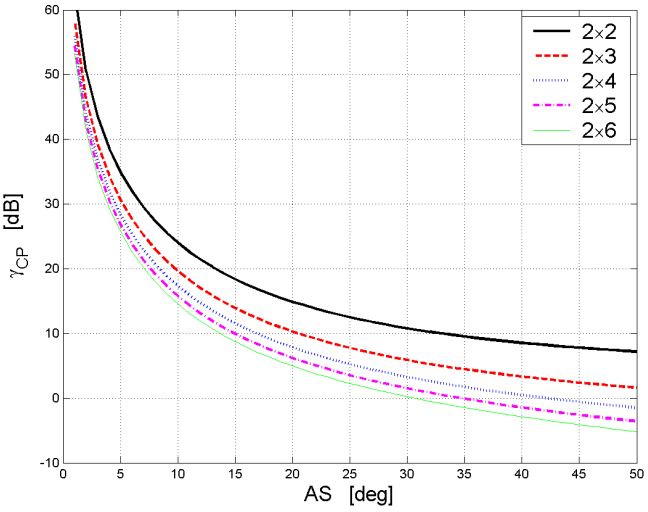

Figure 5.6: Crossing-points for a MIMO(N_r,2) system as a function of the angular spread (AS) and number of receive antennas (N_r). Single-sided correlated channel with single cluster and mean angle of departure at 0^o (broadside direction).

We see that the SNR threshold varies inversely to the angular spread. This is due to the fact that increasing the angular spread reduces the level of spatial correlation (or equivalently, increases the spatial selectivity), in which case the maximum eigenvalue of the transmit correlation matrix $\lambda_{s,\max}$ also reduces, thereby decreasing γ_{CP} consistently with (5.61). The figure also shows that the SNR threshold becomes very large for AS below 10 degrees, for all antenna configurations. This indicates that SM transmission is particularly sensitive to high levels of spatial correlation.

5.4.3 Capacity Crossing-Points between OSTBC and SM

Comparing the OSTBC capacity bound in (5.39) with the SM bound in (5.55) we find that there exists a crossing point of the capacity curves at an SNR threshold γ_{CP}, which corresponds to the positive solution to the polynomial equation

$$\sum_{k=1}^{N_t} \gamma_{\mathrm{CP}}^k \left(\frac{N_r - N_t + 1}{N_t} |\mathbf{S}| \right)^k \mathrm{tr}_k\left(\mathbf{A}\right) + 1 = \left(\gamma_{\mathrm{o}} \frac{N_r}{R_{\mathrm{c}}} + 1 \right)^{R_{\mathrm{c}}} \tag{5.65}$$

where $\mathbf{A} = \mathrm{diag}\left(1/|\mathbf{S}^{11}|, \ldots, 1/|\mathbf{S}^{N_t N_t}|\right)$, $\mathrm{tr}_k(\cdot)$ denotes the k^{th} elementary symmetric function and $\mathbf{S}^{kk}$ corresponds to $\mathbf{S}$ with the k^{th} row and column removed.

To gain further insight, we consider the special case of $N_t = 2$ and $N_r = 2$. By definition $\mathrm{tr}_1\left(\mathbf{A}\right) = 2$ and $\mathrm{tr}_2\left(\mathbf{A}\right) = 1$, and it is easily shown that the solution to (5.65) is given by

$$\gamma_{\mathrm{CP}} = \frac{4}{|\mathbf{S}|} \left(\frac{2}{|\mathbf{S}|} - 1 \right) \tag{5.66}$$

where we assumed $R_{\mathrm{c}} = 1$ for the Alamouti code. Noting that $|\mathbf{S}|$ is a decreasing function of the channel correlation, we see that γ_{CP}, defining the relative performance of OSTBC and SM, varies monotonically with the correlation, indicating that OSTBC is more resilient to correlation than SM.

Fig. 5.7 shows OSTBC capacity curves based on (5.39), and the SM-ZF capacity (derived in [151]), in low and high correlation scenarios. As expected, we see a crossing point between the respective OSTBC and SM curves, which moves significantly to the right (i.e. by approximately 16 dB) as the spatial

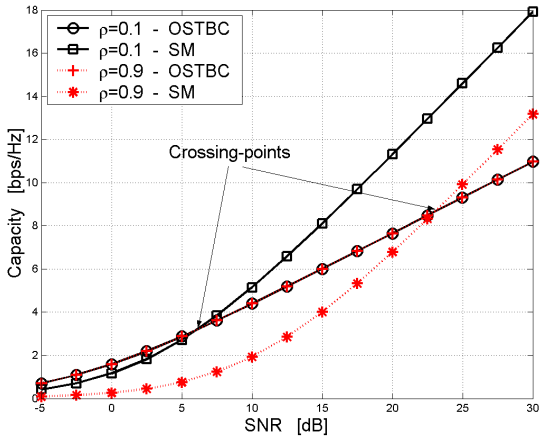

Figure 5.7: Capacity crossing-points of OSTBC and SM for MIMO 2x2 systems, as a function of the transmit spatial correlation. The channel is single-sided correlated and the exponential model is used, with $\rho_{\text{tx}} = 0.1$ and $\rho_{\text{tx}} = 0.9$.

correlation increases. This result suggests that practical adaptive switching strategies (such as the method proposed in Chapter 7) should be designed to take into account not only the average SNR, but also the spatial correlation information.

Chapter 6

BER Analysis of Adaptive MIMO-BICM Systems

In designs of adaptive MIMO systems, it is required to simulate the bit error rate (BER) performance of different transmission techniques to characterize optimal criteria to switch between schemes. These simulations may be very computationally expensive, since the BER performance has to be evaluated in a variety of propagation scenarios. Moreover, practical adaptive systems employ combinations of modulation and coding schemes (MCS) to enable transmissions over the wireless link. Simulating the BER for different combinations of MCSs and MIMO schemes becomes prohibitive in practical designs, where the BER has to be evaluated with restrictive targets (i.e., 10^{-6}). One solution is to analytically compute closed-form BER expressions for bit-interleaved coded modulation (BICM) MIMO systems. This chapter first provides an overview on adaptive MIMO-BICM systems and the low-complexity schemes used in the adaptive algorithm. Then, closed-form BER expressions are derived for BF, OSTBC and SM transmission techniques.

6.1 Introduction

This section presents some background on adaptive MIMO-BICM systems. Then describes the system model and architecture as well as the low-complexity MIMO schemes.

6.1.1 Background on Adaptive MIMO-BICM Systems

In this chapter we extend the scope of investigation on adaptive MIMO systems in [152–154] by considering coded modulation, over channels with correlation between antennas at *both* the transmitter and receiver. We focus on maximizing the data rate for a given target error performance. For this broader, more practical class of systems, we propose a novel adaptive MIMO transmission algorithm based on deriving closed-form bit error rate (BER) expressions.

We consider three simple MIMO schemes: statistical beamforming (SB), orthogonal space-time block codes (OSTBC) and spatial multiplexing with zero-forcing (ZF) receiver. SB requires only covariance feedback information, while OSTBC and ZF are open-loop schemes with low complexity linear receivers. Our proposal is to adaptively switch between these three schemes based on the channel conditions. Of course, it is common to adapt MIMO transmission systems between a set of coding and modulation modes based on SNR, e.g. as discussed in [127]. The key idea of our algorithm is to also introduce adaptive switching between SB or OSTBC in high correlation conditions, and spatial multiplexing in low correlation conditions. This switching

method improves the performance, and requires minimal feedback information since it relies on only two channel statistics: the average SNR and the spatial correlation.

An additional important component of our adaptive algorithm is that the switching criteria is based on closed-form BER expressions, which we derive in this chapter. The only previous adaptive schemes for channels with both transmit and receive correlation, of which we know, are limited by the fact that the mode selection criterion is based on empirically-generated lookup tables constructed from a small set of typical channel scenarios [2, 151], or are based on loose SNR approximations [154]; thus making the switching inaccurate. We note that it may also be possible to get closed-form results for other more complicated receivers structures, such as the minimum mean-square error (MMSE) or successive interference cancelation receivers; although this is beyond the scope of this chapter. In the particular case of the MMSE receiver, the performance is known to be close to ZF, and hence the switching algorithm we develop here could be applied directly with a small approximation error.

The coding we consider in this chapter is bit-interleaved coded modulation (BICM), which is common in practical wireless systems (e.g. IEEE 802.11a WLANs, and proposed for IEEE 802.11n), and is ideally suited to adaptive transmission. BICM is easily adapted to changing channel conditions by simply puncturing the mother encoder and changing to a corresponding modulation format. Recently, BICM schemes have been extended to uncorrelated MIMO scenarios, and been shown to perform favorably with practical

ZF receivers [155, 156].

To design the switching criterion, we derive new closed-form expressions for the BER of BICM coupled with SB, OSTBC an ZF (hereafter denoted BICM-SB, BICM-OSTBC and BICM-ZF, respectively) in transmit and receive spatially-correlated channels. The results are based on the typical BICM assumption of ideal interleaving. This assumption is valid in channels with sufficient time variation or frequency selectivity. We make use of a saddlepoint approach, originally proposed in [157, 158] for the single-input single-output (SISO) BICM case, and derive closed-form expressions for the error probabilities which are tight. The expressions can be used to calculate achievable throughputs for given combinations of coding and modulation. These results are used to identify and examine performance tradeoffs for the three MIMO transmission schemes.

6.1.2 System Model and Architecture

Consider a narrowband MIMO system with N_t and N_r transmit and receive antennas respectively. Throughout this chapter we assume $N_t \leq N_r$, to facilitate low complexity BICM-ZF transmission (see below). For each channel use the received signal vector is given by (5.1) in Section 5.1.2. The channel is decomposed according to the common *Kronecker* structure [111, 114, 132] as in (5.2) in Section 5.1.2. We assume that $\mathbf{R}$ and $\mathbf{S}$ are Hermitian positive-definite matrices containing unit diagonal entries. Moreover, we assume that the eigenvector $\mathbf{u}_{s,\max}$ corresponding to the maximum eigenvalue of $\mathbf{S}$ is known

perfectly at the transmitter (this is to facilitate SB, see below). With this model, the average SNR per receive antenna is $N_t\gamma$.

Note that all analytical results presented in this chapter apply equally to any particular correlation model which can be expressed in the form (5.2). For the numerical studies we consider the exponential correlation model at the transmitter and receiver (e.g. as in [114]), given by (2.15) in Section 2.4.2. We choose this simple exponential correlation model (for the numerical studies) to illustrate clearly the impact of spatial correlation on the relative performance of the SB, OSTBC and ZF schemes. These results will be also validated in more realistic deterministic channel models described in Section 2.4.1.

The MIMO system architecture we analyze is presented in Fig. 6.1. The encoder, interleaver (assumed ideal), and constellation mapper, form the bit-interleaved coded modulation (BICM) section of the transmitter. The BICM system operates according to one of a finite set of modes, with each mode comprising a particular combination of encoder rate and modulation format. The encoder rate R is varied by puncturing a mother binary convolutional encoder. The modulation formats are Gray-labeled 2^M-ary PSK or QAM constellations, denoted $\mathcal{A}$, of unit average energy. Following modulation, the symbols are mapped to transmit signal vectors $\mathbf{x}$, according to the particular MIMO transmission scheme, as discussed in the following section.

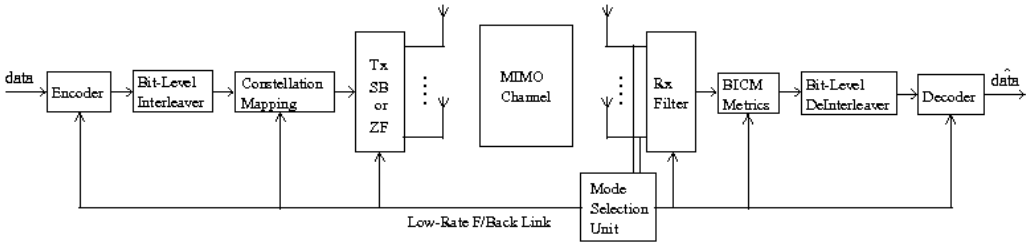

Figure 6.1: MIMO-BICM system architecture.

6.1.3 Low Complexity MIMO Transmission Schemes

This section details SB and OSTBC which we will show is suited to channels with high correlation or low SNR, and a ZF scheme which we show performs best in uncorrelated channels and high SNR.

Statistical Beamforming

For the SB scheme, a single modulated symbol is transmitted from all the antennas, with an appropriate complex weighting, during each channel use. For a modulated symbol $a \in \mathcal{A}$, the transmission vector $\mathbf{x}$ is formed as follows

$$\mathbf{x} = \mathbf{u}_{s,\max} a. \tag{6.1}$$

The spectral efficiency of BICM-SB, in bits/s/Hz, is therefore given by

$$S_{\text{BICM}-\text{SB}} = RM. \tag{6.2}$$

Orthogonal Space-Time Block Code

OSTBC transmits parallel streams over n_s consecutive symbol periods and the symbols are encoded across different antennas. The model of the transmit signal matrix of OSTBC was presented in Section 5.1.3.

Zero-Forcing

For the ZF scheme, N_t modulated symbols are transmitted, one per antenna, during each channel use. The spectral efficiency of BICM-ZF, in bits/s/Hz, is therefore given by

$$S_{\text{BICM}-\text{ZF}} = N_t RM. \tag{6.3}$$

Clearly, for a given mode (R and M), $S_{\text{BICM}-\text{ZF}}$ is larger than $S_{\text{BICM}-\text{SB}}$ by a factor of N_t.

6.1.4 Low Complexity MIMO-BICM Receivers

Statistical Beamforming

For the SB scheme, maximum ratio combining (MRC) is applied to the receive signal vector to yield

$$\begin{aligned} z = \mathbf{f}^{\dagger}\mathbf{y} &= \sqrt{\gamma}\,\mathbf{f}^{\dagger}\left(\mathbf{H}\mathbf{u}_{\text{s,max}}\,a + \mathbf{n}\right) \\ &= \sqrt{\gamma}\,\|\mathbf{f}\|^2 a + \underline{n} \end{aligned} \tag{6.4}$$

where $\mathbf{f} = \mathbf{H}\mathbf{u}_{s,\max}$ and $\underline{n} = \mathbf{f}^{\dagger}\mathbf{n} \sim \mathcal{CN}\left(0, \|\mathbf{f}\|^2\right)$. The BICM log-likelihood metrics for each of the bits i $(= 1, \ldots, M)$ corresponding to the modulated symbol a are calculated from z using

$$\mathcal{L}_i = \ln \frac{\sum_{\tilde{a}\in\mathcal{A}_1^i} p\left(z|\tilde{a}, \mathbf{f}\right)}{\sum_{\tilde{a}\in\mathcal{A}_0^i} p\left(z|\tilde{a}, \mathbf{f}\right)} \tag{6.5}$$

where

$$p\left(z|\tilde{a},\mathbf{f}\right)=\frac{1}{\pi\|\mathbf{f}\|^{2}}\exp\left(-\frac{|z-\sqrt{\gamma}\,\|\mathbf{f}\|^{2}\tilde{a}|^{2}}{\|\mathbf{f}\|^{2}}\right) \tag{6.6}$$

and where $\mathcal{A}_0^i, \mathcal{A}_1^i$ are the signal subsets within $\mathcal{A}$ with i^{th} bit equal to 0 and 1 respectively. These metrics are deinterleaved, and decoded using a conventional soft-decision Viterbi algorithm.

Orthogonal Space-Time Block Code

For OSTBC transmission with a maximum-ratio combining (MRC) receiver, we have the following equivalent input-output extension to (5.1) as in [142]

$$\mathbf{z}=\sqrt{\gamma}\|\mathbf{H}\|_{F}^{2}\mathbf{x}+\underline{\mathbf{n}} \tag{6.7}$$

where $\underline{\mathbf{n}}\sim\mathcal{CN}\left(\mathbf{0}_{n_s\times 1},\|\mathbf{H}\|_{F}^{2}\mathbf{I}_{n_s}\right)$.

From (6.7), clearly the k^{th} element of $\mathbf{z}\in\mathbb{C}^{n_s\times 1}$ corresponds to the output from a fading AWGN scalar channel, where the input is the k^{th} element of $\mathbf{a}$. For the k^{th} modulated symbol, a_k, the BICM log-likelihood metrics are then calculated for the corresponding bits $i\ (=1,\ldots,M)$ according to [156]

$$\mathcal{L}_{k,i}=\ln\frac{\sum_{\tilde{a}\in\mathcal{A}_1^i}p\left(z_k|\tilde{a},\mathbf{H}\right)}{\sum_{\tilde{a}\in\mathcal{A}_0^i}p\left(z_k|\tilde{a},\mathbf{H}\right)} \tag{6.8}$$

where $\mathcal{A}_0^i$ and $\mathcal{A}_1^i$ denote the subsets of the (scalar) transmit constellation $\mathcal{A}$ with i^{th} bit equal to 0 and 1 respectively, z_k is the k^{th} element of $\mathbf{z}$, and

$$p\left(z_k|\tilde{a},\mathbf{H}\right)=\frac{1}{\pi\|\mathbf{H}\|_{F}^{2}}\exp\left(-\frac{|z_k-\sqrt{\gamma}\|\mathbf{H}\|_{F}^{2}\,\tilde{a}|^{2}}{\|\mathbf{H}\|_{F}^{2}}\right). \tag{6.9}$$

These metrics are deinterleaved, and decoded using a soft-decision Viterbi algorithm.

Zero-Forcing

For the ZF scheme, the initial filtering step at the receiver is

$$\mathbf{z} \;=\; \mathbf{W}\,\mathbf{y} \;=\; \sqrt{\gamma}\mathbf{x} + \underline{\mathbf{n}} \tag{6.10}$$

where $\mathbf{W} = \left(\mathbf{H}^{\dagger}\mathbf{H}\right)^{-1}\mathbf{H}^{\dagger}$ and $\underline{\mathbf{n}} = \mathbf{W}\,\mathbf{n} \sim \mathcal{CN}\left(\mathbf{0}_{N_t\times 1}, \mathbf{W}\mathbf{W}^{\dagger}\right)$. Clearly, the k^{th} element of $\mathbf{z}$ corresponds to the output from a colored Gaussian noise channel, where the input is the k^{th} element of $\mathbf{x}$. For the k^{th} modulated symbol, a_k, the BICM log-likelihood metrics are then calculated for the corresponding bits i $(= 1, \ldots, M)$ according to [155, 156]

$$\mathcal{L}_{k,i} = \ln \frac{\sum_{\tilde{a}\in\mathcal{A}_1^i} p\left(z_k|\tilde{a}, \mathbf{w}_k\right)}{\sum_{\tilde{a}\in\mathcal{A}_0^i} p\left(z_k|\tilde{a}, \mathbf{w}_k\right)} \tag{6.11}$$

where z_k is the k^{th} element of $\mathbf{z}$, $\mathbf{w}_k$ is the k^{th} row vector of $\mathbf{W}$, and

$$p\left(z_k|\tilde{a}, \mathbf{w}_k\right) = \frac{1}{\pi\|\mathbf{w}_k\|^2}\exp\left(-\frac{|z_k - \sqrt{\gamma}\tilde{a}|^2}{\|\mathbf{w}_k\|^2}\right). \tag{6.12}$$

These metrics are deinterleaved, and decoded using a soft-decision Viterbi algorithm.

6.2 Link-Level Capacity of MIMO-BICM

In this section we calculate and compare the BICM-SB and BICM-ZF link-level capacities (LLC) in spatially-correlated Rayleigh MIMO channels.

Assuming uniformly-distributed inputs and ideal interleaving, the LLC is calculated by summing the mutual information (MI) for each equivalent BICM subchannel (i.e. as in [156, 159])[1].

6.2.1 Statistical Beamforming (BICM-SB)

Using a technique for the LLC of SISO-BICM from [159], we obtain the LLC of BICM-SB as

$$C_{\text{BICM_SB}} = M - \sum_{i=1}^{M} E_{u,z,\mathbf{f}}\left[\log_2 \frac{\sum_{\tilde{a}\in\mathcal{A}} p(z|\tilde{a},\mathbf{f})}{\sum_{\tilde{a}\in\mathcal{A}_u^i} p(z|\tilde{a},\mathbf{f})}\right] \tag{6.13}$$

where u is an equivalent-channel binary input taking values 0 and 1 with equal probability, independent of z and $\mathbf{f}$. Substituting the conditional p.d.f. (6.6), and using (6.4), we average over u, and the uniformly-distributed channel inputs $a \in \mathcal{A}_u^i$ to obtain

$$C_{\text{BICM_SB}} = M - \frac{1}{2^M}\sum_{i=1}^{M}\sum_{u=0}^{1}\sum_{a\in\mathcal{A}_u^i} E_{n,\mathbf{f}}\left[\log_2 \frac{\sum_{\tilde{a}\in\mathcal{A}} \exp\left(-\frac{|\sqrt{\gamma}\|\mathbf{f}\|^2(a-\tilde{a})+n|^2}{\|\mathbf{f}\|^2}\right)}{\sum_{\tilde{a}\in\mathcal{A}_u^i} \exp\left(-\frac{|\sqrt{\gamma}\|\mathbf{f}\|^2(a-\tilde{a})+n|^2}{\|\mathbf{f}\|^2}\right)}\right]. \tag{6.14}$$

In Section 6.4 we present a closed-form expression for the p.d.f. of $\|\mathbf{f}\|^2$. Using this p.d.f. and the usual Gaussian p.d.f. for n, the expectations in (6.14) can be efficiently computed using a combination of Gauss-Laguerre and Gauss-Hermite quadratures, tabulated in [161].

[1] For general MIMO capacity analysis (Gaussian inputs), see [32, 111, 132, 160].

6.2.2 Zero-Forcing Receivers (BICM-ZF)

We have previously derived the LLC for BICM-ZF in i.i.d. Rayleigh channels as [156]

$$C_{\text{BICM_ZF}} = mN_t - \sum_{k=1}^{N_t}\sum_{i=1}^{M} E_{u,z_k,\mathbf{w}_k}\left[\log_2 \frac{\sum_{\tilde{a}\in\mathcal{A}} p(z_k|\tilde{a},\mathbf{w}_k)}{\sum_{\tilde{a}\in\mathcal{A}_u^i} p(z_k|\tilde{a},\mathbf{w}_k)}\right] \tag{6.15}$$

where u is distributed as it was in (6.13). We note that this expression applies equally to spatially-correlated channels, under the assumption of ideal interleaving. Substituting the conditional p.d.f. (6.12) into (6.15), using (6.10), and averaging over u and $a \in \mathcal{A}_u^i$ we obtain

$$C_{\text{BICM_ZF}} = MN_t - \frac{1}{2^M}\sum_{k=1}^{N_t}\sum_{i=1}^{M}\sum_{u=0}^{1}\sum_{a\in\mathcal{A}_u^i} E_{\underline{n}_k,\mathbf{w}_k}\left[\log_2 \frac{\sum_{\tilde{a}\in\mathcal{A}} \exp\left(-\frac{|\sqrt{\gamma}(a-\tilde{a})+\underline{n}_k|^2}{\|\mathbf{w}_k\|^2}\right)}{\sum_{\tilde{a}\in\mathcal{A}_u^i} \exp\left(-\frac{|\sqrt{\gamma}(a-\tilde{a})+\underline{n}_k|^2}{\|\mathbf{w}_k\|^2}\right)}\right]. \tag{6.16}$$

For transmit correlated channels, the p.d.f. of $\|\mathbf{w}_k\|^{-2}$ is known in closed-form [144], and the expectations in (6.16) can be computed efficiently using Gauss-Laguerre and Gauss-Hermite quadratures. For channels with both transmit and receive correlation, such closed-form p.d.f.s are not available, and the expectations must be evaluated through simulation.

6.2.3 LLC Performance Comparison

Fig. 6.2 compares the LLCs of BICM-SB and BICM-ZF with 2×2 antennas, for two correlation scenarios. Each curve is the envelope of the individual LLC curves for Gray-labeled BPSK, QPSK, 16QAM and 64QAM modulation formats (for the respective transmission scheme).

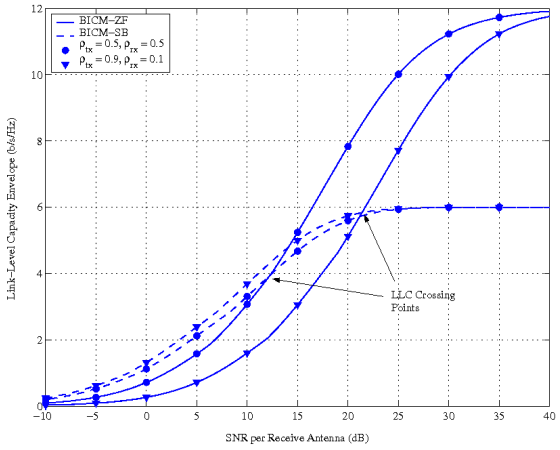

Figure 6.2: BICM LLC envelope for the ZF and SB transmission schemes. Two MIMO channel scenarios with exponential correlation coefficients $\rho_{\text{tx}} = 0.5, \rho_{\text{rx}} = 0.5$ and $\rho_{\text{tx}} = 0.9, \rho_{\text{rx}} = 0.1$ are considered.

The figure shows that the LLC of each transmission scheme depends on the channel correlation scenario. In particular, as the transmit correlation increases, SB benefits and ZF degrades. These curves motivate our new adaptive transmission approach which not only adapts the modulation format and code rate, but also adapts the transmission scheme (between SB and ZF). The relative performance of the two schemes clearly depends on both SNR and channel spatial correlation. For example, in the figure shown, in order to achieve the maximum LLC for the lower transmit correlation channel, SB should be used for SNRs below 12 dB, and ZF should be used for higher SNRs. For the higher transmit correlation channel, the crossing point is at 21 dB.

While these capacity results have motivated the new adaptive approach, for practical systems (with non capacity-achieving codes) we prefer to evaluate

the switching points based on achievable BER. Such is the topic of the following sections. In the numerical studies of Section 7.5.3, the capacity curves of this section are used as a benchmark of achievable performance.

6.3 General Expressions for the Error Probability

We now derive tight expressions for the BER of BICM-SB, BICM-OSTBC and BICM-ZF in spatially-correlated Rayleigh MIMO channels. These results will provide the fundamental tools for establishing the selection criterion for our proposed adaptive MIMO-BICM algorithm in Section 7.5.

Before proceeding, we note that although we are considering binary convolutional codes with low-complexity Viterbi decoding, the subsequent analytical BER results also apply directly to BICM-SB and BICM-ZF systems employing more powerful *turbo-like* codes [157, 158, 162] with iterative decoding (e.g. serial/parallel concatenated codes, and repeat and accumulate codes). It is only necessary to know the distance spectrum of the code. Moreover, the analytical procedure could also be adapted to BICM-SB, BICM-OSTBC and BICM-ZF systems with iterative demodulation (ID) and non-Gray labelings (i.e. as in the BICM-ID systems considered in [163–165]). However, in these particular cases, the general BER union-bound approach used in the sequel is known to yield accurate results only in the error-floor region of the BER curve (see, for example, [157, 158, 164]). It is also important to emphasize that both turbo-like codes and BICM-ID have much higher complexity than the non-iterative schemes considered in this chapter, making them unsuitable for

implementation in many practical systems.

6.3.1 BER Union Bound

The BER union bound for rate $R_c = k_c/n_c$ linear binary convolutional codes is given by [166]

$$\text{BER} \leq \frac{1}{k_c} \sum_{d=d_{\text{free}}}^{\infty} W_I(d) f(d, \mu, \mathcal{A}, \gamma) \tag{6.17}$$

where $W_I(d)$ is the total input weight of all error events at Hamming distance d, $f(.)$ is the codeword pairwise error probability (C-PEP), μ is the labeling map, and d_{free} is the free Hamming distance. Note that for the codes we consider the infinite series in (6.17) converges very quickly, and truncation to as little as 5 terms still yields accurate results.

6.3.2 Exact Expression for the C-PEP

To simplify the C-PEP analysis of both BICM-SB, BICM-OSTBC and BICM-ZF, we adopt the approach of [159] and force the BICM subchannels[2] to behave as binary-input output-symmetric (BIOS) channels by introducing a random bit-swapping variable u, which gives the well-known C-PEP [166]

$$f(d, \mu, \mathcal{A}, \gamma) = \Pr\left(\sum_{i=1}^{d} \mathcal{L}_i > 0\right) \tag{6.18}$$

assuming the all-zero codeword is transmitted, and where $\mathcal{L}_i$ is the log-likelihood metric for the i^{th} coded bit. Since the metrics $\mathcal{L}_i$ are i.i.d. under the assump-

[2]These are the equivalent channels between the transmitted binary codeword and the corresponding BICM bit metrics.

tion of ideal interleaving, we can evaluate the tail probability (6.18) based on the moment generating function (m.g.f.)[3]

$$\mathcal{M}_{\mathcal{L}}(s) \triangleq E_{\mathcal{L}}\left[\exp\left(s\mathcal{L}\right)\right] \tag{6.19}$$

as

$$f(d,\mu,\mathcal{A},\gamma) = \frac{1}{2\pi j}\int_{c-j\infty}^{c+j\infty} \mathcal{M}_{\mathcal{L}}(s)^d \,\frac{\mathrm{d}s}{s}. \tag{6.20}$$

Unfortunately in virtually all cases this solution must be evaluated using numerical complex integration techniques, thereby making it unsuitable for use in practical adaptive systems. In this chapter we use (6.20) for assessing the accuracy of our efficient C-PEP closed-form approximations.

6.3.3 Saddlepoint Approximation for the C-PEP

Since the C-PEP is the tail probability of a sum of i.i.d. random variables, a simplified closed-form expression is obtained by applying a saddlepoint approximation [167, App. 5A] to (6.18). This approximation is more accurate than the usual Chernoff bound, and is given by

$$f(d,\mu,\mathcal{A},\gamma) \approx \frac{1}{\sqrt{2\pi d\mathcal{K}''_{\mathcal{L}}(\hat{s})}\hat{s}}\exp\left(d\,\mathcal{K}_{\mathcal{L}}(\hat{s})\right) = \frac{1}{\sqrt{2\pi d\mathcal{K}''_{\mathcal{L}}(\hat{s})}\hat{s}}\mathcal{M}_{\mathcal{L}}(\hat{s})^d \tag{6.21}$$

where $\mathcal{K}_{\mathcal{L}}(\cdot)$ is the cumulant generating function (c.g.f.) of $\mathcal{L}$ given by

$$\mathcal{K}_{\mathcal{L}}(s) = \ln \mathcal{M}_{\mathcal{L}}(s) \tag{6.22}$$

[3]Note that we drop the subscript on $\mathcal{L}$ when considering the log likelihood ratio statistics at a single instant in time.

and where $\mathcal{K}_{\mathcal{L}}''(\hat{s})$ denotes the second derivative of $\mathcal{K}_{\mathcal{L}}(s)$, evaluated at the *saddlepoint* $\hat{s}$, which is the real value of s that minimizes $\mathcal{K}_{\mathcal{L}}(s)$ (and therefore also minimizes $\mathcal{M}_{\mathcal{L}}(s)$).

We note that the general saddlepoint approximation (6.21) was first used for the analysis of SISO BICM in AWGN and uncorrelated Rayleigh fading in [157], and further elaborated upon in [158]. In this chapter we apply the saddlepoint approximation to the more general correlated MIMO channel, and use it to derive new closed-form BER expressions.

6.4 Analysis of MIMO-BICM with Statistical Beamforming

6.4.1 Moment Generating Function of Log-Likelihood Metric

For BICM-SB transmission, the m.g.f. is easily obtained using (6.5), (6.6) and (6.19) as

$$\begin{aligned}\mathcal{M}_{\mathcal{L}}(s) &= E_{z,m,u,\mathbf{f}}\left[\exp\left(s\ln\frac{\sum_{\tilde{a}\in\mathcal{A}_{\bar{u}}^m}\exp\left(-\frac{|z-\sqrt{\gamma}\|\mathbf{f}\|^2\tilde{a}|^2}{\|\mathbf{f}\|^2}\right)}{\sum_{\tilde{a}\in\mathcal{A}_{u}^m}\exp\left(-\frac{|z-\sqrt{\gamma}\|\mathbf{f}\|^2\tilde{a}|^2}{\|\mathbf{f}\|^2}\right)}\right)\right] \\ &= E_{a,m,u,\underline{n},\mathbf{f}}\left[\left(\frac{\sum_{\tilde{a}\in\mathcal{A}_{\bar{u}}^m}\exp\left(-\frac{|\sqrt{\gamma}\|\mathbf{f}\|^2(a-\tilde{a})+\underline{n}|^2}{\|\mathbf{f}\|^2}\right)}{\sum_{\tilde{a}\in\mathcal{A}_{u}^m}\exp\left(-\frac{|\sqrt{\gamma}\|\mathbf{f}\|^2(a-\tilde{a})+\underline{n}|^2}{\|\mathbf{f}\|^2}\right)}\right)^s\right]. \end{aligned} \tag{6.23}$$

Averaging over the uniform bit-positions m, bit-swapping values u, and symbols $a\in\mathcal{A}_u^m$ gives

$$\mathcal{M}_{\mathcal{L}}(s) = \frac{1}{M2^M}\sum_{m=1}^{M}\sum_{u=0}^{1}\sum_{a\in\mathcal{A}_u^m}\mathcal{I}_{m,u,a}(s) \tag{6.24}$$

where

$$\mathcal{I}_{m,u,a}(s) = E_{\underline{n},\mathbf{f}}\left[\left(\frac{\sum_{\tilde{a}\in\mathcal{A}_{\bar{u}}^m}\exp\left(-\frac{|\sqrt{\gamma}\|\mathbf{f}\|^2(a-\tilde{a})+\underline{n}|^2}{\|\mathbf{f}\|^2}\right)}{\sum_{\tilde{a}\in\mathcal{A}_u^m}\exp\left(-\frac{|\sqrt{\gamma}\|\mathbf{f}\|^2(a-\tilde{a})+\underline{n}|^2}{\|\mathbf{f}\|^2}\right)}\right)^s\right]. \tag{6.25}$$

As for the BICM-SB LLC in (6.14), the expectation (6.25) can be evaluated via numerical integration using Gauss-Laguerre and Gauss-Hermite quadratures. We now show that at high SNR the expression can be calculated in closed-form. At high SNR, the ratio in (6.25) is dominated by a single minimum distance term[4] in the numerator and denominator, and by applying the bounding approach from [158, Eq. (39)] the Dominated Convergence Theorem [168] can be applied to yield

$$\mathcal{I}_{m,u,a}(s) = E_{\underline{n},\mathbf{f}}\left[\left(\frac{\exp\left(-\frac{|\sqrt{\gamma}\|\mathbf{f}\|^2(a-\tilde{a})+\underline{n}|^2}{\|\mathbf{f}\|^2}\right)}{\exp\left(-\frac{|\underline{n}|^2}{\|\mathbf{f}\|^2}\right)}\right)^s\right] \tag{6.26}$$

for $s<1$, where $\tilde{a}\in\mathcal{A}_{\bar{u}}^m$ is the nearest neighbor to $a\in\mathcal{A}_u^m$. Averaging over the noise yields

$$\begin{aligned}
\mathcal{I}_{m,u,a}(s) &= E_{\underline{n},\mathbf{f}}\left[\exp\left(\frac{-s|\sqrt{\gamma}\|\mathbf{f}\|^2(a-\tilde{a})+\underline{n}|^2+s|\underline{n}|^2}{\|\mathbf{f}\|^2}\right)\right] \\
&= E_{\underline{n},\mathbf{f}}\left[\exp\left(\frac{-s\gamma\|\mathbf{f}\|^4|a-\tilde{a}|^2-2s\,\Re\mathrm{e}\left(\sqrt{\gamma}\|\mathbf{f}\|^2\,(a-\tilde{a})\,\underline{n}^*\right)}{\|\mathbf{f}\|^2}\right)\right] \\
&= E_{\mathbf{f}}\left[\exp\left(-s\gamma\|\mathbf{f}\|^2|a-\tilde{a}|^2+s^2\gamma\|\mathbf{f}\|^2|a-\tilde{a}|^2\right)\right. \\
&\qquad\left.\times\int\frac{1}{\pi}\exp\left(-\frac{|\underline{n}+s\sqrt{\gamma}\|\mathbf{f}\|^2(a-\tilde{a})|^2}{\|\mathbf{f}\|^2}\right)\mathrm{d}\underline{n}\right] \\
&= E_{\|\mathbf{f}\|^2}\left[\exp\left(-\gamma\|\mathbf{f}\|^2|a-\tilde{a}|^2s(1-s)\right)\right].
\end{aligned} \tag{6.27}$$

[4]Note that if non-Gray mappings were considered, the multiplicity of nearest neighbors would need to be considered.

To evaluate the expectation in (6.27), we use (5.2) and (5.4), and recall that the distribution of $\mathbf{Z}$ in (5.2) is invariant under unitary transformation, to give

$$\begin{aligned}\|\mathbf{f}\|^2 &= \mathbf{u}_{s,\max}^\dagger \mathbf{H}^\dagger \mathbf{H} \mathbf{u}_{s,\max} \\ &\simeq \mathbf{u}_{s,\max}^\dagger \mathbf{U}_s \mathbf{\Lambda}_s^{\frac{1}{2}} \mathbf{U}_s^\dagger \mathbf{H}_w^\dagger \mathbf{U}_r \mathbf{\Lambda}_r \mathbf{U}_r^\dagger \mathbf{H}_w \mathbf{U}_s \mathbf{\Lambda}_s^{\frac{1}{2}} \mathbf{U}_s^\dagger \mathbf{u}_{s,\max} \\ &\simeq \mathbf{u}_{s,\max}^\dagger \mathbf{U}_s \mathbf{\Lambda}_s^{\frac{1}{2}} \mathbf{H}_w^\dagger \mathbf{\Lambda}_r \mathbf{H}_w \mathbf{\Lambda}_s^{\frac{1}{2}} \mathbf{U}_s^\dagger \mathbf{u}_{s,\max} \\ &\simeq \frac{\lambda_{s,\max}}{2} \mathcal{Q} \end{aligned} \tag{6.28}$$

where $\simeq$ denotes equivalence in distribution, $\lambda_{s,\max}$ is the maximum eigenvalue of $\mathbf{S}$, and

$$\mathcal{Q} = \sum_{\ell=1}^{N_r} \varepsilon_\ell \, \lambda_{r,\ell} \tag{6.29}$$

where $\lambda_{r,\ell}$ denotes the ℓ^{th} eigenvalue of $\mathbf{R}$, and the ε_ℓ's are i.i.d. exponentially-distributed random variables. As such, $\mathcal{Q}$ is a central quadratic form. Since the exponential distribution is a chi-squared distribution with *even* degrees of freedom, we use a general result from [140] to give the p.d.f. of $\mathcal{Q}$ as

$$f(\mathcal{Q}) = \sum_{\ell=1}^{N_r} g_\ell(\mathbf{\Lambda}_r) \, \frac{\exp\left(-\frac{\mathcal{Q}}{2\lambda_{r,\ell}}\right)}{2\lambda_{r,\ell}} \tag{6.30}$$

where

$$g_\ell(\mathbf{\Lambda}_r) = \prod_{j=1, j\neq\ell}^{N_r} \left(\frac{\lambda_{r,\ell}}{\lambda_{r,\ell} - \lambda_{r,j}} \right). \tag{6.31}$$

Using (6.30) and (6.28), along with the integration identity [141, Eq. 3.381.4], the expectation in (6.27) is evaluated as

$$\mathcal{I}_{m,u,a}(s) = \sum_{\ell=1}^{N_r} g_\ell(\mathbf{\Lambda}_r) \left(1 + \gamma |a - \tilde{a}|^2 \lambda_{s,\max} \lambda_{r,\ell} s(1-s)\right)^{-1}. \tag{6.32}$$

	$\mathcal{P}_M$	$\mathcal{E}_M$
BPSK	{1}	{4.0}
QPSK	{1}	{2.0}
16QAM	{3/4, 1/4}	{0.4, 1.6}
64QAM	{7/12, 1/4, 1/12, 1/12}	{ 0.0952, 0.3810, 0.8571, 1.5238}

Table 6.1: Breakdown of distance multiplicities between complement BICM subsets for various QAM/PSK constellations with Gray labelling

Now, substituting (6.32) into (6.24) gives a closed-form expression for the m.g.f. Unfortunately this expression requires the calculation of $M2^M N_t$ terms, $\mathcal{I}_{m,u,a}(s)$. We can see from (6.24) however, that these terms only depend on a through the squared Euclidean distance to its nearest neighbour $\tilde{a}$ in the complement subset. We previously showed in [169] that when Gray labeling PSK/QAM constellations were employed, summations of this form could be greatly simplified by exploiting the multiplicities of the Euclidean distances. In particular, in this case we find that (6.24) can be written in the efficient form

$$\mathcal{M}_{\mathcal{L}}(s) = \sum_{i=1}^{|P_M|} \mathcal{P}_{M,i} \hat{\mathcal{I}}_{\mathcal{E}_{M,i}}(s) \tag{6.33}$$

where the sets $\mathcal{P}_M$ (with cardinality $|\mathcal{P}_M|$) and $\mathcal{E}_M$ are defined in Table 6.1, with i^{th} element $\mathcal{P}_{M,i}$ and $\mathcal{E}_{M,i}$ respectively, and where $\hat{\mathcal{I}}_{\mathcal{E}_{M,i}}(s)$ is as in (6.32), but with $|a - \tilde{a}|^2$ replaced with $\mathcal{E}_{M,i}$.

6.4.2 Closed-form C-PEP Based on Saddlepoint Approximation

Noting that the the m.g.f. (6.33) is minimized at the saddlepoint $\hat{s} = \frac{1}{2}$, we use (6.33) in (6.21) to obtain (after simple but tedius algebra) the saddlepoint approximation to the C-PEP

$$f(d,\mu,\mathcal{A},\gamma) \approx \frac{1}{2\sqrt{\pi d}} \frac{\left[\sum_{i=1}^{|\mathcal{P}_M|} \mathcal{P}_{M,i} \sum_{\ell=1}^{N_r} g_\ell(\mathbf{\Lambda}_r) \left(1+\frac{\gamma \mathcal{E}_{M,i}\lambda_{s,\max}\lambda_{r,\ell}}{4}\right)^{-1}\right]^{d+\frac{1}{2}}}{\sqrt{\sum_{i=1}^{|\mathcal{P}_M|} \mathcal{P}_{M,i} \sum_{\ell=1}^{N_r} g_\ell(\mathbf{\Lambda}_r) \left(1+\frac{\gamma \mathcal{E}_{M,i}\lambda_{s,\max}\lambda_{r,\ell}}{4}\right)^{-2} \left(\frac{\gamma \mathcal{E}_{M,i}\lambda_{s,\max}\lambda_{r,\ell}}{4}\right)}} \tag{6.34}$$

This expression is easy to compute in practice since $|\mathcal{P}_M|$ is small, and all terms are straightforward functions of the eigenvalues of the correlation matrices, and the SNR.

6.4.3 Simplified C-PEP

Applying the following approximation to the denominator of (6.34),

$$\left(\frac{\gamma \mathcal{E}_{M,i}\lambda_{s,\max}\lambda_{r,\ell}}{4}\right) \approx \left(\frac{\gamma \mathcal{E}_{M,i}\lambda_{s,\max}\lambda_{r,\ell}}{4}\right) + 1 \tag{6.35}$$

we obtain a simplified C-PEP expression given by

$$f(d,\mu,\mathcal{A},\gamma) \approx \frac{1}{2\sqrt{\pi d}} \left[\sum_{i=1}^{|\mathcal{P}_M|} \mathcal{P}_{M,i} \sum_{\ell=1}^{N_r} g_\ell(\mathbf{\Lambda}_r) \left(1+\frac{\gamma \mathcal{E}_{M,i}\lambda_{s,\max}\lambda_{r,\ell}}{4}\right)^{-1}\right]^{d}. \tag{6.36}$$

6.4.4 BER Performance Results

Fig. 6.3 compares the preceding analytical BICM-SB BER expressions with Monte-Carlo simulation results, for a 2×2 system with Gray-labeled

QPSK, 16QAM and 64QAM constellations. Results are presented for the optimal 64-state 1/2 rate binary convolutional code with $d_{\text{free}} = 10$, and with ideal interleaving. We consider the exponential correlation model with correlation coefficients $\rho_{\text{tx}} = \rho_{\text{rx}} = 0.5$. The 'saddlepoint' curves were obtained by substituting the C-PEP expression (6.34) into (6.17). Note that, as expected, they are within 0.2 dB of the simulated curves for low to moderate BERs since the union bound is known to be tight for convolutional codes for SNRs above the cut-off rate. The 'saddlepoint (approx)' curves were obtained from (6.36), and are within 1 dB of the simulated curves in all cases. For comparison, results are also presented based on the exact C-PEP expression (6.20). To evaluate this expression, the m.g.f. (6.33) was used in (6.20), and the complex integration was evaluated numerically using Gauss-Chebyshev quadrature (GCQ) rules [170]. We clearly see that the simplified closed-form saddlepoint approximation suffers negligible loss compared with (6.20).

6.5 Analysis of MIMO-BICM with OSTBC

6.5.1 Moment Generating Function of Log-Likelihood Metric

For OSTBC transmission, the m.g.f. is easily obtained using (6.11), (6.12), and (6.19) as

$$\mathcal{M}_{\mathcal{L}}(s) = E_{\mathcal{V}}\left[\left(\frac{\sum_{\tilde{a}\in\mathcal{A}_{\bar{u}}^{m}} \exp\left(-\frac{|\sqrt{\gamma}\|\mathbf{H}\|_F^2(a_k-\tilde{a})+\underline{n}_k|^2}{\|\mathbf{H}\|_F^2}\right)}{\sum_{\tilde{a}\in\mathcal{A}_{u}^{m}} \exp\left(-\frac{|\sqrt{\gamma}\|\mathbf{H}\|_F^2(a_k-\tilde{a})+\underline{n}_k|^2}{\|\mathbf{H}\|_F^2}\right)}\right)^{s}\right] \tag{6.37}$$

where, for notational convenience, we have grouped the expectation variables into the vector $\mathcal{V} = (a_k, m, u, k, \mathbf{H}, \underline{n}_k)$, where u is a uniform binary random variable.

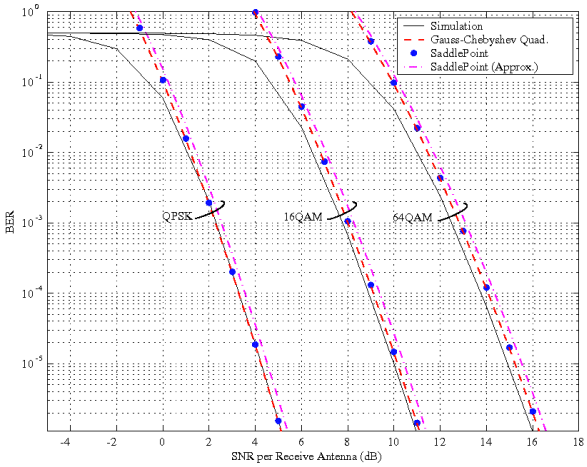

Figure 6.3: Simulated and analytical BER for 2×2 BICM-SB with a $\frac{1}{2}$ rate code, and for various modulation schemes. An exponential correlation model is used, with correlation coefficient 0.5 at both the transmitter and receiver.

In general, this equation does not admit a closed-form solution. At high SNR, however, closed-form solutions do exist and these provide an approximation for all SNRs. Following the general approach in [3, 157] we average over the uniform bit-positions m, bit-swapping values u, and symbols $a_k \in \mathcal{A}_u^m$, and apply the Dominated Convergence Theorem to obtain

$$\mathcal{M}_{\mathcal{L}}(s) = \sum_{i=1}^{|P_M|} \mathcal{P}_{M,i}\, \mathcal{I}_{\mathcal{E}_{M,i}}(s) \tag{6.38}$$

where the sets $\mathcal{P}_M$ (with cardinality $|\mathcal{P}_M|$) and $\mathcal{E}_M$ are defined in Table 6.1, with i^{th} element $\mathcal{P}_{M,i}$ and $\mathcal{E}_{M,i}$ respectively, and

$$\mathcal{I}_{\mathcal{E}_{M,i}}(s) = E_{\underline{n},\mathbf{H}}\left[\left(\frac{\exp\left(-\frac{|\sqrt{\gamma}\|\mathbf{H}\|_F^2\sqrt{\mathcal{E}_{M,i}}+\underline{n}|^2}{\|\mathbf{H}\|_F^2}\right)}{\exp\left(-\frac{|\underline{n}|^2}{\|\mathbf{H}\|_F^2}\right)}\right)^s\right]$$

where $\underline{n} \sim \mathcal{CN}(0, \|\mathbf{H}\|_F^2)$. Averaging over $\underline{n}$, and using (5.33) gives

$$\mathcal{I}_{\mathcal{E}_{M,i}}(s) = E_\eta \left[\exp\left(-\frac{\gamma\, \eta\, \mathcal{E}_{M,i} s(1-s)}{2} \right) \right]. \tag{6.39}$$

Finally, we use (5.35) to obtain

$$\mathcal{I}_{\mathcal{E}_{M,i}}(s) = \sum_{\ell=1}^{r} \prod_{j=1, j\neq\ell}^{r} \left(\frac{\lambda_{q,\ell}}{\lambda_{q,\ell} - \lambda_{q,j}} \right) \frac{1}{(1 + \mathcal{E}_{M,i}\lambda_{q,\ell} s(1-s))}. \tag{6.40}$$

6.5.2 Closed-form C-PEP Based on Saddlepoint Approximation

Noting that the m.g.f. (6.45) is minimized at the saddlepoint $\hat{s} = \frac{1}{2}$, and using (6.40) and (6.45) in (6.21), we obtain the saddlepoint approximation to the C-PEP given by (6.41).

$$f(d, \mu, \mathcal{A}, \gamma) \approx \frac{1}{2\sqrt{\pi d}} \frac{\left[\sum_{i=1}^{|\mathcal{P}_M|} \mathcal{P}_{M,i} \sum_{\ell=1}^{r} \left(1 + \frac{\gamma \mathcal{E}_{M,i}\lambda_{q,\ell}}{4} \right)^{-1} \prod_{j=1, j\neq\ell}^{r} \left(\frac{\lambda_{q,\ell}}{\lambda_{q,\ell} - \lambda_{q,j}} \right) \right]^{d+\frac{1}{2}}}{\sqrt{\sum_{i=1}^{|\mathcal{P}_M|} \mathcal{P}_{M,i} \sum_{\ell=1}^{r} \left(1 + \frac{\gamma \mathcal{E}_{M,i}\lambda_{q,\ell}}{4} \right)^{-2} \left(\frac{\gamma \mathcal{E}_{M,i}\lambda_{q,\ell}}{4} \right) \prod_{j=1, j\neq\ell}^{r} \left(\frac{\lambda_{q,\ell}}{\lambda_{q,\ell} - \lambda_{q,j}} \right)}} \tag{6.41}$$

6.5.3 Simplified C-PEP

Applying the following approximation to the denominator of (6.41)

$$\left(\frac{\gamma \mathcal{E}_{M,i}\lambda_{q,\ell}}{4} \right) \approx \left(\frac{\gamma \mathcal{E}_{M,i}\lambda_{q,\ell}}{4} \right) + 1 \tag{6.42}$$

we obtain a simplified C-PEP expression given by (6.43).

$$f(d,\mu,\mathcal{A},\gamma) \approx \frac{1}{2\sqrt{\pi d}} \left[\sum_{i=1}^{|\mathcal{P}_M|} \mathcal{P}_{M,i} \sum_{\ell=1}^{r} \left(1 + \frac{\gamma \mathcal{E}_{M,i} \lambda_{q,\ell}}{4}\right)^{-1} \prod_{j=1, j\neq\ell}^{r} \left(\frac{\lambda_{q,\ell}}{\lambda_{q,\ell} - \lambda_{q,j}}\right) \right]^{d} \tag{6.43}$$

6.5.4 BER Performance Results

Fig. 6.4 compares the preceding analytical BICM-OSTBC BER expressions with Monte-Carlo simulation results, for a 2×2 system with various Gray-labeled constellations. Results are presented for the optimal 64-state 1/2 rate binary convolutional code with $d_{\text{free}} = 10$. The 'saddlepoint' curves were obtained from the C-PEP expression (6.41), and are clearly tight for low to moderate BERs. The 'saddlepoint (approx)' curves were obtained from (6.43), and are within 1 dB of the simulated curves in all cases.

6.6 Analysis of MIMO-BICM with Zero-Forcing Receivers

6.6.1 Moment Generating Function of Log-Likelihood Metric

For BICM-ZF transmission, the m.g.f. is easily obtained using (6.11), (6.12), and (6.19) as

$$\mathcal{M}_{\mathcal{L}}(s) = E_{z,m,u,k,\mathbf{w}_k} \left[\exp\left(s \ln \frac{\sum_{\tilde{a}\in\mathcal{A}_u^m} \exp\left(-\frac{|z-\sqrt{\gamma}\tilde{a}|^2}{\|\mathbf{w}_k\|^2}\right)}{\sum_{\tilde{a}\in\mathcal{A}_u^m} \exp\left(-\frac{|z-\sqrt{\gamma}\tilde{a}|^2}{\|\mathbf{w}_k\|^2}\right)} \right) \right]. \tag{6.44}$$

In [169] we presented a closed-form high SNR solution to (6.44) given by

$$\mathcal{M}_{\mathcal{L}}(s) = \frac{1}{N_t} \sum_{k=1}^{N_t} \sum_{i=1}^{|P_M|} \mathcal{P}_{M,i}\, \tilde{\mathcal{J}}_{k,\mathcal{E}_{M,i}}(s) \tag{6.45}$$

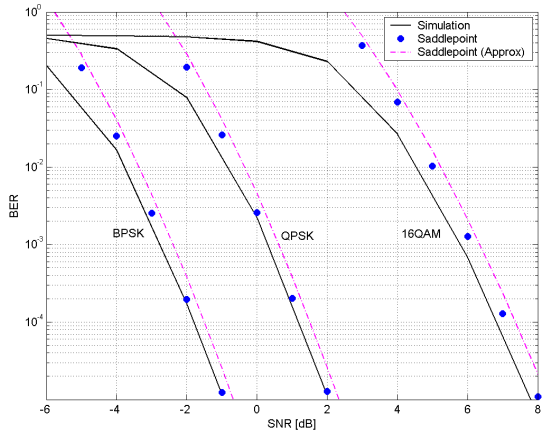

Figure 6.4: Simulated and analytical BER of 2×2 BICM-OSTBC employing the optimal $\frac{1}{2}$ rate code ($d_{\text{free}} = 10$). The exponential model is used, with $\rho_{\text{tx}} = 0.5$ and $\rho_{\text{rx}} = 0.1$.

where

$$\tilde{\mathfrak{J}}_{k,\mathcal{E}_{M,i}}(s) \approx \left| \mathbf{I}_{N_r} + \frac{\gamma \mathcal{E}_{M,i} s(1-s) \mathbf{\Lambda}_r}{[\mathbf{S}^{-1}]_{k,k}} \right|^{-1} \frac{\text{tr}_{N_t-1}(\mathbf{\Lambda}_r)}{\text{tr}_{N_t-1}\left(\mathbf{\Lambda}_r \left[\mathbf{I}_{N_r} + \frac{\gamma \mathcal{E}_{M,i} s(1-s) \mathbf{\Lambda}_r}{[\mathbf{S}^{-1}]_{k,k}} \right]^{-1} \right)} \tag{6.46}$$

where $[\cdot]_{k,k}$ denotes the k^{th} diagonal element, and $\text{tr}_\ell(\cdot)$ is the ℓ^{th} elementary symmetric function (e.s.f.) defined as [146, 171]

$$\text{tr}_\ell(\mathbf{X}) = \sum_{\{\underline{\alpha}\}} \prod_{i=1}^{\ell} \lambda_{x,\alpha_i} = \sum_{\{\underline{\alpha}\}} \left| \mathbf{X}_{\underline{\alpha}}^{\underline{\alpha}} \right| \tag{6.47}$$

for arbitrary Hermitian positive-definite $\mathbf{X} \in \mathcal{C}^{n \times n}$. In (6.47), the sum is over all ordered $\underline{\alpha} = \{\alpha_1, \ldots, \alpha_\ell\} \subseteq \{1, \ldots, n\}$, $\lambda_{x,i}$ denotes the i^{th} eigenvalue of $\mathbf{X}$, and $\mathbf{X}_{\underline{\alpha}}^{\underline{\alpha}}$ is the $\ell \times \ell$ principle submatrix of $\mathbf{X}$, formed by taking only the rows and columns indexed by $\underline{\alpha}$.

6.6.2 Closed-form C-PEP Based on Saddlepoint Approximation

The numerator of the saddlepoint approximation (6.21) for BICM-ZF is obtained by evaluating (6.45) and (6.46) at the saddlepoint $\hat{s}$, which is easily found to be $\frac{1}{2}$. To evaluate the denominator of (6.21) we require $\mathcal{K}''_{\mathcal{L}}(\hat{s})$. To do this, we start by using (6.22) and (6.45) to write

$$\mathcal{K}''_{\mathcal{L}}(\hat{s}) = \frac{\mathcal{M}''_{\mathcal{L}}(\hat{s})}{\mathcal{M}_{\mathcal{L}}(\hat{s})} - \left(\frac{\mathcal{M}'_{\mathcal{L}}(\hat{s})}{\mathcal{M}_{\mathcal{L}}(\hat{s})}\right)^2 \tag{6.48}$$

where

$$\mathcal{M}'_{\mathcal{L}}(\hat{s}) = \frac{1}{N_t}\sum_{k=1}^{N_t}\sum_{i=1}^{|P_M|} \mathcal{P}_{M,i}\,\tilde{\mathcal{I}}'_{k,\mathcal{E}_{M,i}}(\hat{s}) \tag{6.49}$$

$$\mathcal{M}''_{\mathcal{L}}(\hat{s}) = \frac{1}{N_t}\sum_{k=1}^{N_t}\sum_{i=1}^{|P_M|} \mathcal{P}_{M,i}\,\tilde{\mathcal{I}}''_{k,\mathcal{E}_{M,i}}(\hat{s}). \tag{6.50}$$

We must now evaluate $\tilde{\mathcal{I}}'(\hat{s})$ and $\tilde{\mathcal{I}}''(\hat{s})$. Unfortunately, it is very difficult to evaluate these derivatives based directly on the form of $\tilde{\mathcal{I}}(s)$ given in (6.46). In the Appendix we perform significant algebraic manipulations to calculate these derivatives as follows

$$\begin{aligned}
&\tilde{\mathcal{I}}'_{k,\mathcal{E}_{M,i}}(\hat{s}) = 0 \\
&\tilde{\mathcal{I}}''_{k,\mathcal{E}_{M,i}}(\hat{s}) = 8\tilde{\mathcal{I}}_{k,\mathcal{E}_{M,i}}(\hat{s})^2 \left(\sum_{\ell=1}^{N_r-N_t+1} \ell\, C_\ell(\mathbf{\Lambda}_r)\left(\frac{\gamma\mathcal{E}_{M,i}}{4\left[\mathbf{S}^{-1}\right]_{kk}}\right)^\ell\right)
\end{aligned} \tag{6.51}$$

where $C_\ell(\mathbf{\Lambda}_r)$, for $\ell = 1, \ldots, N_r - N_t + 1$, are auxiliary constants, defined in (B.9). We now substitute (6.51) into (6.49) and (6.50), simplify the resulting expression, and then use (6.48) and (6.21) to give the final closed-form C-PEP

saddlepoint approximation as follows

$$f(d,\mu,\mathcal{A},\gamma) \approx \frac{1}{2N_t^d\sqrt{\pi d}} \frac{\left(\sum_{k=1}^{N_t}\sum_{i=1}^{|\mathcal{P}_M|}\mathcal{P}_{M,i}\left(1+\sum_{\ell=1}^{N_r-N_t+1}\left(\frac{\gamma\mathcal{E}_{M,i}}{4[\mathbf{S}^{-1}]_{kk}}\right)^{\ell}C_\ell(\mathbf{\Lambda}_r)\right)^{-1}\right)^{d+\frac{1}{2}}}{\sqrt{\sum_{k=1}^{N_t}\sum_{i=1}^{|\mathcal{P}_M|}\mathcal{P}_{M,i}\frac{\sum_{\ell=1}^{N_r-N_t+1}\ell\left(\frac{\gamma\mathcal{E}_{M,i}}{4[\mathbf{S}^{-1}]_{kk}}\right)^{\ell}C_\ell(\mathbf{\Lambda}_r)}{\left(1+\sum_{\ell=1}^{N_r-N_t+1}\left(\frac{\gamma\mathcal{E}_{M,i}}{4[\mathbf{S}^{-1}]_{kk}}\right)^{\ell}C_\ell(\mathbf{\Lambda}_r)\right)^2}}}. \tag{6.52}$$

Special Case: $N_t = 2, N_r = 2$

For 2×2 systems, (6.52) can be reduced to a simple closed-form expression[5]. We first note that [146]

$$\left[\mathbf{S}^{-1}\right]_{kk} = \frac{|\mathbf{S}^{kk}|}{|\mathbf{S}|} \tag{6.53}$$

where $\mathbf{S}^{kk}$ corresponds to $\mathbf{S}$ with the k^{th} row and column removed, and recall that the spatial correlation matrices have unity diagonal entries, such that for 2×2 systems

$$\left[\mathbf{S}^{-1}\right]_{kk} = \frac{1}{|\mathbf{S}|} \tag{6.54}$$

for $k = 1, 2$. Secondly, we note that (6.52) contains only a single auxiliary constant, $C_1(\mathbf{\Lambda}_r)$, in the 2×2 case, in which case (B.9) reduces to

$$C_1(\mathbf{\Lambda}_r) = 2|\mathbf{R}|. \tag{6.55}$$

[5]Although not shown, simplified expressions are also possible for the more general case $N_r = N_t = n$, and for systems with $N_t = 2$ and $N_r \geq 2$.

Substituting (6.54) and (6.55) into (6.52) and simplifying yields

$$f(d,\mu,\mathcal{A},\gamma) \approx \frac{1}{2\sqrt{\pi d}} \frac{\left(\sum_{i=1}^{|\mathcal{P}_M|} \mathcal{P}_{M,i}\left(1+\frac{\gamma\mathcal{E}_{M,i}|\mathbf{R}||\mathbf{S}|}{4}\right)^{-1}\right)^{d+\frac{1}{2}}}{\sqrt{\sum_{i=1}^{|\mathcal{P}_M|} \mathcal{P}_{M,i} \frac{\frac{\gamma\mathcal{E}_{M,i}|\mathbf{R}||\mathbf{S}|}{4}}{\left(1+\frac{\gamma\mathcal{E}_{M,i}|\mathbf{R}||\mathbf{S}|}{4}\right)^2}}}. \tag{6.56}$$

6.6.3 Simplified C-PEP at High SNR

In the high SNR regime, we note that the summations over ℓ in (6.52) are dominated by the terms corresponding to $\ell = N_r - N_t + 1$. We also note from (B.9) that

$$C_{N_r-N_t+1}(\mathbf{\Lambda}_r) = \binom{N_r}{N_t-1}|\mathbf{R}|. \tag{6.57}$$

With these observations, after basic algebra it is easily shown that (6.52) reduces to

$$f(d,\mu,\mathcal{A},\gamma) \approx \left(\frac{\gamma}{4}\right)^{-(N_r-N_t+1)d} \frac{\mathrm{tr}_{N_t-1}\left(\mathbf{\Lambda}_r\right)^d}{2N_t^d\sqrt{\pi d}\binom{N_r}{N_t-1}^d|\mathbf{R}|^d} \tag{6.58}$$

$$\times \left(\sum_{k=1}^{N_t}\sum_{i=1}^{|\mathcal{P}_M|} \mathcal{P}_{M,i}\left(\frac{\mathcal{E}_{M,i}}{[\mathbf{S}^{-1}]_{kk}}\right)^{-(N_r-N_t+1)}\right)^d \tag{6.59}$$

which is clearly much simpler than (6.52).

Special Case: $N_t = 2, N_r = 2$

In this case, (6.59) reduces to the extremely simple expression

$$f(d,\mu,\mathcal{A},\gamma) \approx \frac{1}{2\sqrt{\pi d}}\left(\frac{\gamma|\mathbf{R}||\mathbf{S}|}{4}\left(\sum_{i=1}^{|\mathcal{P}_M|}\frac{\mathcal{P}_{M,i}}{\mathcal{E}_{M,i}}\right)^{-1}\right)^{-d}. \tag{6.60}$$

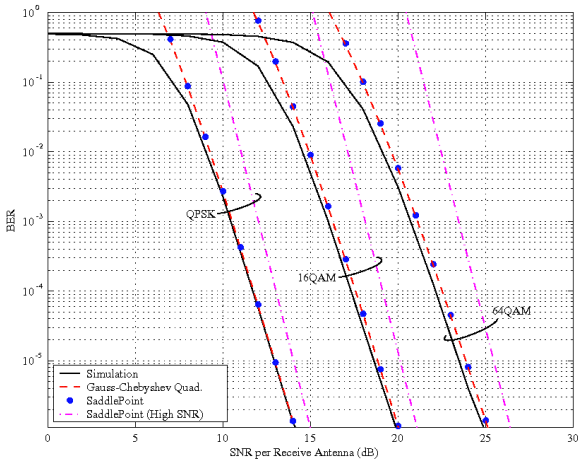

Figure 6.5: Simulated and analytical BER 2×2 BICM-ZF employing a $\frac{1}{2}$ rate code, and for various modulation schemes. An exponential correlation model is used, with correlation coefficient 0.5 at both the transmitter and receiver.

6.6.4 BER Performance Results

Fig. 6.5 compares the preceding analytical BICM-ZF BER expressions with Monte-Carlo simulation results, for a 2×2 system with Gray-labeled QPSK, 16QAM and 64QAM constellations. The same system and channel parameters are assumed as in Section 6.4.4. The 'saddlepoint' curves were obtained by substituting the C-PEP expression (6.56) into (6.17), and are clearly tight for low to moderate BERs. The 'saddlepoint (high SNR)' curves were obtained from (6.60). We see that these curves tighten as the BER is reduced, and are within 1 dB of the simulated curves for BERs below 10^{-6}. For comparison, results are also presented based on the exact C-PEP expression (6.20), which are obtained using the m.g.f. (6.45), and GCQ rules for evaluating the complex integration in (6.20).

Chapter 7

Practical Adaptive MIMO Algorithms

One way to enhance the spectral efficiency of wireless communication systems is to adapt the transmission rate to the changing channel conditions. Adaptive transmission techniques can be designed to switch between different combinations of modulation/coding schemes or transmission strategies. Adaptive techniques have been proposed in the literature to switch between different MIMO schemes based on the instantaneous channel knowledge or relying on time/frequency selectivity indicators. This chapter proposes an adaptive method based on channel statistics, rather than instantaneous channel knowledge, to avoid feedback overhead. This method exploits the spatial selectivity inherent in the channel to switch between different MIMO schemes, as a means to improve system performance.

7.1 Introduction

MIMO technology exploits the spatial components of the wireless channel to provide high data rates, through multiplexing, or better coverage, through diversity schemes. Though there are fundamental tradeoffs between diversity and multiplexing, both can be achieved simultaneously to different degrees

in fading channels [125]. In practical systems, one promising solution to increase throughput is link adaptation [127]. The conventional link adaptation is enabled by switching between different combinations of modulation/coding rates, by tracking the changing channel conditions, as a means to increase spectral efficiency. Additionally, switching can be enabled between diversity or multiplexing MIMO schemes to provide throughput or coverage depending on the channel quality.

This chapter presents a novel system architecture for adaptive MIMO transmissions and practical solutions to enable adaptation, based on the channel quality in the time, frequency and space domains. Four MIMO transmission schemes are considered: statistical beamforming, diversity, hybrid and multiplexing. Diversity schemes are employed to increase link robustness, resulting in better coverage. Hybrid techniques achieve higher data rates and provide good diversity advantage by using both diversity and multiplexing schemes. Multiplexing schemes are used to enhance spectral efficiency, when the channel is characterized by good quality and large number of degrees of freedom. We combine adaptive MIMO switching methods with conventional adaptive modulation/coding techniques by employing a set of practical transmission modes, optimally defined to reduce the amount of control information. To make our discussion concrete, we present system specifications and performance results in the context of the IEEE 802.16e standard for future wireless metropolitan area networks (WMANs) supporting MIMO technology [1].

7.2 Fundamentals of Adaptive MIMO Systems

The key idea of adaptive MIMO transmission methods is to switch between different signaling techniques in response to changing conditions of the propagation channel, resulting in enhanced system performance. We begin by describing the physical characteristics of wireless channels to gain insights on the fundamental criteria to design adaptive MIMO systems.

7.2.1 MIMO Wireless Channels

The signal measured at the receiver of typical wireless communication systems consists of multiple copies of the same transmit signal, produced by different paths in the propagation environment. As a result of the multi-paths, different wavefronts impinge on the receiving antenna with uncorrelated phases and add up constructively or destructively, yielding fluctuations (i.e., peaks or fades) of the signal strength over time, or *time selectivity*. The rate of the temporal variations of the signal is proportional to the Doppler spread of the channel, determined by the speed of the transmitter/receiver or the moving scattering objects in the propagation environment. Fig. 7.1 shows the temporal variation of the signal power (h11) for users moving at the speed of 80 Km/h.

In wide band transmissions, the relative delay of different propagation paths may be greater than the symbol period, resulting in channel fluctuation in the frequency domain. This fading effect is known as *frequency selectivity* and the rate of variation of the channel gain in frequency is a function of

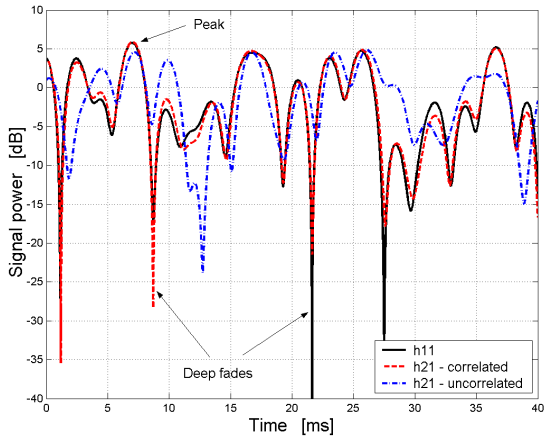

Figure 7.1: Signal power measured at two different antennas of a MIMO array, with and without channel spatial correlation. The temporal channel fading is due to Doppler effects.

the delay spread of the multi-paths. The delay spread varies depending on the propagation environment such as indoor versus outdoor, or macro- versus micro-cell scenarios.

When the transmitter or receiver is equipped with multiple antennas, the signals received at different elements of the arrays may be fading independently, and the channel is characterized by its *spatial selectivity*. The spatial selectivity depends both on the physical characteristics of the channel (i.e., spatial distribution of the impinging wavefronts) and array properties (i.e., antenna spacing, cross-polarization, antenna radiation patterns). The spatial distribution of the multi-paths determines the power angle spectrum of the channel, characterized in part by the angle spread or variance of the angular spectrum. The larger the angle spread the higher the probability that multi-

ple wavefronts add up with different phases at different elements of the array, producing low correlated signals. Another channel effect that has impact on the spatial selectivity is the line-of-sight (LOS). When the LOS component is dominant, the signals measured at different antennas are equally strong over time, resulting in reduced number of degrees of freedom in the spatial domain.

Fig. 7.2 shows the power angle/delay profile of typical outdoor channel environments. The wavefronts impinge on the antenna array from different angles of arrival (ranging between -60^{o} and 60^{o} with respect to the broadside direction of the uniform linear array) and with different delays. The impinging rays are clustered around few angles and delays, and each cluster identifies the energy coming from one specific scattering object in the propagation environment. In more general scenarios, the higher the number and angle spread of the clusters the lower the channel spatial correlation. Fig. 7.1 shows the effect of the spatial correlation on the signal power measured at two different antennas of the array. In presence of low spatial correlation (i.e., large antenna spacing) the received signals h11 and h21 fade independently, resulting in higher spatial diversity.

The channel time, frequency and spatial selectivity described above can be exploited in practical systems to improve link performance via adaptive MIMO techniques. Adaptive MIMO systems switch between robust or high data-rate signalling schemes (consisting of different combinations of moduation/coding and MIMO schemes) to combat signal fading and enhance system throughput.

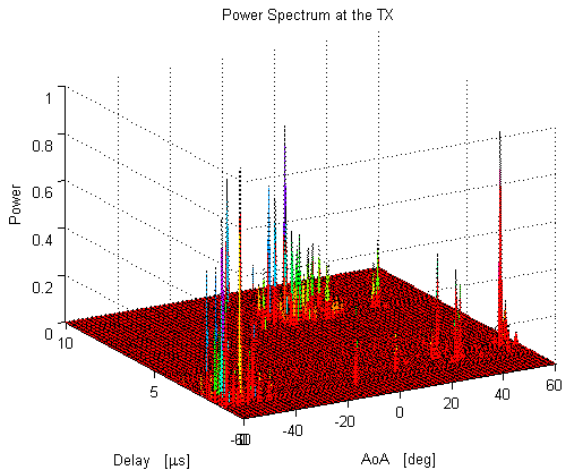

Figure 7.2: Power angle/delay profile of typical spatially correlated channel environments.

7.2.2 Modulation and Coding Schemes

Multiple modulation schemes and forward error correction (FEC) codes are defined in standards wireless communication systems to enable link adaptation. The current wireless standards employing MIMO technology (i.e., IEEE 802.11n, IEEE 802.16e, and 3GPP) define different sets of modulation orders and coding rates that are generally combined in predefined modulation/coding schemes (MCSs).

As an example, the IEEE 802.16e standard defines three modulation schemes: QPSK, 16QAM and 64QAM [1]. Additionally, various FEC coding techniques are possible, such as convolutional code (CC), convolutional turbo code (CTC), and low density parity check (LDPC) code. A few coding rates are considered: 1/2, 2/3, 3/4, and 5/6 (the rate 5/6 code is used only for CTC). Moreover, the standard proposes look-up tables with predefined MCSs

reported in Table 7.1. In the standard, mode 2 is not defined for CC, whereas mode 5 is not defined for CC and CTC.

MCS ID	Modulation	Code Rate
1	QPSK	1/2
2	QPSK	2/3
3	QPSK	3/4
4	16-QAM	1/2
5	16-QAM	2/3
6	16-QAM	3/4
7	64-QAM	2/3
8	64-QAM	3/4

Table 7.1: Modulation/coding schemes (MCSs) as in the IEEE 802.16e standard [1].

7.2.3 MIMO Schemes

We consider three open-loop MIMO transmission techniques defined in the IEEE 802.16e standard: Matrix A, exploiting only diversity; Matrix B, combining diversity and spatial multiplexing; Matrix C, employing only spatial multiplexing. We consider the practical case of four transmit antennas. Hereafter, we briefly review these schemes and outline their properties.

Matrix A (Diversity) – Space-time block codes (STBCs) efficiently exploit transmit diversity to combat channel fading while keeping low decoding complexity. A number of STBCs for four transmit antenna systems have been proposed thus far. A rate 3/4, full-diversity code was presented in [36], while [172] proposed a rate 1 quasi-orthogonal STBC not yielding full diversity.

There are several examples of space-time codes that achieve full diversity and rate 1.

Matrix B (Hybrid) – This scheme combines diversity and spatial multiplexing by encoding the transmit signal across four antennas [38]. Two Alamouti schemes are run in parallel over two different sets of antennas, enabling rate 2 transmissions. To decode the data, zero forcing (ZF), minimum mean square error (MMSE), or maximum likelihood (ML) receivers can be employed.

Matrix C (Spatial multiplexing) – Spatial multiplexing systems transmit multiple parallel data streams to enhance spectral efficiency. The V-BLAST architecture was proposed in [173] to achieve high spectral efficiency over wireless channels characterized by rich scattering. The receive streams can be decoded through linear (i.e., ZF or MMSE) or non-linear receivers. In general, non-linear receivers yield better error rate performance, at the cost of higher computational complexity. Typical examples of non-linear receivers are successive interference cancellation (SIC) and maximum likelihood (ML).

7.2.4 Definition of the MIMO Transmission Modes

Adaptive MIMO architectures utilize different combinations of MCSs and MIMO schemes to enable transmissions over the wireless link. For systems employing the eight MCSs in Table 7.1 and the three MIMO schemes described above, it is possible to define the set of 24 *transmission modes* reported in Table 7.2. These modes are ordered by increasing values of peak spectral efficiency. Some of these modes provide same throughput for different SNR requirements

and may be discarded to reduce feedback overhead as described in the following section.

Mode ID	**MCS ID**	**MIMO Scheme**	**Peak SE** [bps/Hz]
1	1	Matrix A	1
2	2	Matrix A	1.3
3	3	Matrix A	1.5
4	4	Matrix A	2
5	1	Matrix B	2
6	5	Matrix A	2.7
7	2	Matrix B	2.7
8	6	Matrix A	3
9	3	Matrix B	3
10	7	Matrix A	4
11	4	Matrix B	4
12	1	Matrix C	4
13	8	Matrix A	4.5
14	5	Matrix B	5.3
15	2	Matrix C	5.3
16	6	Matrix B	6
17	3	Matrix C	6
18	7	Matrix B	8
19	4	Matrix C	8
20	8	Matrix B	9
21	5	Matrix C	10.7
22	6	Matrix C	12
23	7	Matrix C	16
24	8	Matrix C	18

Table 7.2: MIMO transmission modes and corresponding values of spectral efficiency (SE).

7.3 Adaptive MIMO Transmission Techniques

A simplified framework for adaptive MIMO transmission is depicted in Fig. 7.3. The general adaptation mechanism can be summarized as follows: the receiver estimates the channel quality information (CQI) and sends it back to the transmitter; the transmitter processes the CQI and selects the optimal transmission mode (i.e., combination of MCS and MIMO scheme); the receiver is informed of the new selected mode via low-rate control channel and adaptively switches between different receivers, depending on the selected mode. Alternatively, the receiver may estimate the optimal transmission mode based on the CQI and send it back to the transmitter. One of the design challenges of adaptive MIMO architectures is to define efficient adaptation modules that use minimum amount of feedback information, without sacrificing much the systems performance. Hereafter, we present different adaptive methods designed to enhance throughput or produce diversity gain, and discuss their performance results.

7.3.1 Throughput-Based Adaptive Methods

One common technique employed in broadband wireless systems to achieve high throughput in fading channels is adaptive modulation and coding (AMC). The key idea of AMC is to jointly adapt the modulation order and coding rate to the changing channel conditions, for fixed power constraint. AMC is conceived to enhance spectral efficiency while satisfying a predefined target error rate performance. In practice, AMC techniques utilize robust

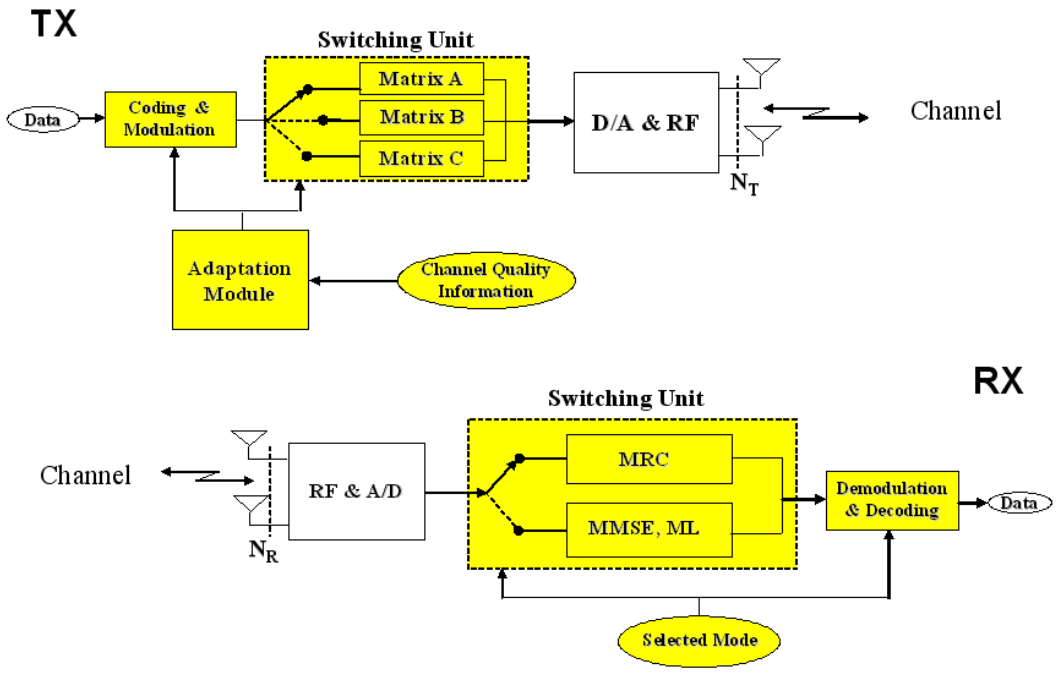

Figure 7.3: Block diagram of adaptive MIMO communication systems.

MCSs when the channel experiences deep-fades, and switch to higher order MCSs as the channel quality improves. In MIMO systems, the spatial components of the channel can be exploited via switching between different transmission schemes. A general criterion is to employ robust diversity schemes for channels with high spatial correlation, whereas transmit parallel streams via multiplexing in spatially selective channels to enhance throughput.

To gain intuition on this throughput-based adaptive mechanism, we consider three practical channel scenarios in the context of WMANs. The first scenario is characterized by one strong line-of-sight (LOS) component and no scattering. Since the channel has only one dominant spatial component, the

Channel scenario	**Low SNR**	**Medium SNR**	**High SNR**
LOS, High CSC	Matrix A	Matrix A	Matrix B
LOS, Low CSC	Matrix A	Matrix A	Matrix B
NLOS, High CSC	Matrix A	Matrix B	Matrix C
NLOS, Low CSC	Matrix A	Matrix B	Matrix C

Table 7.3: Selected MIMO transmission schemes in different channel scenarios and SNR conditions. Each propagation scenario is characterized by given channel spatial correlation (CSC) and line-of-sight (LOS) component. The following SNR regions are considered: Low SNR ($<$ 15 dB), Medium SNR ($\simeq$ 20 dB) and High SNR ($>$ 25 dB).

user would be starved of diversity and robust schemes (i.e., Matrix A) would be selected by the adaptive algorithm. The second channel scenario is poor scattering environment (i.e., non-LOS and low angular spread), in which only few degrees of freedom are available to transmit parallel streams over the wireless link. In this case, the user would require hybrid schemes (i.e., Matrix B) to enhance throughput, while maintaining good error rate performance. The third channel scenario is a rich scattering environment (i.e., high angular spread), for which adaptive MIMO algorithms would switch to multiplexing transmissions (i.e., Matrix C) to increase spectral efficiency.

As for conventional AMC schemes, the choice of the optimal MIMO transmission scheme depends also on the signal-to-noise ratio (SNR). For example, users at the edge of the cell would be served with diversity schemes as opposed to users close to the access point for which multiplexing schemes would be preferable. Table 7.3 summarizes the MIMO schemes to be used in different channel scenarios and SNR conditions.

In practical adaptive switching systems, MIMO schemes are used in combination with MCSs, to enable transmissions over the wireless link. In Table 7.2 we listed the set of 24 available MIMO transmission modes for 4×4 systems. In practice it is desirable to reduce the number of modes to keep the number of control bits to a minimum. One solution is to discard modes that provide the same throughput for worse error rate performance. For example, Fig. 7.4 shows that mode 15 in Table 7.2 yields the same spectral efficiency as mode 14 for higher SNR requirement (due to worse BER). Then, the number of modes in Table 7.2 would be reduced down to sixteen, such that the control information can be encoded over four bits. In systems with low-rate control channels, it is possible to further reduce the number of modes down to eight as depicted in Fig. 7.4, such that only three bits would be required for the control messages.

Given the set of MIMO transmission modes, the challenge now is to design methods to switch between modes depending on the channel conditions. The general criterion of throughput-based adaptive algorithms is to select the mode that yields the highest throughput while satisfying a predefined target error rate. This adaptive method requires knowledge of the error rate performance of each mode, which is also a function of the channel quality in the time, frequency and space domains. For example, the average BER of spatial multiplexing modes (i.e., modes 12, 15, 17, 19, 21-24 in Table 7.2) is much higher in spatially correlated channels than spatially selective channels. One way to estimate the error performance of different modes is to express their

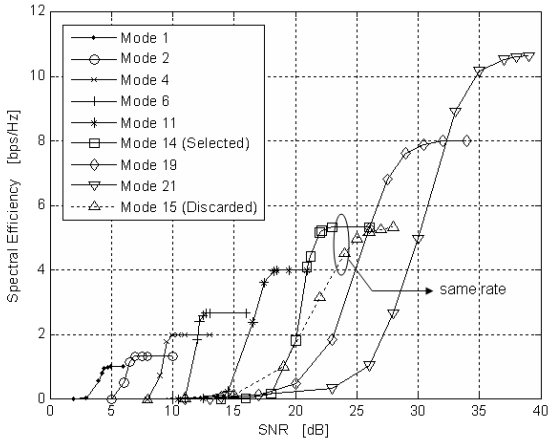

Figure 7.4: Spectral efficiency of different MIMO modes in Table 7.2 (defined as combinations of MCSs and MIMO schemes) for practical 4×4 MIMO systems.

BER in closed-form as a function of the channel parameters for bit-interleaved coded modulation (BICM) systems, as proposed in [174]. Unfortunately, these closed-form expressions are not available for all kind of channels (i.e., with LOS) and MIMO transceivers.

An alternative method is to empirically pre-compute the error performance of the transmission modes for a set of "typical" propagation scenarios or *link-quality regions*. The link quality regions are defined by quantized levels of time/frequency/space correlation and SNR values. Then, the optimal *SNR switching thresholds*, corresponding to the predefined target error rate, are stored for different modes in look-up tables (LUTs). A general method to generate the LUTs was described in [127] by accounting for the time and frequency selectivity of the channel. For spatially selective channels, the LUT

can be constructed based on quantized spatial correlation scenarios as reported in Table 7.3.

In practical adaptive MIMO systems, the receiver first calculates the *link-quality metrics*, consisting of average SNR and time/frequency/space selectivity indicators [2, 127]. These metrics are then input into the LUT, that maps the link-quality metrics into a link-quality region. Then, the average SNR is compared against the available SNR thresholds of the selected channel scenario to choose the optimal transmission mode, providing the highest throughput for the predefined target error rate. The mode-selection information is then conveyed to the transmitter via a reliable low-rate feedback channel. This adaptive mechanism can be carried out on a frame-by-frame basis, by tracking the instantaneous channel quality. Alternatively, long-term adaptation can be employed to reduce the amount of control information, resulting in lower throughput performance.

7.3.2 Diversity-Based Adaptive Methods

The goal of diversity-based adaptive methods is to improve the error rate performance of wireless systems, resulting in higher robustness to fading and increased coverage. Diversity-based methods are enabled by switching between different MIMO modes to reduce error rate for fixed data rate transmissions. To achieve the same data rate with different transmission modes, different MCSs are employed for the three MIMO schemes described above. For example, in Table 7.2 diversity-based methods can be applied to the fol-

lowing sets of modes characterized by the same values of peak spectral efficiency: $\{4, 5\}$, $\{6, 7\}$, $\{8, 9\}$, $\{10, 11, 12\}$, $\{14, 15\}$, $\{16, 17\}$ and $\{18, 19\}$. As for throughput-based methods, the adaptation can be carried out at fast or slow rates.

One solution for instantaneous diversity-based adaptations was proposed in [152, 175]. In [152] an algorithm based on the minimum Euclidean distance was designed to switch between diversity and multiplexing schemes for 2×2 MIMO systems. Similar method was presented in [175] for 4×4 MIMO systems, enabling switching between Matrix A, B and C. These methods, however, are based on theoretical bounds, yielding performance loss especially for large number of transmit antennas. Moreover, the computational complexity at the receiver is high, since the minimum Euclidean distance has to be calculated on a frame-by-frame basis.

Alternatively, a stochastic approach can be employed as in [175]. In this case, the error rate performance is pre-computed for different transmission modes and the optimal SNR switching thresholds are stored in LUTs for different propagation conditions, similarly to the throughput-based method. Then, the receiver estimates the channel quality and selects the mode yielding the lowest BER performance for a fixed error rate. As case-study, we consider the following three MIMO modes without FEC coding for simplicity: Mode A, with 256QAM and Matrix A; Mode B, with 16QAM and Matrix B; Mode C with 4QAM and Matrix C. All three modes are characterized by the same peak spectral efficiency value of 8 bps/Hz.

7.3.3 Joint Diversity/Throughput-Based Adaptive Methods

We showed that adaptive MIMO transmission methods can be designed either to increase throughput or provide diversity gains. For both these approaches we selected only a subset of modes from Table 7.2 to reduce the number of bits used for control information. Alternatively, it is possible to employ the whole set of modes in Table 7.2 in a joint diversity/throughput-based adaptive algorithm. In this case, the throughput-based method would be employed to enhance spectral efficiency for predefined target error rate, by switching to modes with higher data rates depending on the estimated link-quality region. Moreover, within each link-quality region, the joint adaptive algorithm switches between modes with same rate but different error rate performance to yield additional diversity gains, resulting in higher spectral efficiency.

7.4 Adaptation Based on Lookup Tables

In the preceding section, we demonstrated significant theoretical capacity gains offered by the proposed low complexity adaptive MIMO approach, and also identified the important factors from a switching point of view. We now propose a novel algorithm for switching between the low complexity transmission schemes in a practical wireless communication system. The goal of our algorithm is to maximize the system spectral efficiency for a predefined target bit error rate (BER).

7.4.1 MIMO Transmission Modes

Our adaptive switching algorithm operates according to a set of *modes*, with each mode comprising a particular low complexity MIMO transmission technique and a modulation/coding scheme (MCS). The MIMO transmission schemes we consider include statistical BF, D-STTD with MMSE receivers, and SM with MMSE receivers. We consider the eight MCS combinations defined by the IEEE 802.11a standard [176]. The 3 MIMO transmission schemes and the 8 MCS combinations yield a total of 24 different transmission modes, from which we select a subset of 12 (including a *no transmission* mode, for cases where the target error rate is not satisfied by any of the other selected modes).

7.4.2 Link-quality Regions and Metrics

Motivated by the results of Section 5.4, our proposed practical mode selection (or switching) algorithm is based on average SNR and channel correlation (eigenvalue) parameters. Unfortunately, defining switching criterion (i.e. a set of SNR switching thresholds, see below) for every channel correlation scenario is an infeasible solution. As such, our practical approach is to define a set of "typical" channel scenarios, and to pre-compute the error rate performance of the transmission modes for each scenario. The typical channel scenarios we consider are detailed in Table 7.4, with parameters K and N_c corresponding to the Rician K-factor in (2.5) and the number of scatterer clusters, respectively. These were selected based on the IEEE 802.11n

Scenario	Channel Type	Spatial Parameters	D_λ
1	NLOS, High AS	$K = -\infty$ dB, AS $\in [28^o, 55^o]$, $N_c = 6$	[1,5.5)
2	NLOS, Low AS	$K = -\infty$ dB, AS $\in [22.4^o, 24.6^o]$, $N_c = 2$	[5.5,25.8)
3	LOS, Low K	$K = 2$ dB, AS $\in [22.4^o, 24.6^o]$, $N_c = 2$	[25.8,85.8)
4	LOS, High K	$K = 6$ dB, AS$= 30^o$, $N_c = 1$	[85.8,+ inf)

Table 7.4: Typical channel scenarios used by our practical adaptive switching algorithm and corresponding values of the link-quality metric (D_λ).

models [43], and correspond to channels with widely varying degrees of spatial selectivity. For more details, see [2].

For each typical channel scenario we associate a corresponding set of SNR thresholds, which together define the *link-quality regions* used for mode selection. To predict the link-quality region for a given transmission we employ two *link-quality metrics*: the average SNR, and the relative condition number (D_λ) of the spatial correlation matrices. The relative condition number is a function of the eigenvalues of the spatial correlation matrices, as discussed in [2], and is an indicator of the channel spatial-selectivity.

7.4.3 Generating the Look-up Table

The mode selection information, corresponding to the set of link quality regions, is stored in a look-up table (LUT). To generate the LUT, we simulate the error-rate performance of the 24 transmission modes in the 4 typical channels scenarios, and in each case determine the *SNR thresholds* corresponding to a pre-defined target error rate. For each channel scenario, we then select a subset of the 12 modes providing increasing transmission rates with the lowest

SNR thresholds. The SNR thresholds corresponding to the selected modes for each channel scenario are then stored in the LUT.

7.4.4 Switching Algorithm Operation

Once the LUT is constructed, our proposed practical switching algorithm operates as follows. The receiver first calculates the link quality metrics by measuring the average SNR and the relative condition number (D_λ) of the channel spatial correlation matrices. These metrics are then input into the LUT, which maps the link-quality metrics into a link-quality region. In particular, D_λ is used to select the channel scenario, according to the empirically derived values reported in Table 7.4. Then, the average SNR is compared against the SNR thresholds of the selected channel scenario to choose the optimal transmission mode, providing the highest throughput for the predefined target error rate. The mode-selection information is then conveyed to the transmitter via a reliable low-rate feedback channel.

Note that the switching criterion is derived from the channel statistics (i.e., average SNR and spatial correlation) rather than instantaneous channel state information. As such, the proposed method tracks the long-term channel variations (due to shadowing, path-loss, or different correlation scenarios), hereby reducing the amount of feedback required for the adaptive mode switching. Also, since it is based on statistical knowledge, the algorithm is inherently more robust to practical effects such as imperfect channel estimation and feedback delays.

7.4.5 Simulation Results

For the following simulation results we assume a 4×4 MIMO system and a target BER of 0.05. Fig. 7.5 shows the BER versus SNR curves for each of the transmission modes for typical channel Scenario 4 in Table 7.4. The BER performance of the adaptive scheme is shown by the thicker solid line. As the SNR is increased, modes with increasing levels of spectral efficiency are selected. We clearly see that in all cases the BER of the adaptive scheme remains below the predefined target, as required.

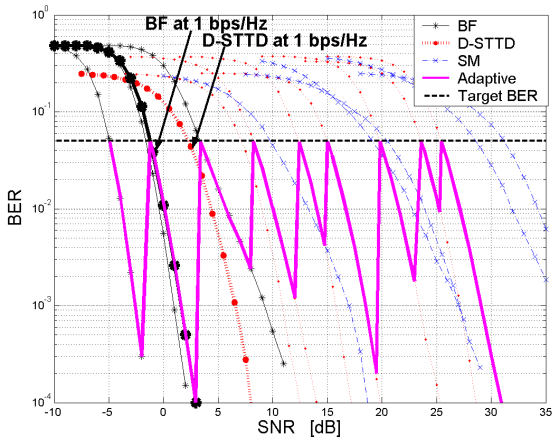

Figure 7.5: Bit error rate (BER) of the adaptive MIMO transmission scheme versus fixed BF, D-STTD and SM with different MCS, in channel Scenario 4.

Fig. 7.6 compares the spectral efficiency of the proposed adaptive algorithm, with that of fixed BF, D-STTD, and SM transmission schemes employing adaptive MCS. Results are presented in typical channel Scenarios 3, as defined in Table 7.4. We see that, for high SNR, the proposed adaptive

algorithm yields a spectral efficiency gain of 11 bps/Hz over a non-adaptive BF scheme. We emphasize that the BER for the adaptive scheme remains below the predefined target for all levels of spectral efficiency. Note that the low performance of statistical BF in this case is due to the presence of multiple clusters for channel Scenario 3, which prevents the channel from having one dominant spatial direction in narrowband systems. In broadband systems, where multiple taps are distinguishable both in time and space, better performance is expected for BF.

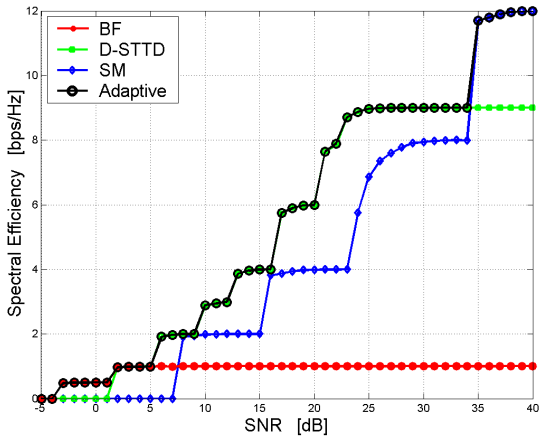

Figure 7.6: Spectral efficiency of the adaptive MIMO transmission scheme versus fixed BF, D-STTD and SM with adaptive MCS, in channel Scenario 3 in [2].

Fig. 7.7 depicts the spectral efficiency curves for the adaptive algorithm in different channel scenarios. It is possible to see that in low SNR regime the spectral efficiency improves from Scenario 2 to 4 in Table 7.4 due to the increasing channel spatial correlation that yields better performance for BF.

Vice versa, for SNR higher than 5 dB the throughput provided by the adaptive algorithm tends to decrease from Scenario 2 to 4, since the performance of D-STTD and SM degenerates as the spatial correlation increases.

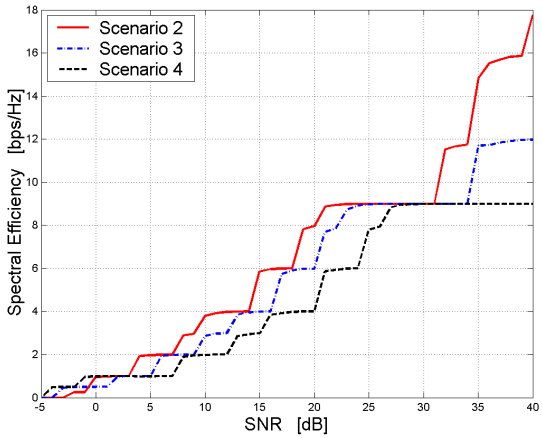

Figure 7.7: Spectral efficiency of the adaptive MIMO transmission scheme in different channel scenarios.

7.5 Adaptation Based on Closed-form BER with BICM

In this section we present a novel low complexity switching strategy for BICM mode and MIMO transmission scheme selection. Our proposed switching strategy is based purely on the analytical results of the previous two sections, and does not require any empirically-generated lookup tables. The approach is shown to yield significant improvements in system throughput for the transmit and receive correlated Rayleigh channels we are considering.

7.5.1 BER Performance Comparison in Correlated Channels

Before presenting the details of the adaptive strategy, we first investigate the relative performance of BICM-SB and BICM-ZF in various correlation scenarios.

Fig. 7.8 considers 2×2 fully-interleaved systems, and shows BER curves based on the C-PEP expressions (6.34) for BICM-SB, and (6.56) for BICM-ZF, which have previously been shown to be tight. For the 2 bits/s/Hz case, BICM-SB operates with the 1/2 rate code discussed in Section 6.4.4 (and used throughout this paper) and 16QAM, and BICM-ZF operates with the 1/2 rate code and QPSK. For the 4 bits/s/Hz case, BICM-SB operates with a 2/3 rate code (obtained by puncturing the 1/2 rate code above, as outlined in [177]) and 64QAM, whereas BICM-ZF operates with the 1/2 rate code and 16QAM.

As expected, we observe that BICM-ZF degrades with increasing transmit correlation. In contrast, the BER of BICM-SB *improves* with increasing transmit correlation. This improvement is due to more energy being focused in the direction of the SB vector $\mathbf{u}_{\mathrm{s,max}}$, yielding an SNR gain. The relative performance is of course the important factor in designing a switching scheme, and this is highly influenced by the correlation and the spectral efficiency. The figure shows that for 2 bits/s/Hz, BICM-SB outperforms BICM-ZF in both correlation scenarios. At 4 bits/s/Hz however, BICM-SB is best for $\rho_{\mathrm{tx}} = 0.7$, and BICM-ZF is best for $\rho_{\mathrm{tx}} = 0.3$.

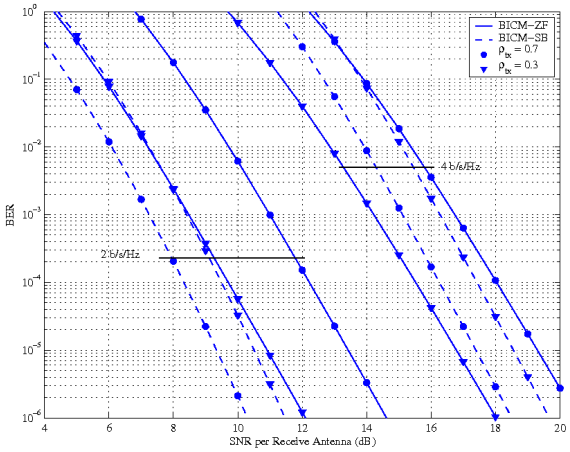

Figure 7.8: BER curves based on the tight C-PEP expressions (6.34) and (6.56) for 2×2 BICM-SB and BICM-ZF respectively. Two exponential correlated channel scenarios are presented, with $\rho_{\text{rx}} = 0.1, \rho_{\text{tx}} = 0.3$, and $\rho_{\text{rx}} = 0.1, \rho_{\text{tx}} = 0.7$.

Fig. 7.9 examines in more detail the relative performance of BICM-SB and BICM-ZF as a function of transmit correlation. The figure shows the minimum required SNR (or *SNR threshold*) to achieve a BER of 10^{-3} for the 4 bits/s/Hz systems considered in Fig. 7.8. The curves were evaluated using C-PEP expressions as in Fig. 7.8. Note that, even if one wanted to, it is infeasible to accurately generate these curves in a practical time-frame via simulation, since they require inverting the BER versus SNR curves. Hence our tight efficient analytical expressions are particularly useful here. Results are presented as a function of ρ_{tx}, for three example correlated channels with $\rho_{\text{rx}} = 0.1$, 0.5, and 0.9. Clearly the ZF scheme requires increasing SNR to achieve the target BER as the transmit correlation increases. The reverse is

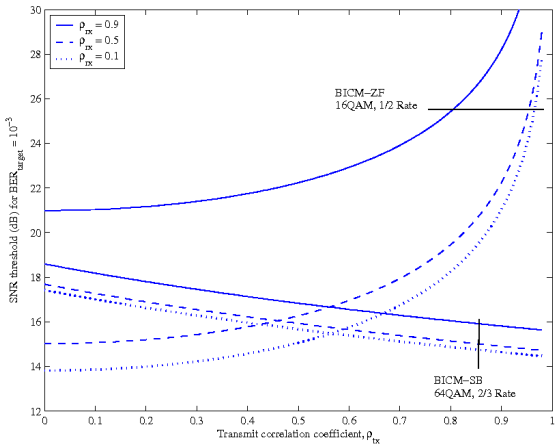

Figure 7.9: SNR thresholds corresponding to a target BER of 10^{-3} for BICM-ZF and BICM-SB as a function of ρ_{rx} and ρ_{tx}. Results are shown for 2×2 BICM-ZF with 16QAM and a 1/2 rate code, and BICM-SB with 64QAM and a 2/3 rate code.

true for the SB scheme. The important observation from a switching algorithm point of view, is that the curves can cross. For example, for receive correlation $\rho_{\text{rx}} = 0.1$, it is clearly desirable to use BICM-ZF for $\rho_{\text{tx}} \leq 0.55$, and to use BICM-SB for $\rho_{\text{tx}} > 0.55$. Another interesting observation is that both SB and ZF are negatively affected by increasing receive correlation. This is particularly significant for ZF.

7.5.2 Analytical BICM Switching Scheme

Clearly there are significant benefits to be gained from switching between BICM-ZF and BICM-SB depending on the channel correlation and the SNR. We now propose a low complexity practical switching algorithm to max-

imize system throughput whilst satisfying a predefined BER.

The throughput ν is calculated for a given BICM mode and MIMO transmission scheme using

$$\nu = S\,(1 - \mathrm{BER}) \tag{7.1}$$

where S is the spectral efficiency. For a given mode, the spectral efficiencies are calculated for the SB and ZF transmission schemes according to (6.2) and (6.3) respectively.

In general terms, we follow a standard adaptive procedure whereby the receiver first estimates channel parameters, then calculates which mode will yield the highest throughput, and then conveys that information to the transmitter via a reliable low-rate feedback link. A key novelty of our scheme is that we perform switching based on the channel spatial correlation matrix eigenvalues, and that we switch between the MIMO transmission schemes (SB and ZF) as well as coding and modulation formats. It is the new closed-form BER expressions of the previous sections which make this possible.

7.5.3 Switching Between SB and SM

In this section, we consider 2×2 systems, and employ the eight BICM modes defined by the IEEE 802.11a standard in [177]. Note, however, that our algorithm applies equally to any antenna configuration, and for any set of modes comprising Gray-labeled modulation formats.

Fig. 7.10 shows throughput results for a target BER of 10^{-3}, and for

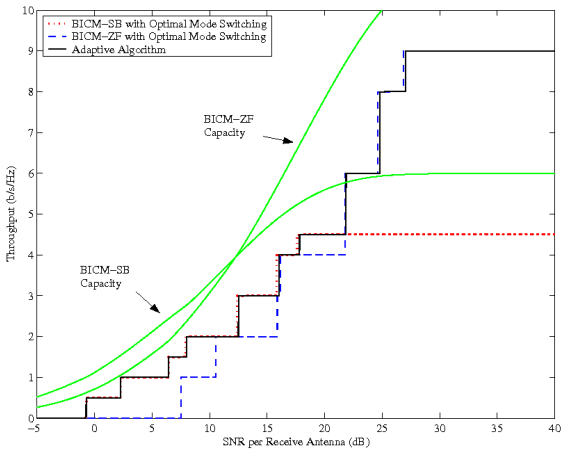

Figure 7.10: Throughput achieved by the proposed adaptive algorithm for a 2×2 system with target BER of 10^{-3}, and for correlated channels with $\rho_{\text{rx}} = \rho_{\text{tx}} = 0.5$. Mode and transmission scheme selection is based on the tight C-PEP expressions (6.34) and (6.56). Throughputs with optimal mode selection, and LLC envelope curves, are also given.

correlated channels with $\rho_{\text{rx}} = \rho_{\text{tx}} = 0.5$. The figure shows the throughputs obtained by BICM-SB and BICM-ZF with optimal mode switching, where the switching points are calculated based on the actual simulated BER curves. For comparison, LLC envelope curves (as derived in Section 6.2), are also shown. The solid line in the figure corresponds to our proposed adaptive selection algorithm, where the switching points are based on the tight C-PEP expressions (6.34) and (6.56) for BICM-SB and BICM-ZF respectively. Clearly our approach achieves near-optimal throughputs for all SNR. As expected, BICM-SB is selected for low SNRs, and BICM-ZF is selected for high SNRs.

Fig. 7.11 shows the throughputs of the proposed adaptive algorithm in

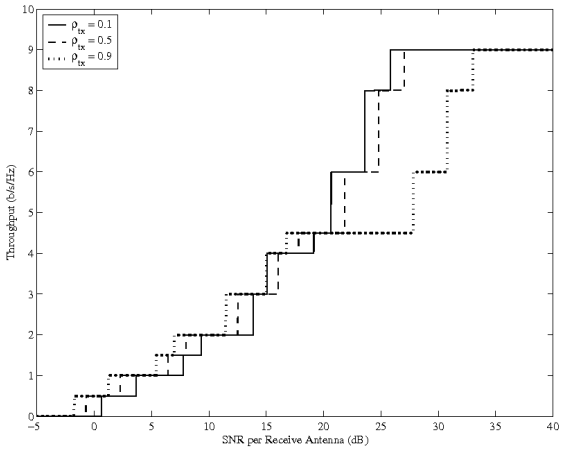

Figure 7.11: Throughputs achieved by the proposed adaptive algorithm for a 2×2 system with target BER 10^{-3}, in different exponential correlated channel scenarios, with $\rho_{\text{rx}} = 0.5$, and ρ_{tx} values of $0.1, 0.5$ and 0.9. Mode and transmission scheme selection is based on the tight C-PEP expressions (6.34) and (6.56).

various transmit correlation scenarios. For SNRs below 20 dB, the throughputs improve with increasing transmit correlation, since BICM-SB was selected by the adaptive algorithm in this low SNR regime. Conversely, for SNRs above 20 dB, the adaptive algorithm selected BICM-ZF, and hence the throughput degrades with increasing transmit correlation.

Fig. 7.12 compares the selection algorithm based on the tight C-PEP expressions (6.34) and (6.56), with the selection algorithm based on the simplified C-PEP expressions (6.36) and (6.60). The figure includes throughput curves corresponding to optimal switching based on actual simulated BERs. We see that for a target BER of 10^{-3}, both algorithms perform very close to

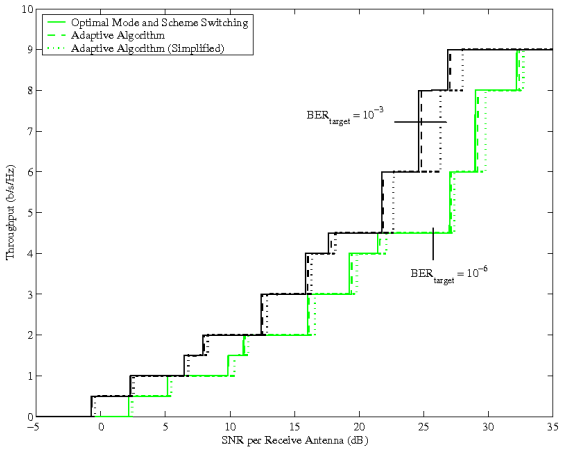

Figure 7.12: Throughput comparison of two mode/transmission scheme selection approaches. The first is based on the tight C-PEP expressions (6.34) and (6.52), the second is based on the simplified expressions (6.36) and (6.59). Results are shown for 2×2 systems with targets BERs 10^{-3} and 10^{-6}, and for channels with $\rho_{\text{rx}} = \rho_{\text{tx}} = 0.5$.

the optimal curve for SNRs ≤ 20 dB. For SNRs above this, the simplified algorithm incurs a noticeable loss. At the lower target BER of 10^{-6}, the simplified algorithm performs close to the optimal curves for *all* SNRs. This is because in this region the ZF scheme is chosen, and the C-PEP expression (6.60) is tighter at this target BER, in comparison to 10^{-3}, as seen from Fig. 6.5. This yields more accurate SNR thresholds for all BICM-ZF modes, thereby improving the throughput achieved by the simplified algorithm when these modes are employed (i.e. in the high SNR regime).

7.5.4 Switching Between OSTBC and SM

We now propose an adaptive MIMO transmission algorithm based on theoretical BER expressions we have just derived. The algorithm switches between BICM-OSTBC and BICM-SM and exploits the statistical channel information (i.e., average SNR and channel spatial correlation). To enable transmission over the wireless link we define a set of transmission *modes*, which are combinations of modulation/coding schemes (MCSs) and MIMO transmission techniques (i.e., OSTBC or SM). We use the eight MCSs proposed in the IEEE 802.11a standard for wireless local area networks, with increasing values of data rate (R). The key idea of the algorithm is to compute the theoretical BER for given channel condition and select the transmission mode that yields the highest spectral efficiency while satisfying a predefined target BER.

Fig. 7.13 depicts the theoretical BER performance of different modes in double-sided spatially correlated channels, with $\rho_{\text{tx}} = 0.1$ and $\rho_{\text{rx}} = 0.05$. The curves with circles represent the BER for the eight MCSs with BICM-OSTBC derived from (6.43), and the curves with stars refer to the closed-form BER expression of BICM-SM in [3]. The performance of the adaptive algorithm with predefined target BER of 10^{-6} is depicted with the solid curve. It is possible to see that, for given transmit/receive spatial correlation, as the SNR increases the proposed adaptive method switches to the higher order modes to enhance the spectral efficiency while satisfying the predefined target BER. Note that in Fig. 7.13 we applied the adaptive algorithm to the theoretical BER in (6.43) and [3], rather than empirical BER derived from simulations.

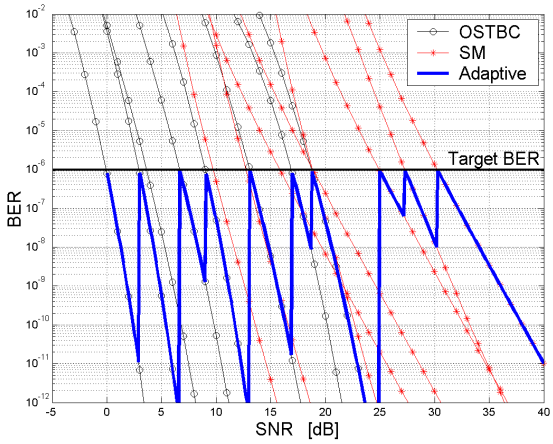

Figure 7.13: BER performance for adaptive MIMO 2x2 systems. The BER of OSTBC and SM are obtained from the approximations in (6.43) and [3], respectively. The exponential model is used, with $\rho_{\text{tx}} = 0.1$ and $\rho_{\text{rx}} = 0.05$.

In practical systems, the switching thresholds can be empirically adjusted to compensate for the small SNR gap between theoretical and simulated BER curves shown in Fig. 6.4.

Next, we show the performance of the proposed method in terms of spectral efficiency, $R(1 - \text{BER})$, for the same target BER of 10^{-6}. We simulated the propagation channel according to the COST-259 physical channel model [4] and assumed uniform linear array (ULA) configuration with half-wavelength element spacing both at the transmitter and receiver. Two different radio environments are simulated: pico-cell with generalized office line-of-sight (GOL) defined with 8 clusters and random generated AS and AOA/AOD; macro-cell with generalized typical urban (GTU) defined with single cluster, AS= 10^{o} and angle of arrival/departure of = 0^{o} (i.e., broadside directions).

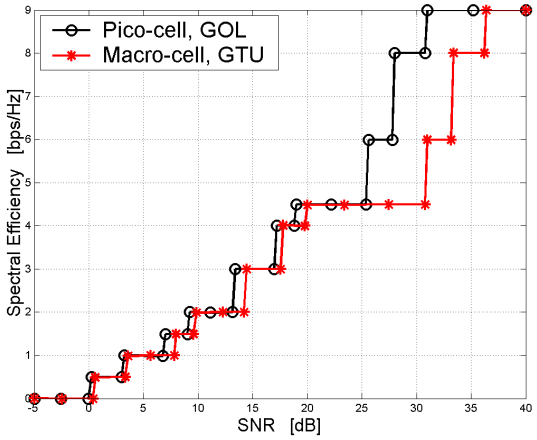

Figure 7.14: Spectral efficiency for adaptive MIMO 2x2 systems in different propagation scenarios. The MIMO channel is simulated according to the COST-259 physical channel model [4]. Two channel environments are considered: "Pico-cell, GOL" and "Macro-cell, GTU".

The transmit/receive spatial correlation matrices are computed by averaging the instantaneous MIMO channel over time. Fig. 7.14 shows that in high SNR regime our proposed adaptive MIMO algorithm doubles the spectral efficiency of conventional systems employing adaptive MCSs with fixed OSTBC transmission scheme. It is possible to see that the performance of the adaptive algorithm is better in "Pico-cell, GOL" due to the higher number of clusters that yield lower spatial correlation.

7.6 Practical Implementation Issues

In the design of practical adaptive MIMO systems the following issues need to be considered.

- When the adaptation module is at the transmit side, the receiver needs to communicate the link-quality metrics (i.e., average SNR and time/frequency/space selectivity indicators) to the transmitter, resulting in higher feedback overhead. Alternatively, the adaptation module can be designed at the receiver such that only the average SNR is fed back to the transmitter. This approach, however, results in high-complexity receiver for the user terminal.

- Real time implementations of the proposed adaptive algorithms exploiting the channel spatial selectivity are constrained by the time required to obtain reliable estimates of the channel spatial correlation matrix. Through numerical simulations, we observed that at least ten independent channel samples are needed to estimate the channel spatial correlation with minimal error. In temporally correlated channels, this condition of independence is achieved when the channel is sampled at rates of the order of twice the maximum Doppler frequency of the channel (i.e., sampling period of approximately one channel coherence time). For example, in indoor propagation environments as for WLANs, the typical Doppler spread at the carrier frequency 2.4 GHz is of the order of 3 Hz, corresponding to channel coherence time of ~ 0.1 seconds [43]. In this channel condition, the time required to obtain reliable estimates of the channel spatial correlation matrix is approximately one second. Note that the one-second time period is required only to initialize the estimate of the channel spatial correlation matrix, while successive estimates can

be carried out via recursive algorithms with forgetting factor. Hence, one solution for practical implementations of the proposed adaptive methods is to initialize the algorithm with a robust transmission mode and enable the adaptive switching to higher order modes when reliable correlation estimates are available (i.e., after the one-second time period). We observe that the adaptation rate of the MIMO transmission modes can be larger than the rate of adaptation of the channel spatial correlation matrix.

- The amount of control information sent by the transmitter to enable mode switching is a function of the adaptation rate. In general, fast adaptation results in better system performance, since the algorithm is able to track the short-term channel variations. The high number of control messages, however, may become impractical for systems with low-rate control channels or in high Doppler, and statistical adaptation may be preferable.

- To pre-compute the LUTs for throughput-based adaptive methods via simulations may be computationally expensive. One way to reduce this complexity is to rely on theoretical performance analysis of BICM MIMO systems [174] and empirically derive from that the SNR switching thresholds for different link-quality regions.

- The IEEE 802.16e standard provides the option for precoding transmissions, based on quantized channel information or limited feedback tech-

niques. The adaptive algorithms described above can be easily extended to switching between different closed-loop schemes, yielding better BER performance and higher spectral efficiency, at the expense of larger number of feedbacks required for the precoders.

- Spatial multiplexing modes require high SNR to be selected by the adaptive algorithm, as shown in Table 7.4. In indoor environments (as for wireless local area netwroks), when the users are close to the access point (i.e., high SNR condition) and in presence of rich scattering, adaptive switching to multiplexing mode is a practical solution to increase system throughput. On the other hand, in outdoor scenarios (as for typical cellular systems) the distribution of the SNR is centered at low values due to the adverse effect of the path loss and presence of users at the edge of the cell [178]. In these conditions, adaptive MIMO algorithms may not provide satisfactory throughput performance, and other solutions such as precoding schemes for multi-user MIMO systems may be better way to increase the spectral efficiency.

Chapter 8

Conclusions

In this dissertation novel MIMO antenna and algorithm design methodologies to exploit the channel spatial selectivity are presented. The current state of research in the area of antenna design and adaptive physical layer transmission techniques for MIMO communication systems is first reviewed. Current developments treat antenna and algorithm design independently. The goal of this dissertation is to propose new methodologies and solutions for MIMO antenna and algorithm designs that exploit metrics from different layers to enhance system performance in spatially correlated channels. The proposed antenna array design employs metrics from microwave and communication theory, and exploits pattern diversity to reduce the channel spatial correlation. The proposed adaptive algorithm is designed to switch between different MIMO transmission schemes as a function of the channel spatial correlation to enhance spectral efficiency.

8.1 Summary

A compact MIMO array design exploiting pattern diversity is first proposed. It is shown through analysis and simulations that pattern diversity may

yield better performance than space diversity, enabling more compact array designs. This dissertation also proposed a new methodology to design MIMO arrays by jointly optimizing antenna theory and communication theoretical performance metrics.

The performance of MIMO arrays and transmission schemes vary as a function of the propagation environment. This dissertation described a novel adaptive technique to switch between different MIMO transmission schemes, based on the channel statistics (i.e., average SNR and spatial correlation), as a means to enhance systems performance.

Both these research topics propose new ideas and advances in the design of wireless communication systems. The proposed antenna design methodology will enable compact and robust array solutions suitable for future wireless devices with limited size constraints. The adaptive transmission method will enable efficient use of the spectrum, resulting in larger data rate, in future wireless multiple-antenna systems.

8.2 Future Work

This dissertation presented analysis and practical solutions for MIMO antenna and adaptive algorithm designs. Future work in this research area may address the following topics:

Miniaturized designs of MIMO arrays exploiting pattern diversity: the proposed MIMO array design can be further miniaturized to satisfy more

restrictive size constraints of wireless communication devises. Possible solutions are printed circuit board (PCB) or planar inverted-F antennas (PIFAs) [115, 179, 180]. The analysis on pattern diversity presented in this dissertation provides useful guidelines for these miniaturized designs exploiting pattern diversity. Moreover, the proposed cross-layer design methodology can be used to optimize the design of these arrays.

Reconfigurable MIMO arrays: one active research area is reconfigurable antennas with micro-electro-mechanical system (MEMS) switches [181–184] or other switching solutions [185–187], where the antenna radiation pattern can be adaptively reconfigured. Our proposed analysis and design methodology for MIMO arrays exploiting pattern diversity can be used to optimize the design of reconfigurable antennas. Additionally, the proposed capacity/BER analysis and algorithm designs can be extended to define adaptive switching criteria for reconfigurable arrays.

Multiuser MIMO: the adaptive MIMO algorithm presented in this dissertation is for point-to-point communications. In the context of multiuser systems, the proposed analysis and algorithm designs can be extended to enable different types of services (whether through diversity or multiplexing transmissions) to different users, depending on their propagation environment and distance from the centralized transmitter.

Appendices

Appendix A

Proof on the Post-Processing SNR of D-STTD

Using $\mathcal{H}$ in (5.40), we define

$$\mathbf{C} \triangleq \mathcal{H}^{\dagger}\mathcal{H} = \begin{bmatrix} c_1 & 0 & c_3 & c_4 \\ 0 & c_1 & -c_4^* & c_3^* \\ c_3^* & -c_4 & c_2 & 0 \\ c_4^* & c_3 & 0 & c_2 \end{bmatrix} \tag{A.1}$$

where

$$c_1 = \sum_{m=1}^{N_r}(|h_{m,1}|^2 + |h_{m,2}|^2) \qquad c_2 = \sum_{m=1}^{N_r}(|h_{m,3}|^2 + |h_{m,4}|^2) \tag{A.2}$$

$$c_3 = \sum_{m=1}^{N_r}(h_{m,1}^* h_{m,3} + h_{m,2}h_{m,4}^*) \qquad c_4 = \sum_{m=1}^{N_r}(-h_{m,1}^* h_{m,4} + h_{m,2}h_{m,3}^*) \tag{A.3}$$

We now show that the first two diagonal entries of $\mathbf{C}^{-1}$ are equal to each other, and so are the last two diagonal entries. This in turn would mean that in (5.48), we have $\gamma_1 = \gamma_2$ and $\gamma_3 = \gamma_4$.

Note that $\mathbf{C}$ in (A.1) can be written in a partitioned form as

$$\mathbf{C} = \begin{bmatrix} c_1\mathbf{I} & \mathbf{B} \\ \mathbf{B}^{\dagger} & c_2\mathbf{I} \end{bmatrix} \tag{A.4}$$

with

$$\mathbf{B} \triangleq \begin{bmatrix} c_3 & c_4 \\ -c_4^* & c_3^* \end{bmatrix}. \tag{A.5}$$

Observe that the matrix $\mathbf{B}$ is orthonormal, and

$$\mathbf{B}\mathbf{B}^\dagger = \{|c_3|^2 + |c_4|^2\}\mathbf{I} = \mathbf{B}^\dagger\mathbf{B}. \tag{A.6}$$

The inverse of $\mathbf{C}$ clearly exists and using the formula for the inverse of partitioned matrices [146] is given by

$$\begin{aligned}
\mathbf{C}^{-1} &= \begin{bmatrix} \left(c_1\mathbf{I} - \frac{1}{c_2}\mathbf{B}\mathbf{B}^\dagger\right)^{-1} & \frac{1}{c_1}\mathbf{B}\left(\frac{1}{c_1}\mathbf{B}^\dagger\mathbf{B} - c_2\mathbf{I}\right)^{-1} \\ \frac{1}{c_1}\left(\frac{1}{c_1}\mathbf{B}^\dagger\mathbf{B} - c_2\mathbf{I}\right)^{-1}\mathbf{B}^\dagger & \left(c_2\mathbf{I} - \frac{1}{c_1}\mathbf{B}^\dagger\mathbf{B}\right)^{-1} \end{bmatrix} & \text{(A.7)} \\
&= \begin{bmatrix} \left(c_1 - \frac{(|c_3|^2+|c_4|^2)}{c_2}\right)^{-1}\mathbf{I} & \frac{1}{c_1}\left(\frac{(|c_3|^2+|c_4|^2)}{c_1} - c_2\right)^{-1}\mathbf{B} \\ \frac{1}{c_1}\left(\frac{(|c_3|^2+|c_4|^2)}{c_1} - c_2\right)^{-1}\mathbf{B}^\dagger & \left(c_2 - \frac{(|c_3|^2+|c_4|^2)}{c_1}\right)^{-1}\mathbf{I} \end{bmatrix}. & \text{(A.8)}
\end{aligned}$$

Substituting (A.8) into equations (5.48) it is easy to see that $\gamma_1 = \gamma_2$, $\gamma_3 = \gamma_4$, and that the random variables γ_k (with $k = 1, \ldots, 4$) are identically distributed. The same results hold even in the case of (5.47). To see this, define $\tilde{\mathbf{C}} = \mathbf{I}_{N_t} + \frac{\gamma_o}{N_t}\mathbf{C}$ and note that $\tilde{\mathbf{C}}$ can be written in a partitioned matrix form similar to (A.4), with the corresponding submatrix of $\tilde{\mathbf{C}}$ obeying analogous relations (A.5-A.6). Hence the elements of $\tilde{\mathbf{C}}^{-1}$ will also be such that the first two diagonal elements equal each other, and so do the last two diagonal elements.

Appendix B

Derivation of Equation (6.51)

To calculate $\tilde{\mathcal{J}}'(\cdot)$ and $\tilde{\mathcal{J}}''(\cdot)$ we manipulate $\tilde{\mathcal{J}}(\cdot)$ in (6.46) as follows. We first express the inverse in the denominator of (6.46) as[1]

$$[\mathbf{I}_{N_r} + K_{k,i}(s)\mathbf{\Lambda}_r]^{-1} = \text{diag}\left(\frac{1}{1 + K_{k,i}(s)\lambda_{r,q}}\right) \tag{B.1}$$

where, for convenience, we have defined

$$K_{k,i}(s) \triangleq \frac{\gamma \mathcal{E}_{M,i} s(1-s)}{[\mathbf{S}^{-1}]_{k,k}}. \tag{B.2}$$

We also write the determinant in (6.46) as

$$|\mathbf{I}_{N_r} + K_{k,i}(s)\mathbf{\Lambda}_r| = \prod_{j=1}^{N_r} \left(1 + K_{k,i}(s)\lambda_{r,j}\right). \tag{B.3}$$

Using (B.1) and (B.3) it can be shown that

$$\tilde{\mathcal{J}}_{k,\mathcal{E}_{M,i}}(s) = \frac{\text{tr}_{N_t-1}\left(\mathbf{\Lambda}_r\right)}{\text{tr}_{N_t-1}\left(\text{diag}\left(\frac{\lambda_{r,q}}{1+K_{k,i}(s)\lambda_{r,q}}\right)\right)\prod_{j=1}^{N_r}\left(1 + K_{k,i}(s)\lambda_{r,j}\right)}. \tag{B.4}$$

We now focus on the denominator in (B.4), which we assign the function name $D(s)$. The key here is to express $D(s)$ as a polynomial in $K_{k,i}(s)$, which

[1]Here we introduce a compact notation to represent the diagonal matrix in terms of the q^{th} diagonal element.

will then allow the required derivatives to be evaluated. Expanding the e.s.f. according to (6.47) gives

$$\begin{aligned} D(s) &= \mathrm{tr}_{N_t-1}\left(\mathrm{diag}\left(\frac{\lambda_{r,q}}{1+K_{k,i}(s)\lambda_{r,q}}\right)\right)\prod_{j=1}^{N_r}(1+K_{k,i}(s)\lambda_{r,j}) \\ &= \left(\sum_{\{\underline{\alpha}\}}\prod_{j=1}^{N_t-1}\left(\frac{\lambda_{r,\alpha_j}}{1+\lambda_{r,\alpha_j}}\right)\right)\prod_{j=1}^{N_r}(1+K_{k,i}(s)\lambda_{r,j}) \\ &= \sum_{\{\underline{\alpha}\}}\prod_{j=1}^{N_t-1}\lambda_{r,\alpha_j}\left(\prod_{j=1}^{N_r-N_t+1}\left(1+K_{k,i}(s)\lambda_{r,\beta_j}\right)\right) \end{aligned} \tag{B.5}$$

where $\{\beta_1,\ldots,\beta_{N_r-N_t+1}\} = \{1,\ldots,N_r\}\backslash\underline{\alpha}$. In order to obtain a polynomial expression, we use the following generating function expansion [188]

$$\prod_{q=1}^{N}(1+ax_q) = 1+\sum_{\ell=1}^{N}a^\ell\,\mathrm{tr}_\ell\left(\mathrm{diag}(x_q)\right) \tag{B.6}$$

which gives

$$D(s) = \mathrm{tr}_{N_t-1}\left(\mathbf{\Lambda}_r\right) + \sum_{\ell=1}^{N_r-N_t+1}K_{k,i}(s)^\ell\sum_{\{\underline{\alpha}\}}\left(\prod_{j=1}^{N_t-1}\lambda_{r,\alpha_j}\right)\mathrm{tr}_\ell\left(\mathrm{diag}\left(\lambda_{r,\beta_q}\right)\right). \tag{B.7}$$

Finally, substituting $D(s)$ as the denominator in (B.4) we obtain the simplified expression

$$\tilde{\mathfrak{I}}_{k,\mathcal{E}_{M,i}}(s) = \left(1+\sum_{\ell=1}^{N_r-N_t+1}K_{k,i}(s)^\ell C_\ell(\mathbf{\Lambda}_r)\right)^{-1} \tag{B.8}$$

where we have defined the auxiliary constants

$$C_\ell(\mathbf{\Lambda}_r) \triangleq \sum_{\{\underline{\alpha}\}}\left(\prod_{j=1}^{N_t-1}\lambda_{r,\alpha_j}\right)\mathrm{tr}_\ell\left(\mathrm{diag}\left(\lambda_{r,\beta_q}\right)\right) \tag{B.9}$$

for $\ell = 1,\ldots,N_r-N_t+1$. Now, using (B.8), we easily evaluate $\tilde{\mathfrak{I}}'_{k,\mathcal{E}_{M,i}}(\hat{s})$ and $\tilde{\mathfrak{I}}''_{k,\mathcal{E}_{M,i}}(\hat{s})$, and perform some simple algebra to obtain the desired result.

Bibliography

[1] IEEE WirelessMAN, "Part 16: Air interface for fixed and mobile broadband wireless access systems," *IEEE P802.16e/D8,*, May 2005.

[2] A. Forenza, A. Pandharipande, H. Kim, and R. W. Heath Jr., "Adaptive MIMO transmission scheme: Exploiting the spatial selectivity of wireless channels," *Proc. IEEE Veh. Technol. Conf.*, vol. 5, pp. 3188–3192, May 2005.

[3] M. R. McKay, I. B. Collings, A. Forenza, and R. W. Heath Jr., "A throughput-based adaptive MIMO-BICM approach for spatially-correlated channels," *to appear in Proc. IEEE ICC*, June 2006.

[4] L. M. Correia, *Wireless Flexible Personalised Communications*, John Wiley and Sons, Inc., New York, NY, USA, 2001.

[5] "eMarketer," Mar. 2002, http://www.emarketer.com/.

[6] T. S. Rappaport, C. Na, J. Chen, H. Nam, and S. Lemo, "Broadband internet access throughout the world," Apr. 2004, http://www.fcc.gov/oet/tac/meetings_2004.html.

[7] R. Resnick, "A silicon supplier's view of broadband wireless access," Apr. 2004, http://www.fcc.gov/oet/tac/meetings_2004.html.

[8] WWiSE, "WWiSE proposal: High throughput extension to the 802.11 standard," *IEEE 802.11-04/886r0*, http://www.802wirelessworld.com:8802/, Aug. 2004.

[9] TGn Sync, "TGn sync proposal technical specification," *IEEE 802.11-04/889r0*, http://www.802wirelessworld.com:8802/, Aug. 2004.

[10] S. Nanda, R. Walton, J. Ketchum, M. Wallace, and S. Howard, "A high-performance MIMO OFDM wireless LAN," *IEEE Comm. Mag.*, vol. 43, no. 2, pp. 101–109, Feb. 2005.

[11] M. Ho, "Closed-loop MIMO framework for IEEE 802.16e (v0.1)," *IEEE S802.16x-04/Intr0*, http://www.802wirelessworld.com:8802/, Oct. 2004.

[12] A. Ghosh, D. R. Wolter, J. G. Andrews, and R. Chen, "Broadband wireless access with WiMax/802.16: current performance benchmarks and future potential," *IEEE Comm. Mag.*, vol. 43, no. 2, pp. 129–136, Feb. 2005.

[13] 3GPP Technical Specification Group Radio Access Network, "Physical layer aspects of UTRA high speed downlink packet access," *Technical Report TR25.848*, 2001.

[14] Nokia, "Closed loop MIMO with 4 Tx and 2 Rx antennas," *3GPP TSG RAN WG1 #36*, http://www.3gpp.org/, Feb. 2004.

[15] Texas Instruments, "Improved double-STTD schemes using asymmetric modulation and antenna shuffling,"
TSG-RAN WG1 #20, http://www.3gpp.org/, May 2004.

[16] D.-S. Shiu, G. J. Foschini, M. J. Gans, and J. M. Kahn, "Fading correlation and its effect on the capacity of multielement antenna systems," *IEEE Trans. Comm.*, vol. 48, no. 3, pp. 502–513, Mar. 2000.

[17] V. Pohl, V. Jungnickel, T. Haustein, and C. von Helmolt, "Antenna spacing in MIMO indoor channels," *Proc. IEEE Veh. Technol. Conf.*, vol. 2, pp. 749–753, May 2002.

[18] M. Stoytchev, H. Safar, A. L. Moustakas, and S. Simon, "Compact antenna arrays for MIMO applications," *Proc. IEEE Antennas and Prop. Symp.*, vol. 3, pp. 708–711, July 2001.

[19] K. Sulonen, P. Suvikunnas, L. Vuokko, J. Kivinen, and P. Vainikainen, "Comparison of MIMO antenna configurations in picocell and microcell environments," *IEEE Jour. Select. Areas in Comm.*, vol. 21, pp. 703–712, June 2003.

[20] Shuangqing Wei, D. L. Goeckel, and R. Janaswamy, "On the asymptotic capacity of MIMO systems with fixed length linear antenna arrays," *Proc. IEEE Int. Conf. on Comm.*, vol. 4, pp. 2633–2637, 2003.

[21] T. S. Pollock, T. D. Abhayapala, and R. A. Kennedy, "Antenna saturation effects on MIMO capacity," *Proc. IEEE Int. Conf. on Comm.*,

vol. 4, pp. 2301–2305, May 2003.

[22] M. L. Morris and M. A. Jensen, "The impact of array configuration on MIMO wireless channel capacity," *Proc. IEEE Antennas and Prop. Symp.*, vol. 3, pp. 214–217, June 2002.

[23] Liang Xiao, Lin Dal, Hairuo Zhuang, Shidong Zhou, and Yan Yao, "A comparative study of MIMO capacity with different antenna topologies," *IEEE ICCS'02*, vol. 1, pp. 431–435, Nov. 2002.

[24] A. Forenza and R. W. Heath Jr., "Impact of antenna geometry on MIMO communication in indoor clustered channels," *Proc. IEEE Antennas and Prop. Symp.*, vol. 2, pp. 1700–1703, June 2004.

[25] M. R. Andrews, P. P. Mitra, and R. deCarvalho, "Tripling the capacity of wireless communications using electromagnetic polarization," *Nature*, vol. 409, pp. 316–318, Jan. 2001.

[26] D.D. Stancil, A. Berson, J.P. Van't Hof, R. Negi, S. Sheth, and P. Patel, "Doubling wireless channel capacity using co-polarised, co-located electric and magnetic dipoles," *Electronics Letters*, vol. 38, pp. 746–747, July 2002.

[27] T. Svantesson, "On capacity and correlation of multi-antenna systems employing multiple polarizations," *Proc. IEEE Antennas and Prop. Symp.*, vol. 3, pp. 202–205, June 2002.

[28] C. Degen and W. Keusgen, "Performance evaluation of MIMO systems using dual-polarized antennas," *Proc. IEEE Int. Conf. on Telecommun.*, vol. 2, pp. 1520–1525, Feb. 2003.

[29] R. Vaughan, "Switched parasitic elements for antenna diversity," *IEEE Trans. Antennas Propagat.*, vol. 47, pp. 399–405, Feb. 1999.

[30] P. Mattheijssen, M. H. A. J. Herben, G. Dolmans, and L. Leyten, "Antenna-pattern diversity versus space diversity for use at handhelds," *IEEE Trans. on Veh. Technol.*, vol. 53, pp. 1035–1042, July 2004.

[31] L. Dong, H. Ling, and R. W. Heath Jr., "Multiple-input multiple-output wireless communication systems using antenna pattern diversity," *Proc. IEEE Glob. Telecom. Conf.*, vol. 1, pp. 997–1001, Nov. 2002.

[32] G. J. Foschini, "Layered space-time architecture for wireless communication in a fading environment when using multiple antennas," *Bell Labs Technical Journal*, vol. 1, no. 2, pp. 41–59, 1996.

[33] A. Paulraj, R. Nabar, and D. Gore, *Introduction to Space-Time Wireless Communications*, Cambridge University Press, 40 West 20th Street, New York, NY, USA, 2003.

[34] E. G. Larsson and P. Stoica, *Space-Time Block Coding for Wireless Communications*, Cambridge University Press, 40 West 20th Street, New York, NY, USA, 2003.

[35] S. M. Alamouti, "A simple transmit diversity technique for wireless communications," *IEEE Jour. Select. Areas in Comm.*, vol. 16, no. 8, pp. 1451–1458, Oct. 1998.

[36] V. Tarokh, N. Seshadri, and A. R. Calderbank, "Space-time codes for high data rate wireless communication: Performance criterion and code construction," *IEEE Trans. Info. Th.*, vol. 44, pp. 744–65, Mar. 1998.

[37] V. Tarokh, H. Jafarkhani, and A. R. Calderbank, "Space-time block codes from orthogonal designs," *IEEE Trans. Info. Th.*, vol. 45, pp. 1456–467, July 1999.

[38] E. N. Onggosanusi, A. G. Dabak, and T. A. Schmidl, "High rate space-time block coded scheme: performance and improvement in correlated fading channels," *Proc. IEEE Wireless Comm. and Net. Conf.*, vol. 1, pp. 194–199, Mar. 2002.

[39] M. Kang and M.-S. Alouini, "Largest eigenvalue of complex Wishart matrices and performance analysis of MIMO MRC systems," vol. 21, pp. 418–26, Apr. 2003.

[40] M. Kang and M.-S. Alouini, "Performance analysis of MIMO MRC systems over Rician fading channels," *Proc. IEEE Veh. Technol. Conf.*, vol. 2, pp. 869–73, Sep. 2002.

[41] A. A. M. Saleh and R. A. Valenzuela, "A statistical model for indoor multipath propagation," *IEEE Jour. Select. Areas in Comm.*, vol.

SAC-5, no. 2, pp. 128–137, Feb. 1987.

[42] J. W. Wallace and M. A. Jensen, "Statistical characteristics of measured MIMO wireless channel data and comparison to conventional models," *Proc. IEEE Veh. Technol. Conf.*, vol. 2, no. 7-11, pp. 1078–1082, Oct. 2001.

[43] V. Erceg et al., "TGn channel models," *IEEE 802.11-03/940r4*, May 2004.

[44] 3GPP Technical Specification Group, "Spatial channel model, SCM-134 text V6.0," *Spatial Channel Model AHG (Combined ad-hoc from 3GPP and 3GPP2)*, Apr. 2003.

[45] R. B. Ertel, P. Carderi, K. W. Sowerby, T. S. Rappaport, and J. H. Reed, "Overview of spatial channel models for antenna array communication systems," *Proc. IEEE Conf. on Pers. Wireless Comm.*, pp. 10–22, Feb. 1998.

[46] J. P. Kermoal, L. Schumacher, K. I. Pedersen, P. E. Mogensen, and F. Frederiksen, "A stochastic MIMO radio channel model with experimental validation," *IEEE Jour. Select. Areas in Comm.*, vol. 20, no. 6, pp. 1211–1226, Aug. 2002.

[47] L. Schumacher, K. I. Pedersen, and P.E. Mogensen, "From antenna spacings to theoretical capacities-guidelines for simulating MIMO sys-

tems," *Proc. IEEE Int. Symp. on Pers., Indoor and Mobile Radio Comm.*, vol. 2, pp. 587–592, Sep. 2002.

[48] K. I. Pedersen, P. E. Mogensen, and B. H. Fleury, "Power azimuth spectrum in outdoor environments," *Electronics Letters*, vol. 33, no. 18, pp. 1583–1584, Aug. 1997.

[49] K. I. Pedersen, P. E. Mogensen, and B. H. Fleury, "A stochastic model of the temporal and azimuthal dispersion seen at the base station in outdoor propagation environments," *IEEE Trans. on Veh. Technol.*, vol. 49, no. 2, pp. 437–447, Mar. 2000.

[50] Q. H. Spencer, B. D. Jeffs, M. A. Jensen, and A. Lee Swindlehurst, "Modeling the statistical time and angle of arrival characteristics of an indoor multipath channel," *IEEE Jour. Select. Areas in Comm.*, vol. 18, no. 3, pp. 347–360, Mar. 2000.

[51] G. German, Q. Spencer, L. Swindlehust, and R. Valenzuela, "Wireless indoor channel modeling: statistical agreement of ray tracing simulations and channel sounding measurements," *Proc. IEEE Int. Conf. Acoust., Speech and Sig. Proc.*, vol. 4, pp. 2501–2504, May 2001.

[52] J. Wigard and P. Mogensen, "A simple mapping from C/I to FER and BER for a GSM type of air-interface," *Proc. IEEE Int. Symp. on Pers., Indoor and Mobile Radio Comm.*, vol. 1, pp. 78–82, Oct. 1996.

[53] H. Olofsson, M. Almgren, C. Johansson, M. Hook, and F. Kronestedt, "Improved interface between link level and system level simulations applied to GSM," *IEEE 6th International Conference on Universal Personal Communications Record*, vol. 1, pp. 79–83, Oct. 1997.

[54] J. Wigard, T. T. Nielsen, P. H. Michaelsen, and P. Mogensen, "BER and FER prediction of control and traffic channels for a GSM type of air-interface," *Proc. IEEE Veh. Technol. Conf.*, vol. 2, pp. 1588–1592, May 1998.

[55] C. Caini and G. Riva, "A new vector quantization technique for performance evaluation in frequency hopping mobile radio systems," *IEEE Comm. Lett.*, vol. 2, pp. 252–254, Aug. 2000.

[56] R. J. Punnoose, P. V. Nikitin, and D. D. Stancil, "Efficient simulation of Ricean fading within a packet simulator," *Proc. IEEE Veh. Technol. Conf.*, vol. 2, pp. 764–767, Sep. 2000.

[57] D. J. Mazzarese and W. A. Krzymien, "High throughput downlink cellular packet data access with multiple antennas and multiuser diversity," *Proc. IEEE Veh. Technol. Conf.*, vol. 2, pp. 1079–1083, Apr. 2003.

[58] M. Pukkila, G. P. Mattellini, and P. A. Ranta, "Constant modulus single antenna interference cancellation for GSM," *Proc. IEEE Veh. Technol. Conf.*, vol. 1, pp. 584–588, May 2004.

[59] P. A. Ranta, H. Berg, E. Tuomaala, and Z. Uykan, "Dual antenna diversity reception for EGPRS terminals," *Proc. IEEE Veh. Technol. Conf.*, vol. 1, pp. 510–514, May 2004.

[60] M. Dohler, J. Dominguez, and H. Aghvami, "Link capacity analysis for virtual antenna arrays," *Proc. IEEE Veh. Technol. Conf.*, vol. 1, pp. 440–443, Sep. 2002.

[61] A. Kastrisios, M. Dohler, and H. Aghvami, "Influence of channel characteristics on the performance of VAA with deployed STBCs," *Proc. IEEE Veh. Technol. Conf.*, vol. 2, pp. 1138–1142, Apr. 2003.

[62] Q. Spencer, M. Rice, B. Jeffs, and M. Jensen, "A statistical model for angle of arrival in indoor multipath propagation," *Proc. IEEE Veh. Technol. Conf.*, vol. 3, pp. 1415–1419, May 1997.

[63] W.C.Y. Lee, "Effects on the correlation between two mobile radio base-station antennas," *IEEE Trans. Comm.*, vol. COM-21, no. 11, pp. 1214–1224, Nov. 1973.

[64] W. Lee, "Effects on correlation between two mobile radio base-station antennas," *IEEE Trans. Comm.*, vol. 21, no. 11, pp. 1214–1224, Nov. 1973.

[65] W. C. Jakes, *Microwave Mobile Communications*, IEEE Press, 445 Hoes Lane, P.O. Box 1331, Piscataway, New Jersey 08855-1331, 1974.

[66] J. Salz and J. H. Winters, "Effect of fading correlation on adaptive arrays in digital mobile radio," *IEEE Trans. on Veh. Technol.*, vol. 43, no. 4, pp. 1049–1057, Nov. 1994.

[67] M. T. Feeney and J. D. Parsons, "Cross-correlation between 900 MHz signal received on vertically separated antennas in small-cell radio systems," *IEE Proceedings I*, vol. 138, no. 2, pp. 81–86, Apr. 1991.

[68] K. I. Pedersen, P. E. Mogensen, and B. H. Fleury, "Spatial channel characteristics in outdoor environments and their impact on BS antenna system performance," *Proc. IEEE Veh. Technol. Conf.*, vol. 2, pp. 719–723, 1998.

[69] A. S. Y. Poon and M. Ho, "Indoor multiple-antenna channel characterization from 2 to 8 GHz," *Proc. IEEE Int. Conf. on Comm.*, vol. 5, pp. 3519–3523, May 2003.

[70] R. J. Cramer, R. A. Scholtz, and M. Z. Win, "Evaluation of an Ultra-Wide-Band propagation channel," *IEEE Trans. Antennas Propagat.*, vol. 50, no. 5, pp. 561–570, May 2002.

[71] G. D. Durgin, *Space-Time Wireless Channels*, Prentice Hall, Upper Saddle River, NJ, USA, 2003.

[72] G. D. Durgin and T. S. Rappaport, "Theory of multipath shape factors for small-scale fading wireless channels," *IEEE Trans. Antennas Propagat.*, vol. 48, pp. 682–693, May 2000.

[73] H. Bölcskei, M. Borgmann, and A. J. Paulraj, "Impact of the propagation environment on the performance of space-frequency coded MIMO-OFDM," *IEEE JSAC*, vol. 21, pp. 427–439, Apr. 2003.

[74] H. Bölcskei, D. Gesbert, and A. J. Paulraj, "On the capacity of OFDM-based spatial multiplexing systems," *IEEE Trans. Comm.*, vol. 50, no. 2, pp. 225–234, Feb. 2002.

[75] M. Stege, J. Jelitto, M. Bronzel, and G. Fettweis, "A multiple input-multiple output channel model for simulation of Tx- and Rx-diversity wireless systems," *Proc. IEEE Veh. Technol. Conf.*, vol. 2, pp. 833–839, Sep. 2000.

[76] A. F. Molisch, "A generic model for MIMO wireless propagation channels in macro- and microcells," *IEEE Trans. Sig. Proc.*, vol. 52, pp. 61–71, Jan. 2004.

[77] K. Yu, *Multiple-Input Multiple-Output Radio Propagation Channels: Characteristics and Models*, Doctoral Thesis, KTH Signal Sensor and Systems, Stockholm, Sweden, 2005.

[78] H. Ozcelik, M. Herdin, W. Weichselberger, J. Wallace, and E. Bonek, "Deficiencies of 'kronecker' MIMO radio channel model," *Electronics Letters*, vol. 39, no. 16, pp. 1209–1210, Aug. 2003.

[79] W. Weichselberger, H. Özcelik, M. Herdin, and E. Bonek, "A novel stochastic MIMO channel model and its physical interpretation," *in*

International Symposium on Wireless Personal Multimedia Communications, WPMC (Yokosuka, Japan), Oct. 2003.

[80] S. Wyne, A. F. Molisch, P. Almers, G. Eriksson, J. Karedal, and F. Tufvesson, "Statistical evaluation of outdoor-to-indoor office MIMO measurements at 5.2 GHz," *Proc. IEEE Veh. Technol. Conf.*, vol. 1, pp. 146–150, July 2005.

[81] C. Oestges, H. Özcelik, and E. Bonek, "On the practical use of analytical MIMO channel models," *Proc. IEEE Antennas and Prop. Symp.*, vol. 3B, pp. 406–409, July 2005.

[82] M. A. Jensen and J. W. Wallace, "A review of antennas and propagation for MIMO wireless communications," *IEEE Trans. Antennas Propagat.*, vol. 52, pp. 2810–2824, Nov. 2004.

[83] A. M. Tulino, A. Lozano, and S. Verdu, "Impact of antenna correlation on the capacity of multiantenna channels," *IEEE Trans. Info. Th.*, vol. 51, pp. 2491–2509, July 2005.

[84] A. M. Tulino, S. Verdu, and A. Lozano, "Capacity of antenna arrays with space, polarization and pattern diversity," *Proc. of IEEE Info. Th. Workshop*, pp. 324–327, Mar. 2003.

[85] S. W. Ellingson, "Antenna design and site planning considerations for MIMO," *Proc. IEEE Veh. Technol. Conf.*, vol. 3, pp. 1718–1722, Sep. 2005.

[86] T. Svantesson, "Correlation and channel capacity of MIMO systems employing multimode antennas," *IEEE Trans. on Veh. Technol.*, vol. 51, pp. 1304–1312, Nov. 2002.

[87] C. Waldschmidt, W. Sorgel, F. Pivit, and W. Wiesbeck, "Broadband multimode antennas for MIMO applications," *Proc. IEEE Antennas and Prop. Symp.*, vol. 2, pp. 511–514, June 2003.

[88] J. B. Andersen and B. N. Getu, "The MIMO cube-a compact MIMO antenna," *IEEE Proc. of Wireless Personal Multimedia Communications Int. Symp.*, vol. 1, pp. 112–114, Oct. 2002.

[89] C. Waldschmidt, C. Kuhnert, S. Schulteis, and W. Wiesbeck, "Compact MIMO-arrays based on polarisation-diversity," *Proc. IEEE Antennas and Prop. Symp.*, vol. 2, pp. 499–502, June 2003.

[90] C. B. Dietrich Jr, K. Dietze, J. R. Nealy, and W. L. Stutzman, "Spatial, polarization, and pattern diversity for wireless handheld terminals," *Proc. IEEE Antennas and Prop. Symp.*, vol. 49, pp. 1271–1281, Sep. 2001.

[91] S. Visuri and D. T. Slock, "Colocated antenna arrays: design desiderata for wireless communications," *Proc. of Sensor Array and Multichannel Sign. Proc. Workshop*, pp. 580–584, Aug. 2002.

[92] R. U. Nabar, H. Bölcskei, V. Erceg, D. Gesbert, and A. J. Paulraj, "Performance of spatial-multiplexing in the presence of polarization di-

versity," *Proc. IEEE Int. Conf. Acoust., Speech and Sig. Proc.*, vol. 4, pp. 2437–2440, May 2001.

[93] C. C. Martin, J. H. Winters, and N. R. Sollenberger, "MIMO radio channel measurements: performance comparison of antenna configurations," *Proc. IEEE Veh. Technol. Conf.*, vol. 2, pp. 1225–1229, Oct. 2001.

[94] H. J. Li and C. H. Yu, "Correlation properties and capacity of antenna polarization combinations for MIMO radio channel," *Proc. IEEE Antennas and Prop. Symp.*, vol. 2, pp. 503–506, Jun. 2003.

[95] V. Jungnickel, V. Pohl, H. Nguyen, U. Kruger, T. Haustein, and C. Von Helmolt, "High capacity antennas for MIMO radio systems," *Int. Symp. on Wireless Personal Communications*, vol. 2, pp. 407–411, Oct. 2002.

[96] R. G. Vaughan, "Two-port higher mode circular microstrip antennas," *IEEE Trans. Antennas Propagat.*, vol. 36, pp. 309–321, Mar. 1988.

[97] R. G. Vaughan and J. B. Anderson, "A multiport patch antenna for mobile communications," *Proc. 14th European Microwave Conf.*, pp. 607–612, 1984.

[98] C. A. Balanis, *Antenna Theory: Analysis and Design (second edition)*, John Wiley and Sons, Inc., New York, NY, USA, 1982.

[99] P. Pirinoli, G. Vecchi, and M. Orefice, "Full-wave spectral analysis and design of annular patch antenna with electromagnetically coupled mi-

crostrip feed line," *IEEE Transactions on Antennas and Propagation*, vol. 52, no. 9, pp. 2415–2423, 2004.

[100] T. Svantesson, M. A. Jensen, and J. W. Wallace, "Analysis of electromagnetic field polarizations in multiantenna systems," *IEEE Trans. Wireless Comm.*, vol. 3, pp. 641–646, Mar. 2004.

[101] A. P. Prudnikov, Y. A. Brychkov, and O. I. Marichev, *Integrals and Series (Volume 1)*, Gordon and Breach of Science Publishers, New York, NY, 1986.

[102] B. Ottersten, "Spatial division multiple access (SDMA) in wireless communications," *Signal Processing, in Proc. of Nordic Radio Symposium*, 1995.

[103] B. Ottersten, "Array processing for wireless communications," *8th IEEE Signal Processing Workshop on Statistical Signal and Array Processing*, Mar. 1996.

[104] H. Shin and J. H. Lee, "Capacity of multiple-antenna fading channels: spatial fading correlation, double scattering, and keyhole," *IEEE Trans. Info. Th.*, vol. 49, pp. 2636–2647, Oct. 2003.

[105] A. Forenza, D. J. Love, and R. W. Heath Jr., "A low complexity algorithm to simulate the spatial covariance matrix for clustered MIMO channel models," *Proc. IEEE Veh. Technol. Conf.*, vol. 2, pp. 889–893, May 2004.

[106] M. L. Morris and M. A. Jensen, "Network model for MIMO systems with coupled antennas and noisy amplifiers," *IEEE Trans. Antennas Propagat.*, vol. 53, pp. 545–552, Jan. 2005.

[107] C. Waldschmidt, S. Schulteis, and W. Wiesbeck, "Complete RF system model for analysis of compact MIMO arrays," *IEEE Trans. on Veh. Technol.*, vol. 53, pp. 579–586, May 2004.

[108] D. M. Pozar, *Microwave Engineering (second edition)*, John Wiley and Sons, Inc., New York, NY, USA, 1998.

[109] S. Yano and A. Ishimaru, "A theoretical study of the input impedance of a circular microstrip disk antenna," *IEEE Trans. Antennas Propagat.*, vol. 29, pp. 77 – 83, Jan. 1981.

[110] A. Forenza and R. W. Heath Jr., "Benefit of pattern diversity via 2-element array of circular patch antennas in indoor clustered MIMO channels," *to appear on IEEE Trans. on Comm.*, Mar. 2005.

[111] M. R. McKay and I. B. Collings, "General capacity bounds for spatially correlated Rician MIMO channels," *IEEE Trans. Info. Th.*, vol. 51, pp. 3121–3145, Sep. 2005.

[112] R. G. Vaughan and J. B. Anderson, "Antenna diversity in mobile communications," *IEEE Trans. on Veh. Technol.*, vol. VT-36, pp. 149–172, Nov. 1987.

[113] M. A. Jensen and Y. Rahmat-Samii, "Performance analysis of antennas for hand-held transceivers using FDTD," *IEEE Trans. Antennas Propagat.*, vol. 42, pp. 1106–1113, Aug. 1994.

[114] M. Kiessling and J. Speidel, "Mutual information of MIMO channels in correlated Rayleigh fading environments-a general solution," *Proc. IEEE Int. Conf. on Comm.*, vol. 2, pp. 814–818, Jun. 2004.

[115] S. C. K. Ko and R. D. Murch, "Compact integrated diversity antenna for wireless communications," *IEEE Trans. Antennas Propagat.*, vol. 49, pp. 954–960, Jun. 2001.

[116] Kuo-Hui Li, M.A. Ingram, and A. Van Nguyen, "Impact of clustering in statistical indoor propagation models on link capacity," *IEEE Transactions on Communications*, vol. 50, no. 4, pp. 521–523, 2002.

[117] M.J. Fakhereddin and K.R. Dandekar, "Combined effect of polarization diversity and mutual coupling on MIMO capacity," *Proc. IEEE Antennas and Prop. Symp.*, vol. 2, pp. 495–498, June 2003.

[118] T. Svantesson and A. Ranheim, "Mutual coupling effects on the capacity of multielement antenna systems," *Proc. IEEE Int. Conf. Acoust., Speech and Sig. Proc.*, vol. 4, pp. 2485–2488, May 2001.

[119] P. N. Fletcher, M. Dean, and A. R. Nix, "Mutual coupling in multielement array antennas and its influence on MIMO channel capacity," *IEEE Electronics Letters*, vol. 39, pp. 342–344, Feb. 2003.

[120] V. Jungnickel, V. Pohl, and C. Von Helmolt, "Capacity of MIMO systems with closely spaced antennas," *IEEE Comm. Lett.*, vol. 7, pp. 361–363, Aug. 2003.

[121] A. Konanur, K. Gosalia, S. Krishnamanhy, B. Hughes, and G. Lazzi, "Investigation of the performance of co-polarized, co-located electric and magnetic dipoles for increasing channel capacity," *Proc. IEEE Antennas and Prop. Symp.*, vol. 2, pp. 531–534, June 2003.

[122] J. W. Wallace and M. A. Jensen, "Termination-dependent diversity performance of coupled antennas: Network theory analysis," *IEEE Trans. Antennas Propagat.*, vol. 52, pp. 98–105, Jan. 2004.

[123] R. R. Ramirez and F. De Flaviis, "A mutual coupling study of linear and circular polarized microstrip antennas for diversity wireless systems," *IEEE Trans. Antennas Propagat.*, vol. 51, pp. 238–248, Feb. 2003.

[124] I. Salonen, A. Toropainen, and P. Vainikainen, "Linear pattern correction in a small microstrip antenna array," *IEEE Trans. Antennas Propagat.*, vol. 52, pp. 578–586, Feb. 2004.

[125] L. Zheng and D. N. C. Tse, "Diversity and multiplexing: a fundamental tradeoff in multiple-antenna channels," *IEEE Trans. Info. Th.*, vol. 49, no. 5, pp. 1073–1096, May 2003.

[126] R. W. Heath Jr. and A. Paulraj, "Switching between multiplexing and diversity based on constellation distance," *Proc. of Allerton Conf. on*

Comm. Control and Comp., Sep. 2000.

[127] S. Catreux, V. Erceg, D. Gesbert, and R. W. Heath Jr., "Adaptive modulation and MIMO coding for broadband wireless data networks," *IEEE Comm. Mag.*, vol. 2, pp. 108–115, June 2002.

[128] M. Bengtsson, D. Astely, and B. Ottersten, "Measurements of spatial characteristics and polarization with a dual polarized antenna array," *Proc. IEEE Veh. Technol. Conf.*, vol. 1, pp. 366–370, May 1999.

[129] E. Visotsky and U. Madhow, "Space-time transmit precoding with imperfect feedback," *IEEE Trans. Info. Th.*, vol. 47, pp. 2632–2639, Sep. 2001.

[130] S. A. Jafar, S. Vishwanath, and A. Goldsmith, "Channel capacity and beamforming for multiple transmit and receive antennas with covariance feedback," *Proc. IEEE Int. Conf. on Comm.*, vol. 7, pp. 2266–2270, Jun. 2001.

[131] S. A. Jafar and A. Goldsmith, "Transmitter optimization and optimality of beamforming for multiple antenna systems," *IEEE Trans. Wireless Comm.*, vol. 3, pp. 1165–1175, July 2004.

[132] E. A. Jorswieck and H. Boche, "Channel capacity and capacity-range of beamforming in MIMO wireless systems under correlated fading with covariance feedback," *IEEE Trans. Wireless Comm.*, vol. 3, pp. 1543–1553, Sep. 2004.

[133] A. L. Moustakas and S. H. Simon, "Optimizing multiple-input single-output (MISO) communication systems with general Gaussian channels: nontrivial covariance and nonzero mean," *IEEE Trans. Info. Th.*, vol. 49, pp. 2770–2780, Oct. 2003.

[134] M. Kang and M. S. Alouini, "Water-filling capacity and beamforming performance of MIMO systems with covariance feedback," *IEEE Work. on Sign. Proc. Adv. in Wire. Comm.*, pp. 556–560, June 2003.

[135] S. H. Simon and A. L. Moustakas, "Optimizing MIMO antenna systems with channel covariance feedback," *IEEE Jour. Select. Areas in Comm.*, vol. 21, pp. 406–417, Apr. 2003.

[136] P. J. Smith, S. Roy, and M. Shafi, "Capacity of MIMO systems with semicorrelated flat fading," *IEEE Trans. Info. Th.*, vol. 49, pp. 2781 – 2788, Oct. 2003.

[137] M. Chiani, M. Z. Win, and A. Zanella, "On the capacity of spatially correlated MIMO Rayleigh-fading channels," *IEEE Trans. Info. Th.*, vol. 49, pp. 2363–2371, Oct. 2003.

[138] P. J. Smith, S. Roy, and M. Shafi, "Capacity of MIMO systems with semicorrelated flat fading," *IEEE Trans. Info. Th.*, vol. 49, pp. 2781–2788, Oct. 2003.

[139] M. R. McKay and I. B. Collings, "Capacity bounds for correlated Rician MIMO channels," in *Int. Conf. Comm.*, 2005, accepted for publication.

[140] A. M. Mathai and S. B. Provost, *Quadratic Forms in Random Variables*, Marcell Dekker, Inc., New York, NY, 1992.

[141] I. S. Gradshteyn and I. M. Ryzhik, *Table of Integrals, Series, and Products*, Academic Press Inc., New York, NY, 1st edition, 1994.

[142] B. Hassibi and B. M. Hochwald, "High-rate codes that are linear in space and time," *IEEE Trans. Info. Th.*, vol. 48, pp. 1804–1824, July 2002.

[143] M. Kiessling and J. Speidel, "Ergodic capacity of MIMO channels with statistical channel state information at the transmitter," *ITG Workshop on Smart Antennas*, Mar. 2004.

[144] D. Gore, R. W. Heath, and A. Paulraj, "Transmit selection in spatial multiplexing systems," *IEEE Comm. Lett.*, vol. 6, pp. 491–493, Nov. 2002.

[145] R. W. Heath, S. Sandhu, and A. Paulraj, "Antenna selection for spatial multiplexing systems with linear receivers," *IEEE Comm. Lett.*, vol. 5, pp. 142–144, Apr. 2001.

[146] R. A. Horn and C. R. Johnson, *Matrix Analysis*, University of Cambridge Press, New York, 4th edition, 1990.

[147] T. Takahama and S. Sakai, "Constraint optimization by α constraint genetic aglorithm (αGA)," *in Systems and Computers in Japan*, vol. 35, 2004.

[148] K. B. Song, *Value of Adaptive Transmission and Effect of Imperfect Decision Feedback in Practical Wireless Systems*, Ph.D. dissertation, Stanford University, 2005.

[149] A. C. Aitken, *Determinants and Matrices (9th ed.)*, Oliver and Boyd, Edinburgh, 1956.

[150] A. W. Marshall and I. Olkin, *Inequalities: Theory of Majorization and Its Applications*, Academic, New York, 1979.

[151] A. Forenza, M. R. McKay, A. Pandharipande, R. W. Heath Jr., and I. B. Collings, "Capacity enhancement via multi-mode adaptation in spatially correlated MIMO channels," *to appear on Proc. IEEE Int. Symp. on Pers., Indoor and Mobile Radio Comm.*, Sep. 2005.

[152] R. W. Heath Jr. and A. Paulraj, "Switching between spatial multiplexing and transmit diversity based on constellation distance," *IEEE Trans. Comm.*, vol. 53, no. 6, pp. 962–968, June 2005.

[153] R. W. Heath Jr. and D. J. Love, "Multi-mode antenna selection for spatial multiplexing systems with linear receivers," *Proc. of Allerton Conf. on Comm. Control and Comp.*, Oct. 2003.

[154] R. Narasimhan, "Spatial multiplexing with transmit antenna and constellation selection for correlated MIMO fading channels," *IEEE Trans. Sig. Proc.*, vol. 51, pp. 2829–2838, Nov. 2003.

[155] M. R. G. Butler and I. B. Collings, "A zero-forcing approximate log-likelihood receiver for MIMO bit-interleaved coded modulation," *IEEE Comm. Lett.*, vol. 8, pp. 105–107, Feb. 2004.

[156] M. R. McKay and I. B. Collings, "Capacity and performance of MIMO-BICM with zero forcing receivers," *IEEE Trans. Comm.*, vol. 53, pp. 74–83, Jan. 2005.

[157] A. Martinez, A. Guillén i Fàbregas, and G. Caire, "New simple evaluation of the error probability of bit-interleaved coded modulation using the saddlepoint approximation," *Proc. IEEE Int. Symp. Info. Th.*, Oct. 2004.

[158] A. Martinez, A. Guillén i Fàbregas, and G. Caire, "Error probability analysis of bit-interleaved coded modulation," *IEEE Trans. Info. Th.*, vol. 52, pp. 262–271, Jan. 2006.

[159] G. Caire, G. Taricco, and E. Biglieri, "Bit-interleaved coded modulation," *IEEE Trans. Info. Th.*, vol. 44, pp. 927–946, May 1998.

[160] E. Telatar, "Capacity of multi-antenna Gaussian channels," AT&T Bell Laboratories Tech. Report, June 1995.

[161] M. Abramowitz and I. A. Stegun, *Handbook of Mathematical Functions with Formulas, Graphs, and Mathematical Tables*, Dover Publications, New York, 1970.

[162] D. Divsalar, H. Jin, and R. J. McEliece, "Coding theorems for "turbo-like" codes," *Proc. of Allerton Conf. on Comm. Control and Comp.*, pp. 201–210, Sep. 1998.

[163] X. Li and J. A. Ritcey, "Trellis-coded modulation with bit interleaving and iterative decoding," *IEEE Jour. Select. Areas in Comm.*, vol. 17, pp. 715–724, Apr. 1999.

[164] X. Li, A. Chindapol, and J. A. Ritcey, "Bit-interleaved coded modulation with iterative decoding and 8PSK signalling," *IEEE Trans. Comm.*, vol. 50, pp. 1250–1257, Aug. 2002.

[165] A. M. Tonello, "Space-time bit-interleaved coded modulation with an iterative decoding strategy," pp. 473–478, Sep. 2000.

[166] A. J. Viterbi and J. K. Omura, *Principles of Digital Communication and Coding*, McGraw-Hill, New York, 1979.

[167] R. Gallager, *Information Theory and Reliable Communication*, John Wiley and Sons, New York, 1968.

[168] R. Durrett, *Probability: Theory and Examples*, Duxbury Press, 1996.

[169] M. R. McKay and I. B. Collings, "Error performance of MIMO-BICM with zero-forcing receivers in spatially-correlated Rayleigh channels," *IEEE Trans. Wireless Comm.*, 2006.

[170] E. Biglieri, G. Caire, G. Taricco, and J. Ventura-Traveset, "Simple method for evaluating error probabilities," *Electronics Letters*, vol. 32, pp. 191–192, Feb. 1996.

[171] A. W. Marshall and I. Olkin, *Inequalities: Theory of Majorization and Its Applications*, Academic, New York, 1979.

[172] H. Jarfakhani, "Quasi-orthogonal space-time block code," *IEEE Trans. Comm.*, vol. 49, pp. 1–4, 2001.

[173] G. J. Foschini and M. J. Gans, "On limits of wireless communications in a fading environment when using multiple antennas," *Proc. IEEE Conf. on Pers. Wireless Comm.*, vol. 6, no. 3, pp. 311–335, Mar. 1998.

[174] M. R. McKay, I. B. Collings, A. Forenza, and R. W. Heath Jr., "Low complexity adaptive MIMO-BICM for spatially-correlated Rayleigh channels," *submitted to IEEE Trans. on Vehic. Techn.*, Apr. 2005, www.ece.utexas.edu/∼forenza.

[175] C. B. Chae, M. Katz, C. H. Suh, and H. S. Jeong, "Adaptive spatial modulation for MIMO-OFDM," *Proc. IEEE Wireless Comm. and Net. Conf.*, vol. 1, pp. 87–92, Mar. 2004.

[176] "Part 11: Wireless LAN medium access control (MAC) and physical layer (PHY) specifications: High-speed physical layer in the 5 GHz band," *IEEE Standard 802.11a*, 1999.

[177] "Part 11: Wireless LAN Medium Access Control (MAC) and Physical Layer (PHY) Specifications: High-Speed Physical Layer in the 5 GHz Band," IEEE Standard 802.11a 1999.

[178] A. Paulraj, "Is OFDMA, MIMO and OS the right stuff for mobile broadband?," *http://www.ieeevtc.org/vtc2005fall/presentations/paulraj.pdf*, Sep. 2005.

[179] C.R. Rowell and R.D. Murch, "A capacitively loaded PIFA for compact mobile telephone handsets," *IEEE Transactions on Antennas and Propagation*, vol. 45, no. 5, pp. 837–842, 1997.

[180] RongLin Li, G. DeJean, M.M. Tentzeris, and J. Laskar, "Development and analysis of a folded shorted-patch antenna with reduced size," *IEEE Transactions on Antennas and Propagation*, vol. 52, no. 2, pp. 555–562, 2004.

[181] B. A. Cetiner, H. Jafarkhani, Jiang-Yuan Qian, Hui Jae Yoo, A. Grau, and F. De Flaviis, "Multifunctional reconfigurable MEMS integrated antennas for adaptive mimo systems," *IEEE Comm. Mag.*, vol. 42, pp. 62– 70, Dec. 2004.

[182] D.E. Anagnostou, Guizhen Zheng, M.T. Chryssomallis, J.C. Lyke, G.E. Ponchak, J. Papapolymerou, and C.G. Christodoulou, "Design, fabrication, and measurements of an RF-MEMS-based self-similar reconfigurable antenna," *IEEE Transactions on Antennas and Propagation*, vol. 54, pp. 422–432, 2006.

[183] Chang won Jung, Ming jer Lee, G.P. Li, and F. De Flaviis, "Reconfigurable scan-beam single-arm spiral antenna integrated with RF-MEMS switches," *IEEE Transactions on Antennas and Propagation*, vol. 54, pp. 455–463, 2006.

[184] G.H. Huff and J.T. Bernhard, "Integration of packaged RF MEMS switches with radiation pattern reconfigurable square spiral microstrip antennas," *IEEE Transactions on Antennas and Propagation*, vol. 54, pp. 464–469, 2006.

[185] S.-L.S. Yang and Kwai-Man Luk, "Design of a wide-band l-probe patch antenna for pattern reconfiguration or diversity applications," *IEEE Transactions on Antennas and Propagation*, vol. 54, pp. 433–438, 2006.

[186] Symeon Nikolaou, R. Bairavasubramanian, Jr. Lugo, C., I. Carrasquillo, D.C. Thompson, G.E. Ponchak, J. Papapolymerou, and M.M. Tentzeris, "Pattern and frequency reconfigurable annular slot antenna using PIN diodes," *IEEE Transactions on Antennas and Propagation*, vol. 54, pp. 439–448, 2006.

[187] C.J. Panagamuwa, A. Chauraya, and J.C. Vardaxoglou, "Frequency and beam reconfigurable antenna using photoconducting switches," *IEEE Transactions on Antennas and Propagation*, vol. 54, pp. 449–454, 2006.

[188] A. B. Balantekin, "Character expansions, Itzykson-Zuber intergrals, and the QCD partition function," *Phys. Rev. D*, vol. 62, pp. 085 017(1)–085 017(8), Sep. 2000.

Index

Abstract, vi
Acknowledgments, v
Appendices, 185

Dedication, iv

Vita

Antonio Forenza received his B.S. and M.S. degrees in Telecommunications Engineering from Politecnico di Torino (Italy) and the Institut Eurécom (Sophia Antipolis, France) in 2001.

In 2001 he interned as systems engineer at Iospan Wireless, Inc., San Jose, CA, a startup company that developed the first commercial MIMO-OFDM communication system. His main focus was on link-adaptation and physical layer algorithm design. In the fall 2001 he joined ArrayComm, Inc. (San Jose, CA), as systems research engineer, where he worked on smart antenna technology for 3G WCDMA wireless systems. Over the summer 2004 and 2005 he interned as research engineer at Samsung (SAIT, Suwon, Korea) and Freescale Semiconductor, Inc. (Austin, TX), respectively, developing adaptive MIMO transmission and MU-MIMO precoding techniques for 3GPP, IEEE 802.11n and IEEE 802.16e standards systems.

His research interests include wireless MIMO-OFDM and WCDMA systems, adaptive MIMO transmission techniques, MIMO antenna design, precoding methods for MU-MIMO, smart antenna signal processing.

Permanent address: 5109 Avenue H
Austin, Texas 78751

This dissertation was typeset with LaTeX[†] by the author.

[†]LaTeX is a document preparation system developed by Leslie Lamport as a special version of Donald Knuth's TeX Program.